Influence of Chemical Doping on Microstructures and Superconducting Properties of MgB_2 Wires and Bulk Samples

DISSERTATION

Presented in Partial Fulfillment of the Requirements for the Degree Doctor of Philosophy in the Graduate School of the Ohio State University

By

Yuan Yang

Graduate Program in Materials Science and Engineering

The Ohio State University

2016

Dissertation Committee:

Dr. Michael D. Sumption, Adviser

Dr. Patricia Morris

Dr. Roberto Myers

Abstract

Magnesium diboride (MgB_2) is a material with a superconducting transition temperature of 39 K. Discovered in 2001, the relatively large coherence length (and associated lack of weak links) together with its simple binary composition (making phase pure formation relatively easy) have made it a material of substantial interest. However, its inadequate in-field performance limits the high field applications. Chemical doping is the key to increasing the B_{c2} of MgB_2. Chemical doping aiming at Mg site or B site substitution is of interest and both routes are explored in this thesis. Structure-property correlations are developed for dopants that either do or do not, incorporate themselves into the MgB_2 matrix.

First, the effects of C doping in the state of art MgB_2 wires were investigated. In order to do so, a series of state of the art C doped MgB_2 wires, in both mono-filamentary and multi-filamentary forms, were fabricated by a local company. Their transport and magnetic performance in various magnetic fields, and mechanical induced degradation, were examined. The C doping influence on the critical current density and the *n*-values were discussed.

Secondly, the effects of rare earth oxide (REO) doping in MgB_2 were studied. Two sets of samples including both bulk samples and wires were fabricated. Microstructural

evidence obtained by SEM and TEM proved that nano-size inclusions formed after REO doping acted as grain growth inhibitors, as evidenced a reduction of MgB_2 grain size in REO doped bulk samples. The results of XRD and magnetic measurements on the bulk samples demonstrated that Dy_2O_3 and Nd_2O_3 do not alloy with MgB_2, no changes being observed in the lattice parameters, T_c and B_{c2} of doped MgB_2. Enhancements in flux pinning and J_c were obtained in both bulk samples and wires by REO doping, consistent with the microstructural evidence of notable grain refinements and the presence of nano-size inclusions as new pinning sites in MgB_2 grains.

Lastly, a set of metal diboride and Dy_2O_3 added MgB_2 bulk samples were synthesized at very high temperatures and pressures (up to 1700°C and 10 MPa) to explore solubility limits of dopant species in MgB_2 and enhance diffusion during the sample synthesis. The microstructure was studied by XRD, EDS, TEM and STEM, and doping the influence of doping on superconducting properties were investigated by magnetic measurement. The chemical doping induced changes in microstructure and properties of MgB_2 bulk samples were discussed.

Dedication

This document is dedicated to my family.

Acknowledgments

I would like to thank both Dr. Michael D. Sumption and Dr. Edward W. Collings for their guidance, enthusiasm, and support they have given me throughout the completion of my doctoral work. I would also like to thank the members of my dissertation committee, Dr. Roberto C. Myers and Dr. Patricia Morris, as well as Dr. Sheikh Akbar and Dr. William Clark who served in my Ph.D. candidacy exam, for their support, advice, and constructive criticism.

In addition, I would like to thank the co-workers and colleagues from Department of Materials Science and Engineering at The Ohio State University, including but not limited to Dr. Milan Majoros, Dr. Scot Bohnenstiehl, Dr. Michael Susner, Mohammed Mahmud, Madhu Kongara, Cory Myers, Chris Kovacs, Xingchen Xu, Guangze Li, Yi Ding, Hyun-Sung Kim, Ashiwini Chandra, Jake Zwayer, and Mike Kuldell. I would also like to thank my collaborators at Hyper-Tech Research, Inc., including Matt Rindfleisch, Xuan Peng, Mike Tomsic, CJ Thong and Jinji Yue.

I also want to acknowledge the following grants which supported my research: National Institutes of Health (NIH), National Institute of Biomedical Imaging and Bioengineering, under R01EB018363.

Furthermore, I would like to thank the staff of the Department of Materials Science and Engineering, particularly Ken Kushner, Ross Baldwin, Steve Bright, Mark Cooper, Mei Wang, and Kathleen Babusci. Additionally, thanks to Henk Colijn, Cameron Begg, and Dan Huber of Center for Electron Microscopy and Analysis (CEMAS) for their help with XRD, TEM, SEM, and FIB training.

Finally, I would like to acknowledge the supports of my beloved family. None of this thesis work would be possible without their support.

Vita

Jan 8, 1988 .....Born in Changji, Xinjiang, China

2002.....No.1 Senior High School of Ürümqi

2005.....B.S. Physics, Zhejiang University

2009 to 2015 .....M.S. Materials Science and Engineering, The Ohio State University

2009 to present .....Graduate Research Associate, Department of Materials Science and Engineering, The Ohio State University

Publications

Y. Yang, M. D. Sumption and E. W. Collings, "Influence of Metal Diboride and Dy_2O_3 Additions on Microstructure and Properties of MgB_2 Fabricated at High Temperatures and Under Pressure", *Sci. Rep.* **6,** 29306 (2016).

Y. Yang, M. D. Sumption, M. Rindfleisch, M. Tomsic and E. W. Collings, "Strong enhancement of critical current density and flux pinning in rare earth oxides added MgB_2 bulks and strands by notable grain refinement", in preparation.

Y. Yang, G. Li, M. Susner, M. D. Sumption, M. Rindfleisch, M. Tomsic and E. W. Collings, "Influence of twisting and bending on the J_c and *n*-value of multifilamentary MgB_2 strands", *Physica C*, **519** 188-123 (2015).

M. A. Susner, S. D. Bohnenstiehl, S. A. Dregia, M. D. Sumption, **Y. Yang**, J. J. Donovan and E. W. Collings, "Homogeneous carbon doping of magnesium diboride by high-temperature, high-pressure synthesis", *Appl. Phys. Lett.* **104,** 162603 (2014).

G. Z. Li, K. M. Reddy, J. B. Zwayer, M. A. Kuldell, M. A. Susner, **Y. Yang**, M. D. Sumption, J. J. Yue, M. A. Rindfleisch, M. J. Tomsic, C. J. Thong and E. W. Collings. "Critical current density and current transfer length of multifilamentary MgB_2 strands of various design*", IEEE Trans. Appl. Supercond.,* **23** 6200202 (2013).

Y. Yang, M. A. Susner, M. D. Sumption, M. A. Rindfleisch, M. J. Tomsic and E. W. Collings "Influence of Strand Design, Boron Type, and Carbon Doping Method on the Transport Properties of Powder-in-Tube MgB_2-xCx Strands", *IEEE Trans. Appl. Supercond.* **22** 6200110 (2012).

G. Z. Li, M. D. Sumption, M. A. Susner, **Y. Yang**, K. M. Reddy, M. A. Rindfleisch, M. J. Tomsic, C. J. Thong and E. W. Collings, "The critical current density of advanced internal-Mg-diffusion-processed MgB_2 wires", *Supercond. Sci. Technol.,* **25** 115023 (2012).

G. Z. Li, **Y. Yang**, M. A. Susner, M. D. Sumption and E. W. Collings, "Critical current densities and n-values of MgB_2 strands over a wide range of temperatures and fields", *Supercond. Sci. Technol.,* **25** 025001 (2012).

Y. Ding, G. Z. Li, **Y. Yang**, C. J. Kovacs, M. A. Susner, M. D. Sumption, Y. Sun, J. C. Zhuang, Z. X. Shi, M. Majoros and E. W. Collings, "Effects of cold high pressure densification on Cu sheathed $Ba_{0.6}K_{0.4}Fe_2As_2$ superconducting wire", *Physica C,* **483** 13-16 (2012).

M. A. Susner, **Y. Yang**, M. D. Sumption, E. W. Collings, M. A. Rindfleisch, M. J. Tomsic and J. V. Marzik, "Enhanced critical fields and superconducting properties of pre-doped B powder-type MgB_2 strands", *Supercond. Sci. Technol.* **24**, 012001 (2011).

S. D. Bohnenstiehl, M. A. Susner, **Y. Yang**, E. W. Collings, M. D. Sumption, M. A. Rindfleisch and R. Boone, "Carbon doping of MgB_2 by toluene and malic-acid-in-toluene", *Physica C,* **471** 3-4 108-111 (2011).

Fields of Study

Major Field: Materials Science and Engineering

Table of Contents

List of Tables

List of Figures

Chapter 1: Introduction to MgB_2 Superconductors

1.1 Discovery, Advantages and Limitations in MgB_2 Superconductors

Superconductivity in magnesium diboride (MgB_2) was discovered by Akimitsu *et al.* in 2001 [1]. However, research on MgB_2 itself began over one hundred years ago [2], shortly after Onnes' discovery of superconductivity in mercury [3]. MgB_2 was first seen in the literature in 1881 as a product of the reduction of B_2O_3 with Mg [2]; however, at the time it was identified as Mg_3B_2. In 1954, Russell [4] used X-ray diffraction (XRD) to determine the lattice parameters of MgB_2, thereby fixing the composition at MgB_2 for the lowest boride phase based on geometric constraints. The observation was then confirmed by many authors [1], who categorized MgB_2 into a P6/mmm space group.

With a transition temperature T_c of about 39K, the MgB_2 superconductor can be operated under closed-loop refrigeration instead of in a liquid helium bath. Compared to Nb-based alloys and intermetallic superconductors which have been well studied, the possibility of applications at 20-25 K make MgB_2 cost competitive. Although the T_cs of several cuprate-based high temperature superconductors are in the range of 90K [6,7], their highly anisotropic properties and weak-link problems which require a high degree of grain alignment, as well as cost, limit the industrial applications of these materials. Additionally,

MgB_2 is synthesized from relatively inexpensive constituent elements (Mg and B), contains no weak links, and it is relatively easy to fabricate. All these advantages make it a good candidate for future applications.

In spite of the aforementioned advantages, several obstacles limit the actual application of MgB_2 superconductors: (i) low connectivity, due to its porous structure and the presence of impurity phases; (ii) low critical current density, J_c, which is proportionally related to its flux pinning behavior, and (iii) low values of the upper critical field, B_{c2}, compared to those of Nb_3Sn and some cuprate-based superconductors, a deficiency that limits its high magnetic field application. Extensive studies have been devoted to the resolution of these issues [8-11]. Chemical doping has been seen to be an efficient way to enhance the properties of MgB_2 superconductor, especially flux pinning and upper critical field B_{c2}.

1.2 Structure and General Properties of MgB_2

The crystal structure of MgB_2 is presented in Figure 1. It is an AlB_2-like hexagonal structure with the in-plane lattice parameter a = 3.086Å and out-of-plane parameter c = 3.524Å [1]. The space group is P6/mmm. The MgB_2 unit cell is traced in red and can be described with the Mg at (0,0,0) and the B at (1/3, 2/3,1/2) and (2/3, 1/3,1/2). Essentially, B atoms in MgB_2 lattice form primitive two dimensional honeycomb-like layers similar to

graphene sheets stacked with no displacement, leaving large, nearly spherical pores for Mg [12]. Mg atoms whose size is much bigger than B occupy these pores between the B layers.

There are two types of atomic bonds which play important roles in the superconductivity of MgB_2: a covalent σ bonding in the B atomic plane and a ionic π bonding formed between Mg and B out of the B plane [12,13]. The superconducting energy gaps are 6.4-7.2meV for the σ band and 1.2-3.7meV for the π band at 4.2K [13,14]. The superconducting and normal-state properties of MgB_2 are strongly influenced by this two-band structure which leads to the anisotropic behavior in both the electronic and thermal properties, that have been observed in thin films [15] and single crystals [16].

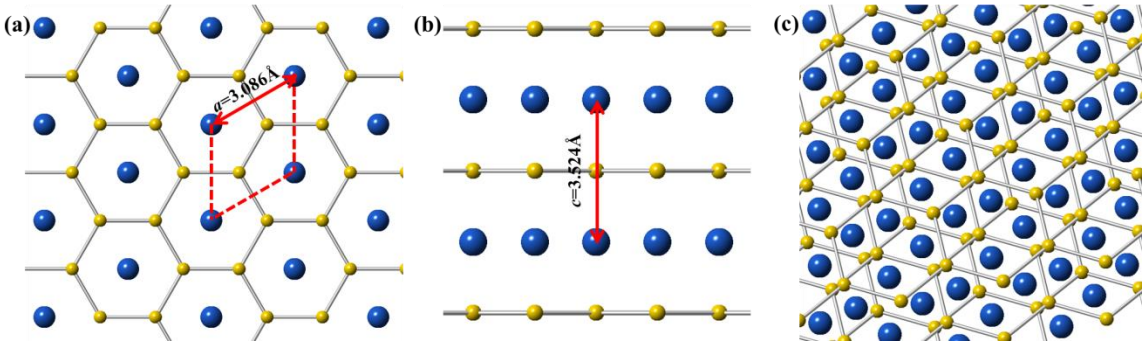

Figure 1 MgB_2 lattice structure (a) along the *c*axis; (b) along the *a or b* axis; c) from an arbitrary point. The blue spheres are Mg atoms and the yellow spheres are B atoms. The silver sticks represent the B-B bonding in the *a*-*b* plane.

1.3 Thermodynamics and Kinetics in MgB_2 Formation

The Mg-B binary phase diagram is presented in Figure 2 [17]. It is clear that even at very high temperatures, B has a very low solubility in Mg and vice-versa. Also, Mg has a low melting temperature (~ 650 ºC) and a boiling temperature (~ 1094 °C), compared to B whose melting temperature is ~2071 ºC. Without the use of high pressures and a confined system to prevent significant Mg loss, the temperature of MgB_2 synthesis in the literature is generally limited to ~600-900 °C. Besides MgB_2, there are other intermetallics present, namely, MgB_4 and MgB_7, with orthorhombic structures [18,19]. All of these borides are considered to be line compounds and are stable well above the boiling point of Mg. Since no superconductivity has been observed in MgB_4 or MgB_7, they can be treated as normal impurity phases that may block currents and reduce connectivity if present in the final product. Further, at 1atm, MgB_2 can decompose into MgB_4 and Mg at ~ 1174 ºC by the reaction of $2MgB_2 \Rightarrow MgB_4 + Mg$. This peritectic decomposition also limits the high temperature synthesis of MgB_2.

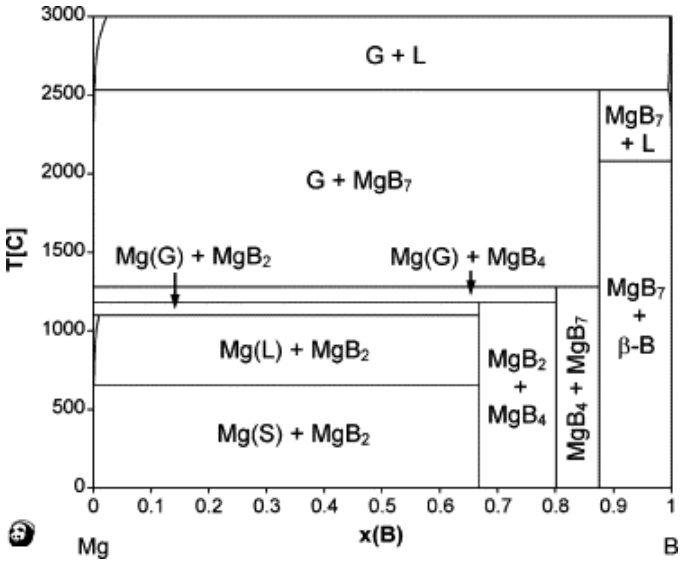

Figure 2 Mg-B phase diagram at 0.1MPa (1 atm) [17]. (Reprint with permission from Elsevier)

The semi solid-state formation of MgB_2 follows a shrinking core model [20,21]. During heat treatment, Mg first infiltrates into the B particles, reacts with B to form an MgB_7 shell. Then, this MgB_7 outer shell gradually transforms into MgB_4; finally, MgB_2 is formed with further diffusion of Mg through these outer layers [20,21]. The kinetics of this diffusion-controlled reaction were fully studied by embedding a pure B fiber (in which an amorphous B layer surrounded a W-B core) in liquid Mg and investigating the reaction at temperatures varying from 700 °C to 1025 ºC [20,21]. Two mechanisms were applied to explain the MgB_2 fiber formations: diffusion-controlled growth of cylindrical triple layers (MgB_7, MgB_4 and MgB_2) and radial growth of the cracks produced by the volume expansion, Figure 3. The diffusion coefficients of these intermetallics are so small that it is difficult to achieve full reaction of the MgB_2 phase under traditional experimental

conditions (600-900 °C, ~1atm). Therefore, B-rich impurities like MgB_4 and MgB_7 are very common in MgB_2 samples and may reduce the connectivity.

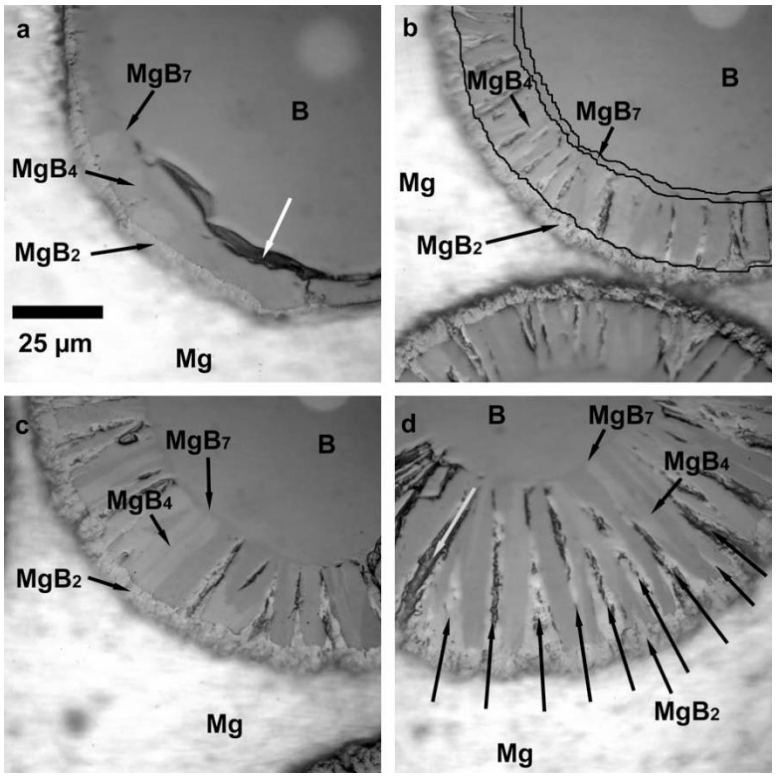

Figure 3 Images are optical micrographs of B fibers partially reacted with liquid Mg at 1000 °C for (a) 1 min, (b) 2 min, (c) 3 min and (d) 5 min [20].(Reprint with permission from APS)

1.4 Superconductivity in MgB_2

1.4.1 Fundamental Theories and Concepts of Superconductivity

Superconductivity was discovered in 1911 by Kamerlingh-Onnes and his collaborators [3]. They noticed that the electric resistivity in a solid mercury (Hg) wire vanished when it was immersed in liquid helium at 4.2 K. They named this phenomenon as “superconductivity” and defined the transition temperature as “superconducting critical temperature” T_c. Later they also found the vanishing of electric resistivity in tin, lead and some other pure metals.

In 1933, another unique phenomenon of superconductors called Meissner effect was discovered by Meissner and Ochsenfel [22]. By measuring the magnetic field distribution outside tin and lead in the presence of an applied magnetic field, they indirectly observed that below T_c the samples excluded nearly all of the applied magnetic fields. Their experiment demonstrated for the first time that superconductors exclude all magnetic flux from its body and exhibit perfect diamagnetism in a magnetic field. In fact, the magnetic field can penetrate the surface of the superconductor to a so-called penetration depth, λ which is on the order of 10^{-7} m. Within this surface layer, a persistent current (the screening current) flows, generating a magnetic field that cancels the external field. As a result, the material exhibits a perfectly diamagnetism. However, this perfect diamagnetism can break down when the applied magnetic field exceeds a critical field, the thermodynamic critical field, B_c. Under this condition the material is no longer superconductive.

The superconductivity of most conventional superconductors can be explained by the Bardeen-Cooper-Schrieffer (BCS) theory [26,27] proposed in 1957. In the BCS superconductive state, electrons near the Fermi surface intend to form so-called Cooper pairs via electron-phonon interaction. The formation of Cooper pairs leaves an energy gap

2Δ of the order of 1 meV at the Fermi level. Unlike electrons in the normal state which constantly experience the collision, these Cooper pairs or "superconducting electrons" can flow in the superconductor as a whole without collision. Thus, at temperatures below T_c, the thermal perturbation is not strong enough to break the Cooper pairs, so that superconductors exhibit zero resistivity. From the BCS theory, several important theoretical predictions were derived. One of them is the temperature dependence of the energy gap Δ according to [28]:

$$2\Delta(T \to T_c) = 6.14 k_B T_c \sqrt{1 - (T/T_c)} \quad (1)$$

where k_B is the Boltzmann constant ($k_B = 1.38 \times 10^{-23}$ J/K). In the framework of the BCS theory, the zero temperature gap Δ(0 K) is given by:

$$2\Delta(0K) = 3.5 k_B T_c \quad (2)$$

Also:
$$\Delta(0K) = 2\hbar\omega_D \exp\left(-\frac{1}{VN(E_f)}\right) \quad (3)$$

in which $\hbar$ is the reduced Planck constant, V is the phonon-moderated electron-electron interaction strength, $N(E_f)$ is the electronic density of states at the Fermi level and ω_D is the Debye frequency which is related to atomic mass m by [29,30]:

$$\omega_D \propto m^{-1/2} \quad (4)$$

Therefore, based on Eq. (2), Eq. (3) and Eq. (4), $T_c \propto m^{-1/2}$. This correlation between T_c and m has been experimentally observed, leading to an important property - the "isotope effect". The isotope effect is the experimental observation that for a given superconducting material, the critical temperature T_c is inversely proportional to the mass of the isotope used

in the material [28]. This effect was firstly reported independently by Maxwell *et al.* [31] and Reynolds *et al.* [32] in 1950. The choice of isotope ordinarily has little effect on the electric properties of a material, but does affect the frequency of lattice vibrations, which supports the notion that superconductivity is related to vibrations of the lattice. Many studies have focused on increasing the T_c values of existing superconducting materials based on the isotope effect. Two approaches are: (i) using lighter isotopes to fabricate the materials and (ii) using a lighter element with similar electronic properties to substitute for an original element by chemical doping. Various groups studying the isotope effect in MgB_2 [29,30] reported that different T_c values were observed in samples made by using the isotopes ^{10}B and ^{11}B. The lighter ^{10}B containing sample had a T_c of 40 K while the heavier ^{11}B sample had a T_c of 39 K. Smaller differences in T_c values were observed in samples made by using the Mg isotopes ^{24}Mg and ^{26}Mg [30].

Besides the BCS description of superconductivity is the Ginzburg–Landau (GL) theory. Developed by Ginzburg and Landau in 1950 [31], it became widely accepted after Gor'kov showed it to be derivable from the BCS theory in 1959 [32]. In GL theory, superconductors are characterized by two important lengths: the superconducting coherence length ξ and penetration depth λ. These lengths are given by:

$$\xi = \sqrt{\frac{\hbar^2}{2m|\alpha|}} \tag{5}$$

$$\lambda = \sqrt{\frac{m^2}{4\mu_0 e^2 \psi_0^2}} \tag{6}$$

where m is the effective mass of electron, α is a temperature dependent coefficient, e is the charge of an electron, μ_0 is the permeability in vacuum, ψ_0 is the equilibrium value of the order parameter in the absence of an electromagnetic field. In BCS theory the coherence length ξ can also be expressed in the form [28]:

$$\xi = \frac{\hbar v_f}{\pi \Delta} \tag{7}$$

where v_f is the Fermi velocity. The coherence length ξ estimates the average spacing between two correlated electrons in a Cooper pair. In practical superconductors, crystalline defects are commonly present. Thus, taking electron scattering caused by defects into account, the effective coherence length ξ is related to the mean free path l through the equation:

$$\xi = \left(\frac{1}{\xi_0} + \frac{1}{l}\right)^{-1} \tag{8}$$

where ξ_0 is the coherent length in a clean superconductor [35]. Therefore, ξ decreases with decreasing l.

Compared to normal conductors, superconducting materials can carry very high current densities. However, this current-carrying ability has an intrinsic upper limit. According to GL theory, this limit is termed by depairing current density J_d, the theoretical

maximum supercurrent density at which the Cooper pairs will be depaired and become normal electrons. J_d can be expressed by [28]:

$$J_d = \frac{B_c}{\mu_0 \lambda} \tag{9}$$

in which B_c is the previously mentioned thermodynamic critical field. The current-carrying ability of superconductors is characterized by the so-called critical current density J_c, defined as the maximum current that can be carried in a unit area of the superconductor without loss of its superconductivity. Its value is much smaller than J_d. The J_d of MgB_2 is comparable to that of other superconductors. For example, at 4.2K and 0 T, J_d=~8.7×10^8 A/cm^2 for MgB_2 [36], ~3×10^8 A/cm^2 for the cuprate superconductors and 3.6–77×10^7 A/cm^2 for the Nb alloys and intermetallics [6]. However, unlike cuprate- and Nb-based superconductors whose J_c values at 4.2 K have already achieved about 5-15 % of their J_d values, the typical J_c is only about 1-5 % of J_d for MgB_2 [6] (except in the case of clean thin films [36]).

Superconductors can be divided into two categories based on their in-magnetic-field behaviors [28]. Type-I superconductors show perfect diamagnetism (Meissner effect) in the presence of an applied magnetic field ($B < B_c$) and their superconducting state is destroyed when the whole material is penetrated by the magnetic field ($B > B_c$). The critical field B_c and critical temperature T_c in Type-I superconductors are related by [28]:

$$B_c(T) = B_c(0)\left[1 - (\frac{T}{T_c})\right] \tag{10}$$

The in-field superconducting behavior of a Type-II superconductor is similar to Type-I when B is smaller than a certain value called the lower critical field B_{c1} (typically of order 10-20 mT). However, when B becomes larger than B_{c1}, a so-called "mixed state" of superconducting and normal regions exists due to the negative interfacial energy of the boundaries between the superconducting and the normal regions. The radius of these normal cores approximately equals the coherence length ξ, and there is a "flux-line" with a magnetic field B inside each normal core. The flux-line inside the normal core is generated by a persistent current loop (or current vortex) flowing around the core with a rotation opposite to the screening current. As a result, all cores repel each other and form a hexagonal lattice called the flux-line lattice (FLL), represented in Figure 4. The "lattice constant a" of this flux-line lattice [28] is given by:

$$a = 1.07\left(\frac{\Phi_0}{B}\right)^{1/2} \tag{11}$$

in which Φ_0 is the quantum of magnetic flux ($\Phi_0 = 2.07\times10^{-15}$ Wb). As B increases, a is reduced which means the normal cores are closer. Thus the normal state region grows larger by forming more and more normal core, while the superconducting matrix becomes smaller. When all of the superconducting regions disappear, the whole superconductor is in the normal state. The magnetic field at which this happen is the upper critical field B_{c2}. Abrikosov [37], based on the GL theory, showed the formation of the FLL and provided the following expressions for B_{c1} and B_{c2}:

$$B_{c1} = \frac{\phi_0}{4\pi\lambda^2}\ln(\kappa) \tag{12}$$

$$B_{c2} = \frac{\phi_0}{2\pi\xi^2} \tag{13}$$

The thermodynamic critical field is given by:

$$B_c = \frac{\phi_0}{2\sqrt{2}\xi\lambda} \tag{14}$$

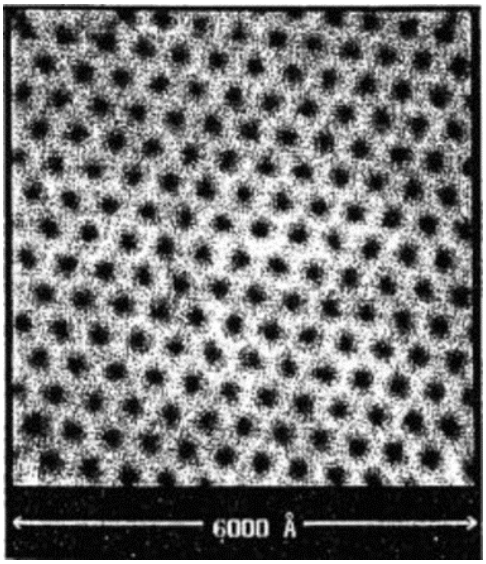

Figure 4 Vortices in $NbSe_2$ defined by scanning tunneling microscopy (STEM) [38]. (Reprint with permission from APS)

The Ginzburg-Landau (GL) constant κ of a material frequently used to specify the type of superconductivity is given by:

$$\kappa = \lambda/\xi = B_{c2}/\sqrt{2}B_c \tag{15}$$

If $\kappa < 1/\sqrt{2}$ such that $B_{c2} < B_c$, the interfacial energy between the superconducting and normal regions is positive, so that the mixed state is not energetically favorable (Type-I, Figure 5 top); otherwise the interfacial energy is negative (Type-II, Figure 5 bottom). MgB_2

is quite unique due to its two-band structure [39,40,41]. For its σ band, the coherent length ξ_σ is about 6-13 nm and the penetration length λ_σ is about 48 nm at 0 K, therefore the GL constant κ_σ for the σ band is much larger than 0.71 which leads to a Type-II behavior in the B-B plane. Conversely, for the π band, ξ_π is about 50 nm and λ_π is about 34 nm at 0 K, so that κ_π for π band is smaller than 0.71 [41]. Although both the π band and the σ band play important roles in the superconductivity of MgB_2, the dominant contribution comes from the strong σ band scattering unless *T* is very close to 0 K [42-44]. Therefore, MgB_2 can be safely treated as Type-II superconductor in most situations.

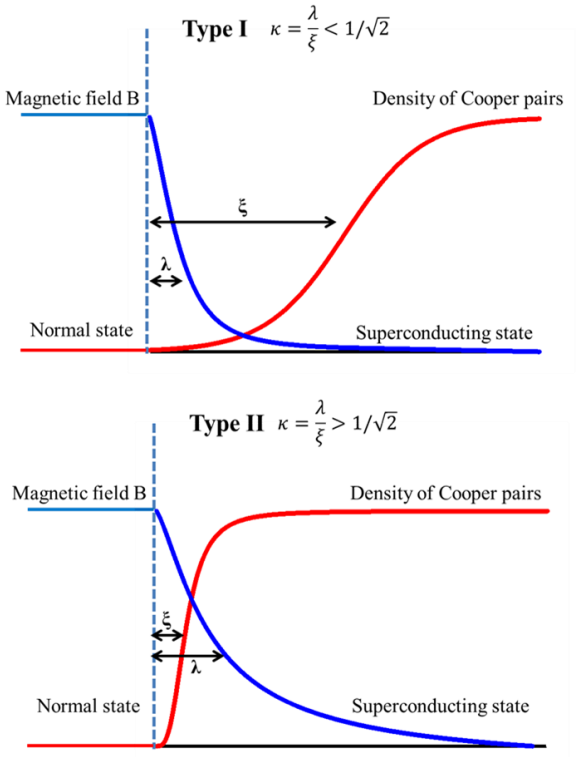

Figure 5 The interface between superconducting region and normal region of (top) Type-I and (bottom) Type-II. (Pictures were drawn by Yuan Yang)

Now all three important parameters in evaluating the superconducting properties of a Type-II practical superconductor have been explained and derived: (i) the critical current density, J_c; (ii) the upper critical field, B_{c2}; and (iii) the superconducting transition temperature, T_c. Figure 4 shows the superconducting phase diagram of MgB_2. When its J, T and B stay below the critical surface in Figure 6, MgB_2 is in the superconducting state.

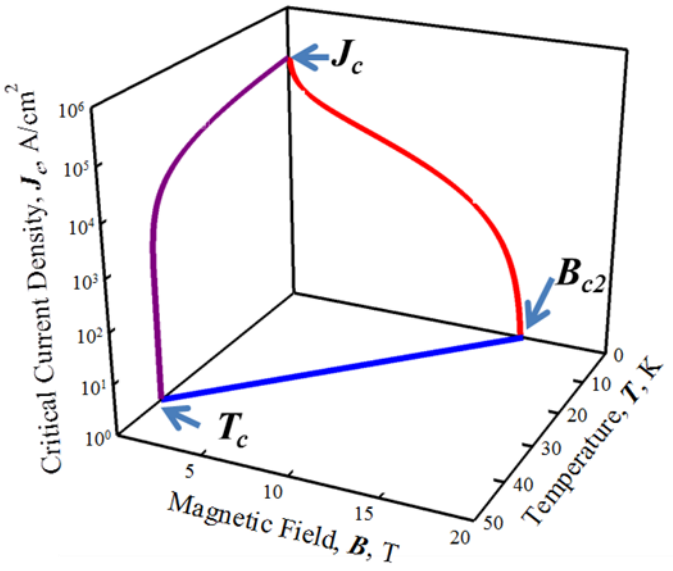

Figure 6 Critical surface of a typical MgB_2 superconductor characterized by J_c, B_{c2} and T_c.

1.4.2 Upper Critical Field B_{c2} and Irreversibility Field B_k in MgB_2

As mentioned in above, B_{c2} is the maximum field under which a type-II superconductor can be used. One of the most important applications of a type-II superconductor is transporting current under high external magnetic fields. A very high B_{c2}

is desirable. Commonly in a single-band superconductor described by the single-band BCS theory, the 0 K B_{c2} can be expressed by [28]:

$$B_{c2}(0K) = -0.68T_c(dB_{c2}/dT)_{T_c} \quad (16)$$

Thus, the 0 K B_{c2} is 68% below the linear extrapolation to 0 K of the B_{c2}-T curve at T_c. Thus a downward curvature of $B_{c2}(T)$ is expected when T approaches 0 K. On the other hand, for MgB_2 an upward curvature of B_{c2}–T at low temperatures has been observed by many authors [45]. This deviation was explained by Gurevich *et al.* [42,44] using a bilayer model in terms of electronic diffusivities, D_σ and D_π, for each band, respectively. Based on the BCS theory in the dirty limit for MgB_2, the temperature dependence of B_{c2} is given by:

At T = 0 K
$$B_{c2} \propto \frac{T_c}{\sqrt{D_\sigma D_\pi}} \quad (17)$$

At T near T_c
$$B_{c2} \propto \frac{T_c - T}{a_\sigma D_\sigma + a_\pi D_\pi} \quad (18)$$

where a_σ and a_π are the electron–phonon coupling constants. Figure 7 shows the B_{c2}– based on the bilayer model. From Eq. (17) and Eq. (18), when T_c is a constant, B_{c2} near T_c is dominated by $(a_\sigma D_\sigma + a_\pi D_\pi)$, while B_{c2}(0 K) is dominated by $\sqrt{D_\sigma D_\pi}$. In the limit of very different diffusivities, the maximum of D_σ and D_π controls the B_{c2} behavior near T_c, while the minimum of D_σ and D_π determines B_{c2} at 0 K. Thus, based on Gurevich's theory, in order to improve the B_{c2} over the whole temperature range, it is necessary to reduce the values of both D_σ and D_π. The electronic diffusivity D for one band is given by [47]:

$$D = 2\pi T_c \xi^2 \quad (19)$$

To reduce *D*, one can reduce the effective coherence length ξ. Based on the equation (8), ξ can be reduced by introducing more defects to enhance electron scattering and reduce the electron mean free path *l* into the crystal lattice. Gurevich's work provides an important guideline: inducing impurity scattering is beneficial to B_{c2} over the entire temperature range in MgB_2.

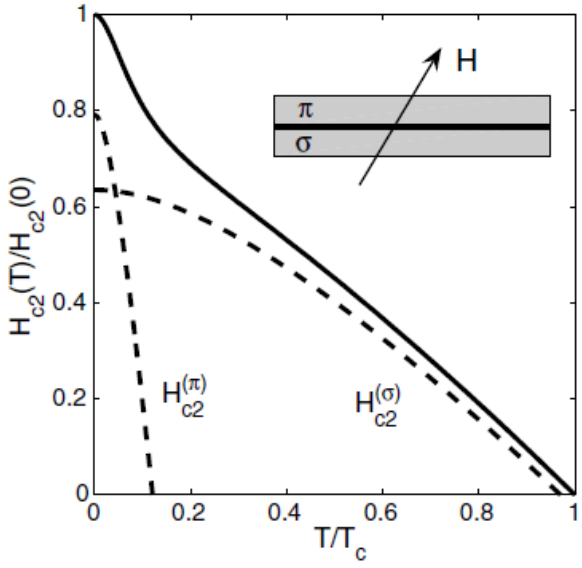

Figure 7 B_{c2}-*T* (solid line) for MgB_2 illustrated by the bilayer model shown as inset. The dash lines indicate the B_{c2}(T) curves for the σ and and π band based on the single-band BCS theory under dirty limit [44] (Reprinted with permission from Elsevier).

Due to the two-band structure of MgB_2, it is not surprising to observe anisotropic behavior in B_{c2}. In pure MgB_2 single crystals, the 0 K B_{c2} to the B plane ($B_{c2}^{\parallel}$) is about 15-25 T and the B_{c2} to the B plane ($B_{c2}^{\perp}$) is about 3-9 T, giving an anisotropic factor $\gamma =$

$B_{c2}^{\parallel}/B_{c2}^{\perp} \approx 1.7 - 6.5$ [48-51]. Both B_{c2} values are rather low, compared to the B_{c2}(0 K) = ~ 30 T for Nb_3Sn [6] and ~ 120 T for YBCO [7].

The B_{c2} of MgB_2 can be enhanced by chemical doping. The numerous studies focusing on the use of chemical dopants to enhance its B_{c2} have culminated in a record value of $B_{c2}^{\parallel}(0K) = \sim 70$ T [52,53] in a C-doped MgB_2 thin film, a value that exceeds the B_{c2} of Nb-based superconductors [6]. Very high B_{c2} values have also been observed in MgB_2 polycrystalline bulk and wires. Serquis *et al.* [54] reported B_{c2}(0K) = 44.4 T in carbon nanotube (CHT) doped MgB_2 polycrystalline bulk samples. Dou *et al.* [55] reported a B_{c2}(0K) of 35 T in a SiC-doped MgB_2 wire. However, the effective B_{c2} of polycrystalline MgB_2 is complicated by the existence of anisotropy and randomly orientated grains. A current-percolation theory developed by Eisterer *et al.* [56] theoretically explains the influence of the anisotropic B_{c2} on the J_c of polycrystalline MgB_2. Although the B_{c2}s of the MgB_2 superconductors (bulk samples and wires) are still below those of thin films, further improvement of B_{c2} by chemical doping is feasible and necessary.

The irreversibility field B_k of a superconductor is defined as the magnetic field at which its J_c decreases to zero. Therefore, B_k is a very important parameter in practical terms as it describes the upper limit of in-field current-carrying ability. The relation between B_{c2} and B_k is material-dependent. In low-temperature superconductors (LTS), e.g. NbTi and Nb_3Sn, there is no real difference between B_k and B_{c2} [57], while in high-temperature superconductors (HTS), e.g. YBCO and BSCOO, B_k is about 80 % - 90 % of B_{c2} [58,59]. In MgB_2, the several factors that can significantly affect B_k include anisotropy γ, electric

connectivity K, and inhomogeneity, therefore large differences have been observed between the values of B_{c2} and B_k, in particular, B_k = 0.3-0.9B_{c2} [50,52,55,60-62].

Experimentally, B_{c2} can be obtained by two methods: (i) resistivity measurement, where the resistivity ρ is determined as functions of T and B; and (ii) magnetization measurement, where the magnetization is measured as functions of T and B. The details will be described in chapter 2. There are several ways to determine the B_k. In this work, a widely accepted method, the Kramer plot was used [63,64]. In this method the B-intercept of a linear fitted plot of $J_c^{0.5}B^{0.25}$ vs. B [63,64] is taken as the irreversibility field B_k, Figure 8. This method is based on the grain boundary pinning function to be described in the following Section.

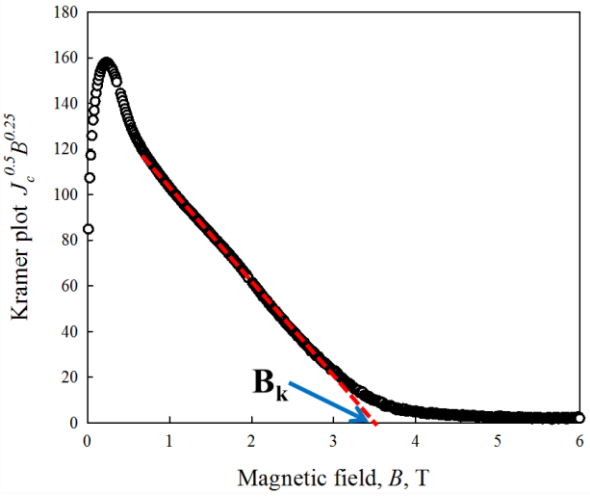

Figure 8 A typical Kramer plot of a MgB_2 sample describes the determination of B_k. The red dash line indicates the linear fitting.

1.4.3 Flux Pinning in MgB_2

Flux pinning is essential to the existence of the superconducting current in a Type-II superconductor in the presence of a magnetic field. As mentioned in Section 1.3.1, a Type-II superconductor exposed to a magnetic field between B_{c1} and B_{c2} forms a mixed state with a hexagonal flux-line lattice. When transport current flows through a Type-II superconductor in the mixed state, an electromagnetic interaction – specifically the Lorentz force - between the current and the flux-line lattice (FLL) is generated, Figure 9. In the absence of restraint, this force would cause the flux-lines to move. This movement leads to a voltage drop parallel to the transport current direction, i.e. a macroscopic resistive behavior. However, if the Lorentz force is balanced by an opposing force, the flux-line lattice will not move, no resistive behavior shows up, and the material remains superconducting. Flux pinning theory is based on the following assumptions: the flux-line lattice is "pinned" by "pinning centers" that provide a flux pinning force which counters the Lorentz force, so that the material can stay in the superconducting state. The bulk pinning force density F_p is usually characterized by the strength of the pinning per volume and represents an averaged summation of all elemental pinning forces, thus $F_p = J_c \times B$. If the pinning strength is increased, the superconductor can carry a higher transport current.

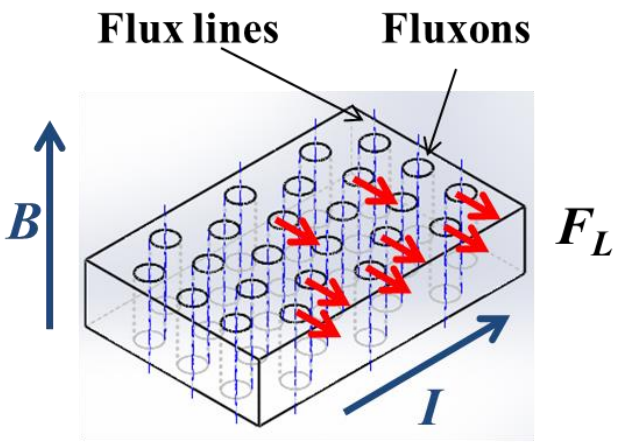

Figure 9 Schematic diagram of the relationship between the transport current, *I*, the applied field, *B*, and the Lorentz force, F_L, on the flux lines.

Consider the case where normal state spherical defects with an average diameter *x* (assume a simple case, x > 2ξ where ξ is the coherence length) work as pinning centers in a mixed state Type-II superconductor in an external field B. The increase of volumetric free energy in the defects, due to the present magnetic field, is ${B_c}^2/2\mu_0$ with respect to the superconducting matrix which has no magnetic field inside. Also, as mentioned in Section 1.3.1, since the Type-II superconductor is in a mixed state, the normal cores and superconducting matrix coexist. There is also a magnetic field B inside these normal cores. If a normal core with a radius of ξ is "trapped" in one of these defects, the free energy of the overlapped volume would be reduced by $\sim(\pi\xi^2 x)({B_c}^2/2\mu_0)$. Therefore, the normal cores in Type-II superconductors are energetically favored to be pinned at the defects. The maximum pinning force generated by these pinning centers can be expressed in terms of the gradient of the pinning potential *U*. Thus the pinning force f_i of a pining center *i* is given

by $f_i = \partial U / \partial x$. Generally, the pinning is formed by non-superconducting particles, precipitates, voids, and grain boundaries, and this type of pinning is commonly referred as normal pinning.

Flux pinning behavior is field dependent. When a Type-II superconductor is exposed to a field B > B_{c1}, the FLL forms with a lattice parameter *a* given by the equation (12). At the early stage, *a* is very large and there are less fluxons than pinning centers. Therefore, it is engertically favorable for each fluxon to interact with a distinct pinning center until the number of fluxons equals the number of pinning centers. The total pinning force per unit volume is the single pinning force multiplied by the number of active pins per unit volume. As B increases, *a* is smaller and the fluxons outnumber the pinning centers. The situation becomes complicated. Two models haven been developed to explain pinnning mechanism and estimate the flux pinning force: the flux line shear model [63,64] and the core pinning model [65,66].

The flux-line shear model by Kramer [64] assumes that the mutual repulsion between fluxons which result in flux shearing process. This model considers regions wherein fluxons are pinned by planar pins, and there are more fluxons than pinning centers, thus some flux lines are strongly held in place by pinning centers while the remainder are held in place by the mutual repulsion between fluxons. As the current (and hence the Lorentz force) is increased, the FLL is elasically deformed until either the lattice breaks and starts to move as a whole or the repulsion between fluxons is overcome and the unpinned fluxons shear past these pinned fluxon. Therefore, the elastic shear modulus C_{66} which describes the stiffness of the FLL to the shear of fluxons past each other determines

critical current density J_c of a Type-II superconductor. The elastic shear modulus C_{66} and the flux pinning force density F_p in the flux-line shear model are given by [64]:

$$C_{66}=7.4\times10^{-3}(\frac{B_{c2}}{\mu_0\kappa})^2(1-b)^2 \tag{20}$$

$$F_P = \frac{C_{66}}{12\pi^2 a(1-a/D)^2} \tag{21}$$

where b is the normalized magnetic field,B/B_{c2}. Using the FLL constant a from Eq. (12) and the Ginzburg-Landau constant κ from Eq. (15), the flux pinning force density can be expressed as:

$$F_P \propto \frac{1}{(1-a/D)^2} b^{1/2}(1-b)^2 \tag{22}$$

This predicted function, the so-called "the scaling law", has been observed in many superconductors. However, it has two main drawbacks. Firstly, it predicts a weak dependence on the grain size (thus pin density) which disgrees with experimental observatons [66-68]; secondly, the expression for C_{66} is an proximation only valid at very high fields ($b \rightarrow 1$).

The core pinning model by Dew-Hughes [65] considers the interaction between pin core and flux line. Based on the comparison between the flux-line lattice parameter a and the pin size d, one can define "point pins" whose dimensions in all direction are less than a, "surface pins" in which two dimensions are larger than a, and "volume pins" where all dimensions exceed a. Therefore, only one flux-line can interact with point pins, but surface pins and volume pins can interact with multiple flux-lines.

Flux pinning plays an essential role in transport properties of MgB_2 superconductors. The first report of flux pinning in polycrystalline MgB_2 was by Larbalestier *et al.* [60] who found that MgB_2 followed the grain boundary pinning mechanism, similar to the intermetallic Nb_3Sn. Larbalestier also noticed that this pinning behavior did not show a strong temperature dependence. By using magneto-optical, polarized light, and analytical scanning electron microscopy, he presented an interesting comparison which showed direct evidence of significant superconducting inhomogeneity and few intra-granular contributions to the flux pinning, see in Figure 10.

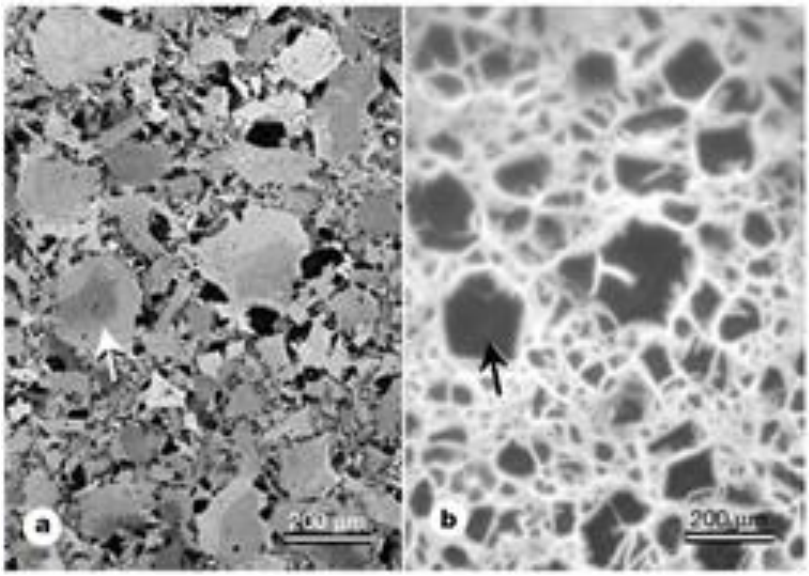

Figure 10 (a) Polarized light image of MgB_2 sample; (b) magneto-optical images of the same area of the MgB_2 sample [60]. (Reprinted with permission from Nature Publishing Group)

Following Larbalestier, many authors [48,50,51,68-70] have proved that MgB_2 polycrystalline samples mainly follow the grain boundary pinning mechanism which

belongs to the normal surface pinning category; other evidence shows that under special conditions, the normal point pinning and normal volume pinning mechanisms might also be at play [11,55,70]. The important bulk flux pinning force formulas according to the Dew-Hughes model in MgB_2 are:

Normal Point Pinning
$a > d$ in 3 dimensions

$$F_P = \frac{V_f B_{c2}^2}{4.64\mu_0 d\kappa^2} b(1-b)^2 = \frac{V_f B_c^2}{2.32\mu_0 d} b(1-b)^2 \quad (23)$$

Normal Surface Pinning
$a > d$ in 2 dimensions

$$F_P = \frac{S_v B_{c2}^2}{4\mu_0 \kappa^2} b^{1/2}(1-b)^2 = \frac{S_v B_c^2}{2\mu_0} b^{1/2}(1-b)^2 \quad (24)$$

Normal Volume Pinning
$a < d$ in 3 dimensions

$$F_P = \frac{S_v B_{c2}^2}{5.34\mu_0 \kappa^2} (1-b)^2 = \frac{S_v B_c^2}{2.67\mu_0} (1-b)^2 \quad (25)$$

in the above a is the flux-line lattice parameter, d is the pin size, V_f is the volume fraction of the flux line within the pinning centers and S_v is the effective surface for pinning ($S_v \propto 1/D$). The normalized bulk pinning force functions described by the equations (23) – (25) are presented in Figure 11.

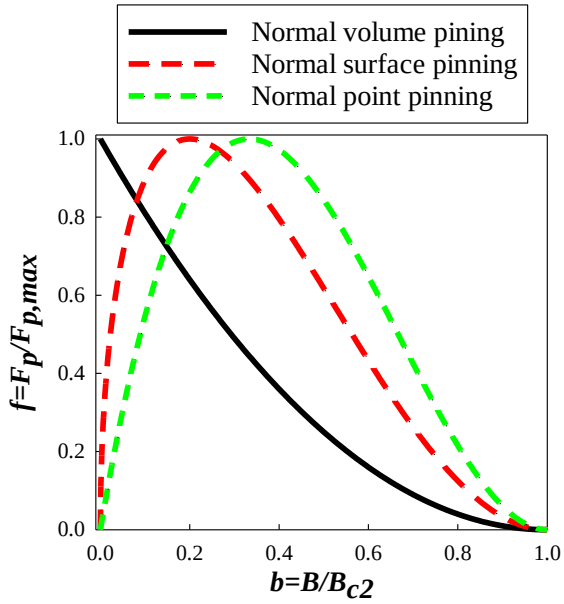

Figure 11 Three normalized bulk pinning function curves, Dew-Hughes [38].

Flux pinning in MgB_2 polycrystalline samples has been studied, for example, by Martinez *et al.* [68] and Mikheenko *et al.* [69]. Martinez focused on various preparation techniques used to synthesis MgB_2 samples at temperature ranging from 640 ºC to 1000 ºC. The MgB_2 grain size, *D*, varied from 50 nm to 2 μm due to the differences in the sample preparation conditions. Martinez reported a linear behavior in the J_c vs. *1/D* curves at 20K and 2 T and claimed this observation as direct proof of grain boundary pinning in MgB_2 polycrystalline samples. Martinez [68] studied MgB_2 samples made by various starting powders, including *in situ* (Mg and B powders), *ex situ* (commercial MgB_2 powder), mechanically alloyed Mg + B, as well as samples that included numerous nanoparticle dopants (30 nm SiC, 30-50 nm TiO_2, 30-50nm Al_2O_3, 30-50 nm $BaTiO_3$,). In order to eliminate porosity's influence on J_c, a hot isostatic pressing (HIP) method was performed

to make very dense MgB_2 bulk samples. Also, the variations in MgB_2 grain size were controlled by changing the pressure during cooling. Polarized optical microscopy and electron backscatter diffraction were used to verify the misorientation between the MgB_2 grains and the average grain size D as calculated assuming circular grains. In agreement with Martinez, Mikheenko also observed a $1/D$ dependent J_c in MgB_2 bulk samples in various fields indicating the dominance of grain boundary pinning. He also found that the frequently observed misorientation angles between MgB_2 grains were 19.3º, 24.9º, 26.7º, 28.1º, 49.7º, 53.4º, 71.7º and 84.5º (above 15º) in pure MgB_2 bulk samples. This observation indicated that the high angle grain boundaries were very effective in flux pinning.

1.4.4 Weak-linking of Superconductors

The weak-link issue is very serious in cuprate HTS materials (e.g., YBCO and BSCCO) due to their relatively small coherence length ξ. Cooper pairs (and therefore the supercurrent) cannot pass the boundaries thicker than ξ. The coherence length in YBCO and BSCCO is ~ 1.0 nm which is very close to the width of their grain boundaries. The relatively large coherence length of MgB_2 (above 6-13 nm in the B plane at 0 K, about 10-15 times larger than the size of MgB_2 unit cell) renders its grain boundaries transparent to the superconducting electrons. So MgB_2 suffers no grain-boundary weak-link problems. The absence of weak-links together with the grain boundary dominated flux pinning

discussed in Section 1.3.2 makes MgB_2 a very promising superconductor whose ability to be used in its polycrystalline form significantly reduces the costs of large-scale application.

1.4.5 Electric Connectivity and Porosity in MgB_2

The electric connectivity *K* of a superconductor is defined as the effective fraction of its cross-section area able to carry supercurrent. Low connectivity is a critical issue in MgB_2, as it strongly limits its macroscopic superconducting performance. Typically, the connectivity of *in situ* MgB_2 bulk and wire has been calculated to be only about 7-17 % [71-73]. Figure 12 shows the typical porous structure of the transverse cross-section of an *in situ* MgB_2 powder-in-tube (PIT) wire. If the connectivity could be increased, J_c would be also increased. Among the various factors shown to be responsible for this low connectivity are the volume shrinkage during formation and the existence of impurity phases.

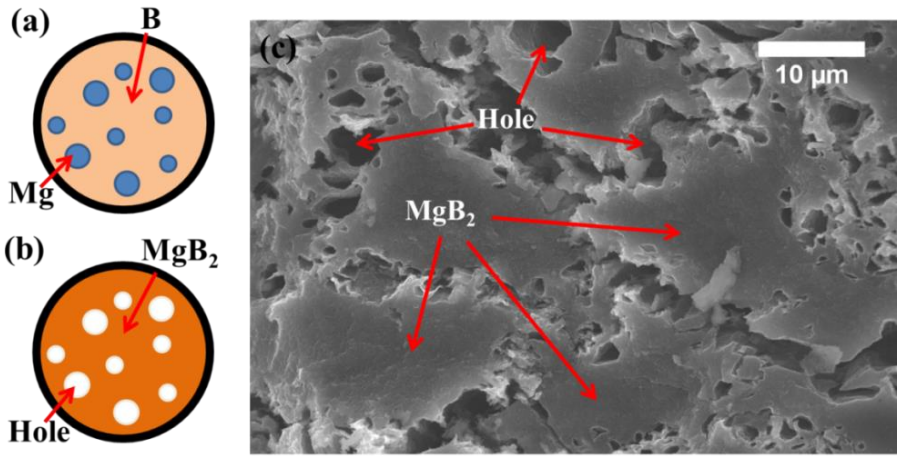

Figure 12 Schematic of an *in situ* MgB_2 PIT wire (a) before reaction and (b) after reaction. (c) Secondary electron imaging (SE) by through-the-lens detection (TLD) on fractured surfaces of an in situ MgB_2 PIT wire.

The *in situ* formation (from Mg and B) of MgB_2 naturally creates a porous structure due to the shrinkage during the reaction between Mg and B. The elemental molar volumes of Mg, B and MgB_2 are 13.74 cm^3/mol, 4.63 cm^3/mol and 17.21 cm^3/mol, respectively [11]. A stoichiometric mixture of Mg and B powders therefore has a molar volume of 23 cm^3/mol, significantly more than that of the final product, MgB_2. Based on these data, even a fully dense Mg and B powder mixture would react to a 25% porous MgB_2. In the real world, the porosity of practical MgB_2 samples is much higher because full packing of the unreacted powder mixture is not achievable. High porosity substantially reduces the effective cross-sectional area of the material and decreases its capability of carrying supercurrent.

Beside the volume shrinkage after the MgB_2 formation, impurity phases play important roles as well. Normally, resistive impurities significantly reduce the connectivity

of MgB_2. In some cases, though, they can be beneficial [55,74,75]. It has been shown that a limited number of impurity phases with the appropriate size can form flux pinning centers hence increase J_c. Oxides in the raw materials are very common and hard to avoid; Mg and B can react with O under ambient to form $MgO/Mg(OH)_2$ and B_2O_3 [76], e.g. Figure 8. Also, as mentioned in chapter 1.1, the boride-rich phase, MgB_4, is another common impurity whose formation during the synthesis of MgB_2 is hard to avoid. Mg is easily vaporized during the heat treatment, resulting in Mg deficiency and the formation of MgB_4; also, the formation of MgB_2 is based on Mg diffusing into the pre-formed MgB_4 and MgB_7 solid shells, so it is very hard to transform all of the MgB_4 into MgB_2. According to [8,77,78], the volume fraction of MgB_4 in MgB_2 bulk can vary from ~ 1.5 to 5%. Other impurities may be introduced by doping or may be found within the starting materials. Some impurities reduce the intergranular connectivity of MgB_2. Other impurities of appropriate size can act as flux pinning centers and enhance the bulk flux pinning force density. Still others may partially substitute for the Mg or B atoms in MgB_2 lattice to increase the upper critical field B_{c2}. Both of the latter serve to increase J_c. However, except for carefully selected chemical dopants or a limited number of samples made under special experimental conditions, the negative effects of impurities in MgB_2 generally overwhelm the positive and lead to decreases of J_c.

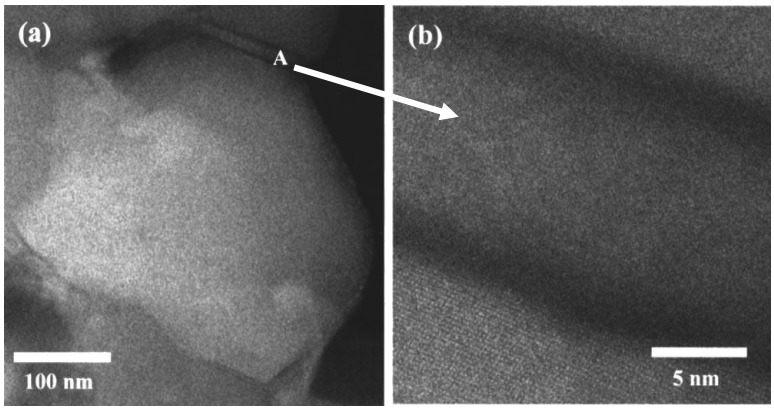

Figure 13 High resolution TEM of a single-phase grain. (a) MgO layer at grain boundary A. (b) enlarged A area [76]. (Reprinted with permission from Elsevier)

The connectivity issue was firstly reported by Rowell [79] who noticed that MgB_2 samples with a larger amount of oxide impurities (e.g., MgO and B_2O_3) generally had a higher normal-state resistivity. He deduced that this high resistivity resulted from low electrical connectivity between MgB_2 grains, caused by these oxides which reduced the effective cross-section area for the passage of supercurrent. The relationship between connectivity, *K*, and the temperature-dependent resistivity $\rho(T)$ is given by:

$$\rho(T)=[\rho_0+\rho_t(T)]/K \tag{26}$$

where ρ_0 is a residual resistivity and $\rho_t(T)$ is temperature-dependent resistivity component caused by lattice vibration (electron-phonon scattering). By using resistivity data from MgB_2 single crystals, Rowell established a method of estimating the connectivity, *K*. After measuring the resistivity at 50 K and 300 K, the connectivity is obtained by substitution into the following equation:

$$K=\Delta\rho_{sc}/[\rho(300\text{ K})-\rho(50\text{ K})] \quad (27)$$

in which $\Delta\rho_{sc}$ is the change in resistivity from 300 K to 50 K of a fully connected MgB_2 single crystal, i.e. $\Delta\rho_{sc} = \rho_{sc}(300\text{ K}) - \rho_{sc}(50\text{ K}) = 4.3\ \mu\Omega\cdot\text{cm}$.

Matsushita *et al.* [80] applied Rowell's analysis to a series of MgB_2 samples fabricated to various packing densities and under various reaction conditions. The correlation between the self-field J_c at 20 K and K presented in Figure 14, supports Rowell's hypothesis of connectivity-controlled J_c in MgB_2.

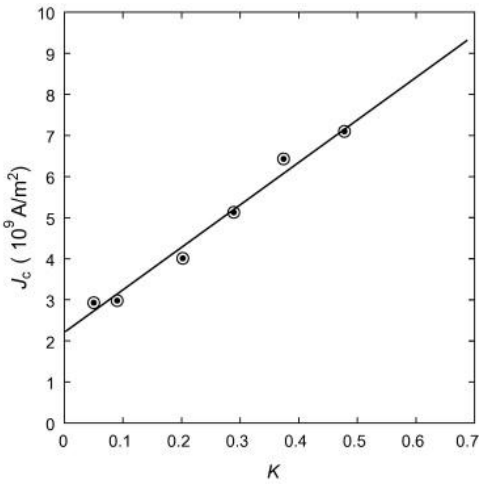

Figure 14 Relationship between the critical current density in self field at 20 K and the electric connectivity. The line simply shows the trend [80]. (Reprinted with permission from Elsevier)

1.5 Chemical Doping in MgB_2

Of the many methods that have been performed in the fabrication of MgB_2 in order to enhance its intrinsic properties, chemical doping by far is one of the most effective. As

summarized by Collings *et al.* [11], numerous chemicals have been considered and used as dopants to improve the intrinsic properties of MgB_2. Chemical dopants can be classified into five categories, dopants that: (1) partially substitute for either the Mg or B atoms in the MgB_2 lattice; (2) form new pinning centers; (3) cause lattice distortion introduced by coherent precipitation; (4) modify the grain size as grain growth inhibitors; and (5) improve intergranular connectivity by cleaning grain boundaries. Also, two significant disadvantages associated with doping must be addressed: (1) the formation of impurity phases which can reduce the intergranular connectivity; (2) the existence of doping inhomogeneity. One dopant may perform several functions, and can have positive and/or negative effects. This Section focuses on the three main dopant categories: C and C-containing compounds, metal and metal-containing borides, and rare earth oxides, Table 1.

Table 1 List of C and C-containing compounds, metal and metal-containing borides, and rare earth oxides added to MgB_2

C and C-containing	Metal and Metal borides		Rare earth oxides
	Al [94,103-109]	Ti [176]	
	Mo [178]	Zr [176,176]	
	Fe [179]	Ni [183]	
Direct C [82]	Co [177,182]	Cu [180]	Y_2O_3 [118]
C nano-tubes [54]	Ag [181]	Mn [182]	Dy_2O_3 [119]
TiC [174]	Sn [184]	Ni [183]	Nd_2O_3 [120]
SiC [55,70,74,75,88,100]	W [186]	La [185]	Ho_2O_3 [121]
B_4C [176]	Bi [187]	Te [187]	CeO_2 [189]
Carbohydrates [89-91]	Se [187]		Sb_2O_3 [190]
	AlB_2 [188]	TiB_2 [87,148, 149]	
	TaB_2 [188,191]	ZrB_2 [87,164, 165,188]	
	VB_2 [188]	NbB_2 [87]	

1.5.1 Carbon Doping in MgB_2

Shortly after the discovery of superconductivity in MgB_2, Takenobu *et al.* [81] reported that in C doped MgB_2 bulk samples, the T_c as well as the in-plane lattice parameter *a* decreased with increasing C concentration, but the out-of-plane lattice parameter c was more-or-less insensitive to it (Figure 15).

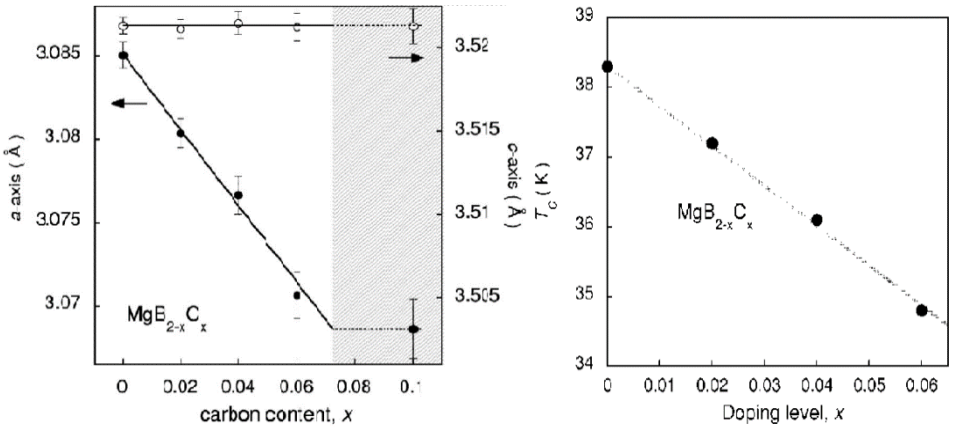

Figure 15 Variations in lattice parameters (left) and T_c (right) with increasing C composition in $MgB_{2-x}C_x$ [81]. (Reprinted with permission from APS)

Further studies on C-doped MgB_2 single crystals were performed by Lee *et al.* [82] and Masui *et al.* [83]. As with the MgB_2 polycrystalline samples, the lattice constant *a* and the T_c of the MgB_2 single crystals also decreased with C doping, leaving the lattice constant *c* unchanged. Moreover, they found that despite the suppression of T_c the B_{c2} was significantly increased by C doping [83,84]. This phenomenon, observed by other authors

as well [86], was important in its being the first time that chemical doping was shown to benefit the superconductive properties of MgB_2.

Subsequently the C doping of MgB_2 thin films and polycrystalline samples were the foci of many groups and many C-doping techniques were developed. One of the earliest methods was SiC doping. SiC can react with Mg to form Mg_2Si and C at ~524 °C [11]. This C is very reactive and can substitute for B atoms at relatively low temperatures [11]. A homogeneous distribution of C can be achieved by the inclusion of very small and evenly distributed SiC particles in the initial powder mixture. A series of nano-particle SiC-doped MgB_2 bulk samples was prepared by Dou *et al.* [55,74,75]. Beside the C substitution for B, Dou observed inclusions which were presumably Mg_2Si with a size of ~2-10nm, as well as a high density of dislocations, widely distributed inside the MgB_2 grains (Figure 16). He reported that the high dislocation density induced by substitution was the dominant source of flux pinning, rather than the nano-size intragranular inclusions which acted as point pinning centers and were weak at high magnetic fields. Following Dou, Shi *et al.* [70] presented a study of nano-size SiC doped MgB_2 wires. Based on transport measurements, they found that two pinning mechanisms, grain boundary pinning and point pinning, contributed to the bulk pinning force of SiC doped MgB_2 wires. Our group has also investigated the effect of SiC doping in MgB_2 wires. Bhatia *et al.* [8,87] and Sumption *et al.* [88] have shown that SiC doping can increase the B_{c2} of metal-sheathed PIT MgB_2 strands up to more than 30 T.

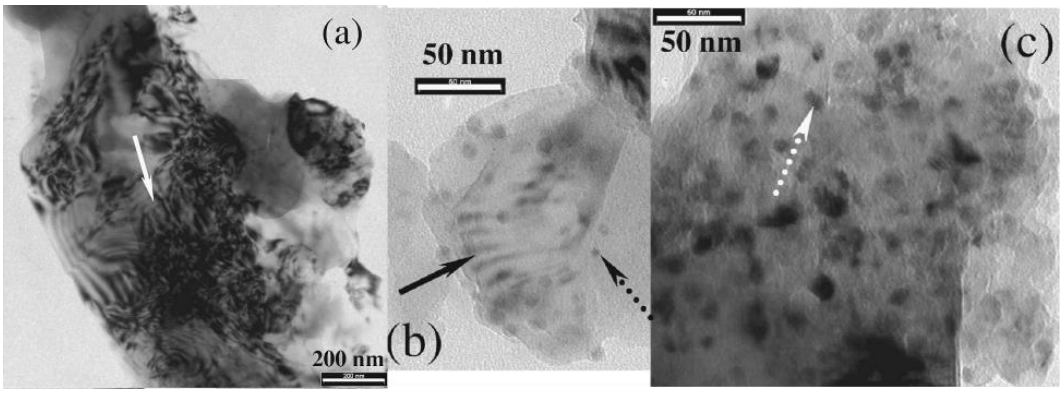

Figure 16 TEM images of SiC doped MgB_2 samples. High dislocation density and round shape inclusions are present within each grain [75]. (Reprinted with permission from AIP)

Much research has focused on carbohydrates as a source of C doping in MgB_2. Selected carbohydrates are inexpensive and can easily mix with B powder to form a B/organic slurry leading to a homogeneous distribution of C in the starting powder, after pyrolyzation at low temperatures (~300 °C) under vacuum. Many authors have observed strong enhancements of flux pinning and B_{c2} as a result of various carbohydrate additions. Kim *et al.* [89] used malic acid ($C_4H_6O_5$) to homogeneously mix C with initial B powder and obtained strong increases in J_c and flux pinning force density, F_p, in high fields. Gao *et al.* [90] in studies of maleic anhydride ($C_4H_2O_3$) and maleic acid ($C_4H_4O_4$) doped MgB_2 tapes found J_c values which were ten times higher than the undoped MgB_2 tapes. Bohnenstiehl *et al.* [91] investigated malic acid ($C_4H_6O_5$) doping in MgB_2 strands observing in them a clear increase of B_{c2}. Although the use of carbohydrates as a vector for C doping in MgB_2 has many advantages, it is inevitable that oxide impurities such as MgO and B_2O_3 can be introduced simultaneously. Referring to Section 1.4, these oxides are insulating materials which can significantly reduce connectivity. Carbohydrates

(depending on their chemical composition) contain a relatively high fraction of oxygen which might cause a serious issue. As seen in Gao's work [90], the J_c of the 10 wt.% $C_4H_2O_3$ doped MgB_2 tape was higher than that of the 10wt% $C_4H_4O_4$ doped tape as a result of the latter's greater O content.

Recently, a "C-pre-doped" boron powder was developed by Specialty Materials Inc. (SMI). This "C-pre-doped" B powder is produced in a plasma torch by the reaction of $BCl_4 + (2-2x)\cdot H_2 + x\cdot CH_4 \Rightarrow B + x\cdot C + 4HCl$. Nano-size B powder with homogeneously distributed C is formed during this reaction [92]. Using this pre-doped B powder, Susner *et al.* [93] obtained significant improvements of the high field J_c and B_{c2} in a series of MgB_2 wires with various C contents. This C pre-doping method leads to a more homogeneous distribution of C than the previously mentioned methods (e.g. SiC and carbohydrates).

Although C doping has been extensively studied, there are debates on the mechanism of the resulting B_{c2} enhancement. A widely accepted mechanism is the substitution of C into the B sites under which condition electron scattering in the σ bond is enhanced while π bond is relatively unaffected [94,176]. Based on the two-band theory and the equations (17) and (18), the B_{c2} in the low temperature regime can be increased by C doping, consistent with many experimental results [86-88]. However, Kim *et al.* [96] claimed the absence of C substitution into the MgB_2 lattice in a malic acid doped MgB_2 wire, Figure 17. By using a Cs-corrected scanning TEM (STEM) equipped with an electron energy loss spectrometer (EELS), he observed that most of the C was outside the MgB_2 grains in the form of thick C layers enclosing unreacted B powder particles, Figure 17 (a)

inset. Rather than C substitution, Kim explained the B_{c2} enhancement in his work as the contribution from MgB_2 lattice distortion caused by vacancies and stacking faults.

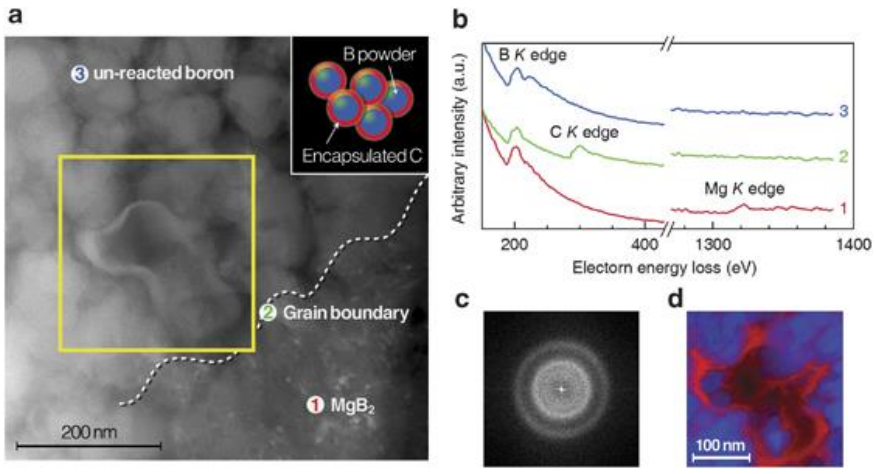

Figure 17 Microscopic analysis of the grain boundary region of malic acid-doped sample. (a) Scanning transmission electron microscope (STEM) image of interface region, with the inset showing a schematic diagram. (b) Electron energy loss spectrum (EELS). Carbon K peak can be most clearly seen at the interface (region 2). (c) Fast Fourier transform (FFT) pattern for the impurity phase. (d) Color map of electron energy loss of boron K (blue color) and carbon K (red color) in a selected area of (a) (marked with yellow box) [96]. (Reprinted with permission from Nature Publishing Group)

Susner *et al.* [97] investigated C doping in MgB_2 bulk samples synthesized by a high-temperature and high-pressure method (to be described in detail in chapter 2). Using an electron probe microanalyzer (EPMA) and a wavelength-dispersive spectrometer (WDS), Susner was able to perform direct compositional analysis on a very large MgB_2 grain (~ 20 μm), Figure 18. After collecting the C concentration in multiple spots inside the MgB_2 grains, he reported a homogeneous dissolution of C in MgB_2 grains at a concentration of ~ 6 at. % C, an observation supporting the substitution of C in MgB_2.

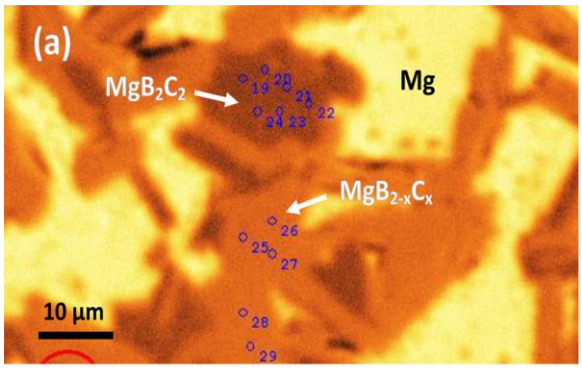

(b)

		$MgB_{2-x}C_x$	MgB_2C_2
Mg	As collected	37.0 ± 0.7	23.0 ± 1.1
	Re-normalized	36.5 ± 0.8	19.9 ± 1.2
B	As collected	55.0 ± 0.8	32.4 ± 3.5
	Re-normalized	57.3 ± 0.9	36.1 ± 3.9
C	As collected	5.9 ± 1.3	39.6 ± 3.8
	Re-normalized	6.2 ± 1.3	44.1 ± 4.2
O	As collected	2.0 ± 0.2	5.0 ± 1.7
	Re-normalized	--	--
(B+C)	As collected	61.0 ± 0.7	71.9 ± 1.8
	Re-normalized	63.5 ± 1.6	80.2 ± 5.7

Figure 18 (a) False color SEM image showing locations of EPMA data collection and (b) summary of EPMA analysis on sample MBC-2 including renormalization based on the assumption that most of the oxygen was bound to Mg as MgO [97]. (Reprinted with permission from APS)

There is no doubt that C doping is an effective way to increase the B_{c2} of MgB_2 superconductors. However, two significant "tradeoffs" simultaneously appear during C doping. Firstly, the T_c of MgB_2 is reduced, in some cases from 39 K to 23 K [97], making C doping ineffective at high temperatures (20 – 30 K). Thus for MgB_2 devices intended for operation at 20 K or above, C doping is less attractive. Secondly, the C doping-induced improvement in the B_{c2} is accompanied by a decrease in the J_c at low magnetic fields. This "cross-over effect" reported by Susner *et al.* [99] has been observed in many C-doped MgB_2 wires [96,100-102]. In summary, C doping decreases T_c, increases B_{c2} and high-field

J_c, and reduces the low-field J_c. The benefit of this cross-over effect has been discussed elsewhere [99].

1.5.2 Metal Doping in MgB_2

It is not surprising that metal and metal-containing compounds have been considered as dopants in MgB_2. Like C substitution for B and metals having similar chemical properties to Mg, are believed to have the possibility of substituting for Mg atoms. Metal-containing dopants, including pure metals and metal borides, have been extensively studied. Aluminum was considered by Slusky *et al.* [103] as a doping candidate soon after the superconductivity of MgB_2 was discovered in 2001. The following factors marked Al as a promising dopant: AlB_2 is isomorphic to MgB_2; the in-plane lattice parameter of AlB_2, a = 3.008Å, is similar to that of MgB_2 (MgB_2: a = 3.086Å), although its out-of-plane parameter c = 3.261Å is much smaller (MgB_2: c = 3.524Å). Therefore, successful Mg site substitution will produce a reduction in c rather than a. Also, Al has comparable melting point (660 °C) as well as high solubility in Mg [176]. Various studies, both experimental and theoretical, followed Slusky *et al.* [103] and provided many interesting results [104-109]. Generally speaking, Al can substitute for Mg atoms on the Mg site and form a $Mg_{1-x}Al_xB_2$ solid solution when $0 \le x \le 0.5$ without losing superconductivity [104,105]. This solid solution has an interesting lamellar superstructure of ordered Mg and Al layers along the c-axis, Figure 19 (a - c). The T_c as well as the out-

of-plane lattice parameter, *c*, is gradually decreased with increasing Al doping level. The in-plane lattice parameter, *a*, is relatively insensitive to Al content, as compared to *c*, Figure 20. There is a significant downside to this procedure: B_{c2} decreases with increasing Al doping concentration [105,106], Figure 21. Several studies on Al-doped MgB_2 single crystals show this result in more detail [107]. With increasing Al levels, B_{c2} parallel to the *c*-axis is relatively unchanged, while B_{c2} parallel to the *a-b* plane decreases. Therefore, in randomly oriented polycrystalline MgB_2, the overall B_{c2} decreases. Thus, because of their negative effects on T_c and B_{c2}, Al and Al-containing dopants are not considered as useful additions to MgB_2.

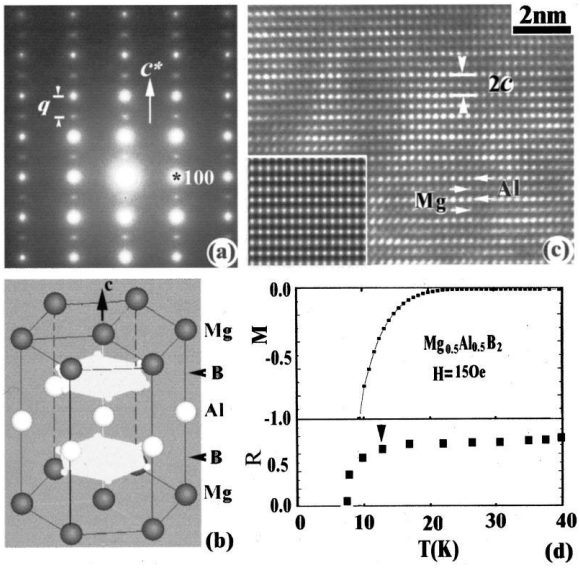

Figure 19 (a) An electron-diffraction pattern of the superstructure phase $MgAlB_4$, with the wave vector of $q=c^*/2$. (b) A schematic structural model of $MgAlB_4$. (c) High-resolution TEM image clearly exhibiting ordered Al and Mg layers along *c* direction. Inset shows a calculated image. (d) Temperature dependence of normalized magnetization (upper panel) and resistivity (lower panel) showing superconductivity in a $MgAlB_4$ sample [104]. (Reprinted with permission from APS)

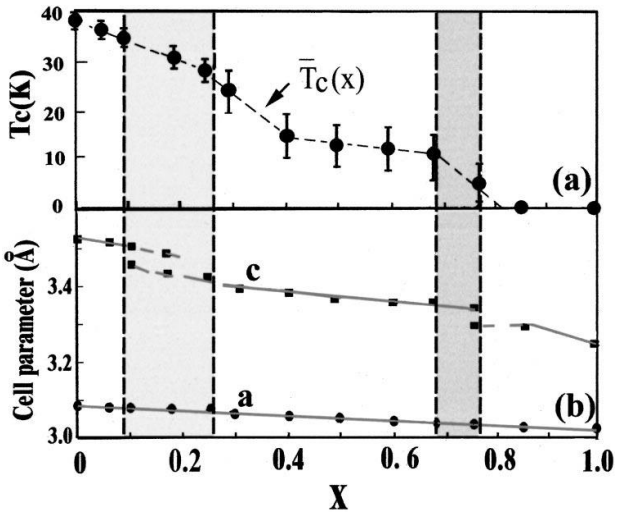

Figure 20 Composition dependence of (a) superconducting temperature (T_c) and (b) basic structural parameters *a* and *c* for $Mg_{1-x}Al_xB_2$, anomalies in both structural and physical properties in association with Al ordering can be clearly recognized [104]. (Reprinted with permission from APS)

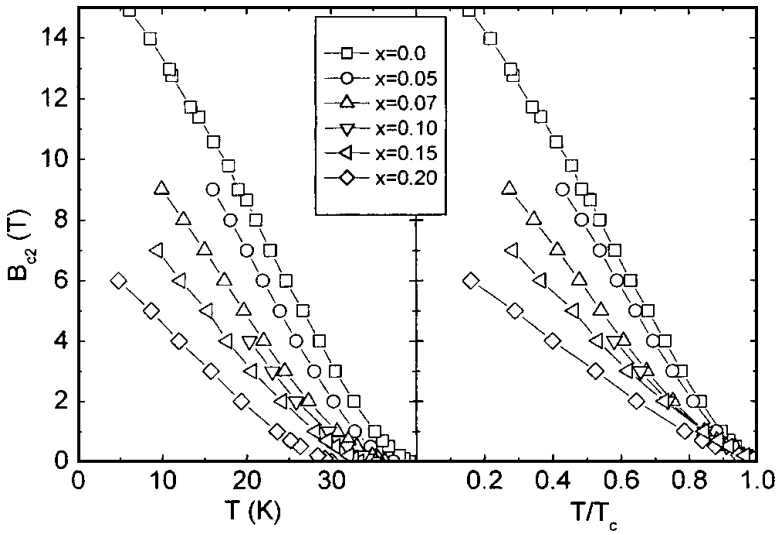

Figure 21 Left panel: B_{c2} of the $Al_xMg_{1-x}B_2$ samples as a function of temperature; right panel: B_{c2} of the $Al_xMg_{1-x}B_2$ samples as a function of the reduced temperature T/T_c [107]. (Reprinted with permission from APS)

Zirconium (Zr) has been considered as a candidate for substitution onto the Mg site. ZrB_2 also has AlB_2–type structure, however, unlike AlB_2, the in-plane lattice parameter of ZrB_2 (a = ~3.170Å) is larger than that in MgB_2 (~3.086Å), while their out-of-plane lattice parameters c (~3.533Å for ZrB_2 and ~3.524 for MgB_2, respectively) are similar [111]. Zr has a high melting temperature (~1855 °C), as well as low solubility in Mg even at high temperatures (less than 1mol% at 2000 °C) [112]. Recent studies on Zr/ZrB_2 doping are contradictory. Feng *et al.* [113,114] reported an enhancement in B_{c2} in response to 10 mol% Zr doping; Bhatia *et al.* [8,115] observed an increase in B_{c2} (from 20.5 T to 28.6 T at 4.2 K) after adding 7.5 mol% ZrB_2 in MgB_2 bulk samples. On the other hand, Zhang *et al.* [116] reported no changes in B_{c2} in the ZrB_2 doped MgB_2 tapes. In any case, while B_{c2} increases have been noted by various researchers working with MgB_2 PIT or powder type processes, no one has reported any increases in J_c, suggesting that the effect may be in a surface layer rather than the bulk. The one effort to date which has clearly injected Zr deeply into the grain (a pulsed laser deposition (PLD) synthesized ZrB_2-doped MgB_2 thin film [9,117]) showed a strong response to the presence of Zr, in this case decreases of T_c and B_{c2} with increasing Zr content. These various observations give rise to the question: what is the actual influence of Zr doping in MgB_2? The possible roles of Zr in MgB_2 can be summarized in terms of: (1) extrinsic effects, such as increased intergranular connectivity and reduced grain size [113,114]; (2) intrinsic effects, such as an influence on B_{c2} of the substitution of Zr for Mg atoms [8,9, 115, 117], and increased flux pinning by a distribution of nano-size ZrB_2/Zr precipitates [116]. Bearing in mind that the experimental conditions (sample types, purities and sizes of the raw materials, and also the heat treatment

schedules) were varied in these reports, Zr doping might perform different or multiple functions under different experimental conditions. On the other hand, incomplete microscopic evidence of Zr substitution for Mg has been provided, at least for materials made by equilibrium processes (contrasting to the non-equilibrium processing of the films of [9, 117]). Therefore, further study on the mechanisms and kinetics of Zr doping is deemed to be necessary.

1.5.3 Rare Earth Oxide Doping in MgB_2

Besides chemicals aiming at the substitution for Mg or B, numerous other dopants, with an aim of introducing pinning centers, have been studied as well. As mentioned in Section 1.4.3, defects with appropriate size can act as flux pinning centers. Nano-size impurity doping, therefore, has the potential to enhance the flux pinning behavior and J_c in the MgB_2 superconductors. Many studies have focused on the effects of nano-size dopants in MgB_2. Metal nano-powders have not improved the properties of MgB_2. On the other hand, several recent studies have shown that nano-size rare earth oxides (REO), such as Y_2O_3[118], Dy_2O_3 [119], Nd_2O_3 [120], Ho_2O_3 [121], Pr_6O_{11} andEu_2O_3 [122], can improve the superconducting properties of MgB_2 by forming pinning centers inside MgB_2 grains. The first report in REO doping was that of Wang *et al.* [118] who studied Y_2O_3 nano-powder (10-30nm) doping in MgB_2 bulk samples. Wang observed that YB_4 precipitates (3-5nm in size) were evenly distributed within the MgB_2 grains and some larger YB_4

precipitates (~10nm) appeared at the grain boundaries in Figure 22. He did not observe any changes in the lattice parameters and T_c even after adding 10wt% Y_2O_3, which suggests that these YB_4 nanoparticles neither alloyed with the MgB_2, nor produced significant disorder. After subtracting the influence of sample porosity, it was seen that the J_c in the doped samples was slightly increased in all measured fields, especially in the 10wt% Y_2O_3 added sample. Also he reported a large increase in the B_k in response to Y_2O_3 doping. Wang's observation is important not only because the J_c of MgB_2 was improved, but his work showed that dopants which do not substitute for Mg or B can still benefit the properties of MgB_2.

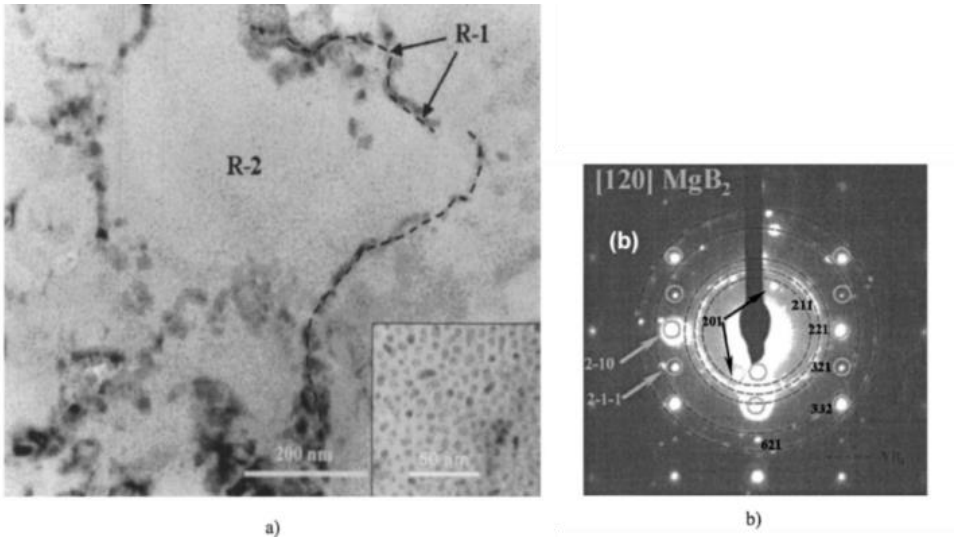

Figure 22 TEM of 10 wt % Y2O3-doped MgB_2 (a) Micrograph showing nanoprecipitates of YB_4 embedded in MgB_2 grains, and (b) diffraction pattern along MgB_2 [120] direction. YB4 ring pattern is outlined [118]. (Reprinted with permission from APS)

Cheng *et al.* [121] studied Ho_2O_3 nano-powder (~ 50 nm) doping in MgB_2. Similar to the effects of Y_2O_3 doping, the lattice parameters and T_c of MgB_2 did not change up to

3 at. % Ho_2O_3 additions. Also, nanoparticles of HoB_4 with a size of 5–10 nm were dispersed in the MgB_2 grains. Cheng noticed that there was no difference in the B_{c2} between undoped and Ho_2O_3-doped MgB_2 samples. However, unlike Y_2O_3 doping which increased J_c at all magnetic fields [118], doping with Ho_2O_3 increased only the high-field J_c, leaving the low-field J_c relatively unchanged. Later, the effect of Dy_2O_3 doping in MgB_2 was reported by Chen *et al.* [119]. As with Y_2O_3 and Ho_2O_3 doping, he observed no changes in the T_c, lattice parameters, and B_{c2} after adding 0.5 wt.% Dy_2O_3 powders. He also noticed that nano-size DyB_4 precipitates existed in MgB_2 grains and at the grain boundaries in Figure 23 (c) (d). By adding 0.5wt% Dy_2O_3, the average grain size reduced from ~500nm to ~200nm (Figure 23 (a) (b)), compared to Ho_2O_3 doping which did not change the grain size [121]. The J_c of the Dy_2O_3 doped samples increased in all magnetic fields, more so in low fields.

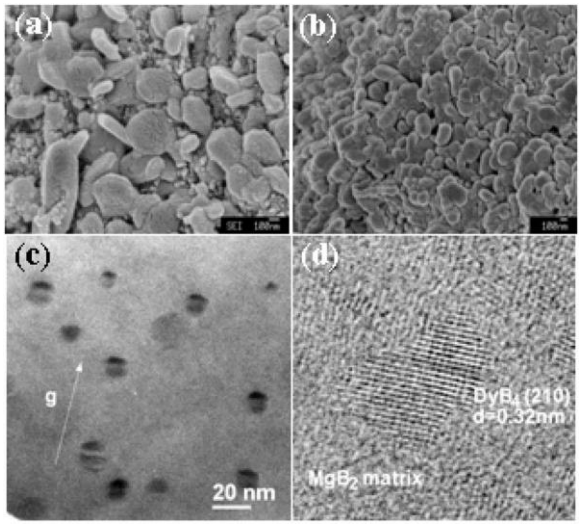

Figure 23 FEG-SEM images of the (a) pure MgB_2 and (b) sample added with 0.5 wt.% of Dy_2O_3. (c) Bright-field TEM micrograph of MgB_2 matrix showing strain field contrast with a high order matrix reflection. The reciprocal lattice vector g is indicated by an arrow. (d) HRTEM image showing the [210] lattice fringe of a nano-size DyB_4 precipitate [119]. (Reprinted with permission from APS)

Generally speaking, REO do not substitute for the Mg or B atoms or generate distortion sufficient to change the lattice constants, T_c, and B_{c2}. Instead they can react with Mg and B to form rare earth borides (REB_4) as nano-size precipitates embedded inside MgB_2 grains or at the grain boundaries. They are formed by the reaction: $x \cdot RE_2O_3 + Mg + 2B \Rightarrow 2x \cdot REB_4 + (1-4x)MgB_2 + 3x \cdot MgO + x \cdot Mg$.

These nano-size precipitates of REB_4 act as pinning centers and improve flux pinning, and thereby increase J_c. Although these REO dopants have positive influences on MgB_2, several important issues still need to be addressed and resolved. (1) The J_c has different in-field behaviors in response to different dopants, e.g., Y_2O_3-doping slightly increased J_c at all fields [118]; Ho_2O_3-doping only increased high-field J_c [121]; Dy_2O_3-doping increased J_c at all fields, but more so at low fields [119]. Lack of theories to explain these observed experimental variations can be problematic for further studies. (2) Although REO doping has been stated to be relatively homogeneous, it is hard to believe that homogeneous doping was achieved in these samples. All the heat treatments were performed around or below 900 °C a temperature range in which the diffusivities of these rare earth species in MgB_2 are very low.

1.6 Summary and Motivation

MgB_2 has many advantages: (i) its T_c of ~39 K, the highest of the conventional superconductors indicates a potential for liquid-helium-free applications (20 - 30 K); (ii) its lack of weak links makes MgB_2 superconductors easy and inexpensive to fabricate on a large scale without having to consider grain alignment; (iii) the depairing critical current density J_d is comparable to those of other superconducting materials; and (iv) the low cost of its precursor materials and its simple binary composition. However, there are still several obstacles limiting the wide application of MgB_2. Three approaches address these issues: (1) Enhancement of B_{c2} to improve the high field performance of MgB_2 by C-containing dopants. (2) Introduction of new flux pinning centers to increase the bulk pinning force density, F_p, and the intrinsic J_c by, for example, neutron irradiation and grain refinement. (3) Improvement of the intergrain connectivity by techniques such as cold/hot pressing and internal magnesium diffusion.

Chemical doping is regarded as one of the most effective approaches. Selected dopant species can alloy with MgB_2 to increase B_{c2} and/or induce defects and precipitates to increase flux pinning. However, chemical doping can also induce impurities which can reduce the connectivity and hence the J_c. Therefore, the balance between the benefit of enhanced B_{c2} and flux pinning and the trade-off of reduced connectivity is important when considering the doping of MgB_2.

Motivation:

The purpose of this thesis work is to obtain an understanding of the chemical doping introduced changes in the microstructures and superconducting properties in MgB_2 superconductors. Specifically, I focus on three types of chemical doping:

(i) Study C doping and its influence on state-of-art *in situ* MgB_2 wires in terms of superconducting properties (J_c and *n*-values). As described in Section1.5.1, C doping has been proved to be effective at low temperatures ($T < 20$ K) in MgB_2 bulk and thin films, so my motivation is to try to apply C doping in the MgB_2 wires and improve the in-field performance of these MgB_2 wires by controlling C concentration, HT parameters and other parameters (e.g. wire structure, B types, C dopant types);

(ii) Investigate the influences of REO doping on the microstructure and superconducting properties of MgB_2. REO doping can improve the J_c of MgB_2 bulk (Section 1.5.3), however the mechanism behind this improvement is still unclear. Also few studies have reported that REO doping improves the J_c of MgB_2 wires. My motivation is to reveal REO doping effect on microstructure and superconducting properties of MgB_2 bulk, build the connection between them and use these findings to improve the state-of-the-art MgB_2 *in situ* wires;

(iii) Explore the possibilities of Mg site substitution by MB_2 doping. Based on the theoretical work by Gurevich *et al.* [42,44] (described in Section 1.4.2), successful Mg site substitution, if it was possible, may enhance B_{c2} of MgB_2 at high temperatures (close to T_c), unlike B site substitution which can only increase B_{c2} at low temperatures (close to 0 K). Extensive efforts have been made on MB_2 doping in MgB_2. Some of researchers

observed increases in B_{c2}, but few of them reported increases in J_c. To understand the mechanism behind these observations, a series of MB_2 isomorphic to MgB_2 are selected as potential dopants and a high temperature and pressure equipment (HPT) is used to fabricate dense and homogeneously doped MgB_2 bulk at well-controlled experimental conditions. The doping introduced changes in the microstructures (e.g. crystal defects and impurity inclusions) and superconducting properties (e.g., T_c, B_{c2}, and flux pinning) of metal-diboride- and Dy_2O_3-doped MgB_2 are studied.

Chapter 2: Experimental Methods and Sample Fabrication

The various methods for making MgB_2 bulk and wires will be described. Among them, a high-pressure and temperature-method (HPT) has been developed for the synthesis of MgB_2 bulk samples. The experimental techniques used for sample characterization include X-ray diffraction (XRD), scanning electron microscopy (SEM), transmission electron microscopy (TEM), transport measurements, magnetic measurements (vibrating sample magnetometry (VSM)) and resistivity are also described.

2.1 MgB_2 Bulk Synthesis Techniques

The conventional method for fabricating MgB_2 bulk samples is powder synthesis. In terms of powder types and reaction mechanisms, powder synthesis can be divided into two different categories: (i) the *ex situ* method, where MgB_2 powder is ground, packed into a sample container and sintered at temperatures above 900 ºC; and (ii) the *in situ* method in which the Mg and B powders are mixed, packed and reacted at 600-800 ºC to form MgB_2. Both methods need to be performed in an inert environment (typically Ar) to prevent the formation of oxides (MgO and B_2O_3). The advantage of the *ex situ* method is that the

packing density of MgB_2 powders in the sample container does not suffer from reaction-induced porosity. The disadvantage is that the oxides may cover the MgB_2 particles making them difficult to sinter together [123]. Dancer *et al.* [123] found little evidence for self-sintering in the *ex situ* MgB_2 bulk samples heat treated at 1100 ºC. As a result, the intergranular connectivity in the *ex situ* MgB_2 bulk samples is generally poor. As the sintering temperatures are high, MgB_2 grain coarsening is inevitable. Since MgB_2 is mainly a grain boundary pinning material, the larger grain size leads to a weaker flux pinning. Compared to the *ex situ* method, the main advantage of the *in situ* method is that the MgB_2 grains formed by the reaction between Mg and B are well connected. Further, chemical doping can be easily incorporated since the dopants can participate in the formation of MgB_2 phase. The size of MgB_2 grains in the *in situ* bulk is generally small as a result of low heat treatment temperatures. However, as mentioned in Section 1.4.5, the major drawback of this method is the unavoidably high porosity caused by the reaction between Mg and B.

An alternative *in situ* method, first introduced by Giunchi [124] in 2003, is named "reactive liquid Mg infiltration (Mg-RLI)". In this method, the B powder is packed in a container and Mg source (typically in the forms of large Mg pieces) is imbedded in the B compact. The container is then evacuated, sealed and heat treated to temperatures of typically 900 °C for a few hours. During the heat treatment, the Mg melts, infiltrates into the B compact and reacts with B to form a dense MgB_2 bulk. This Mg-RLI method is very useful since it results in MgB_2 bulk without the low intergranular connectivity and porosity characteristic of the *ex situ* and the conventional *in situ* methods. However, under Mg-RLI

it is difficult to obtain fully-reacted MgB_2 bulk, as the contact surface between Mg and B is small and the process is diffusion-control, as a result of which the formed MgB_2 bulk are unlikely to be homogeneous.

In this work some MgB_2 bulk samples were made by the conventional *in situ* methods. In addition, an *in situ* high-pressure and high-temperature method (HPT) was used to make dense and homogenous MgB_2 bulk.

2.2 MgB_2 Superconducting Wire Fabrication

For most practical application, MgB_2 superconductors are fabricated into long wires. So far three methods have been used to make MgB_2 wires: (i) the *ex situ* method; (ii) the *in situ* powder-in-tube method (PIT); (iii) the internal Mg diffusion method (IMD) [130].

In an *ex situ* process, commercial MgB_2 powder is cleaned, milled and loaded into a metal tube. After that, the composite is drawn to wire. This as-drawn wire has moderate superconducting performance. Usually it needs to be heat treated over 900 ºC for several hours to enable the individual MgB_2 grains to sinter together, form good bonds, and achieve high electrical connectivity [11]. As with the *ex situ* bulk, the main advantage of this *ex situ* MgB_2 wire method is its high packing density, although the overall connectivity is generally limited by poor intergranular connectivity.

In the fabrication of *in situ* PIT MgB_2 wires a mixture of Mg and B powder is loaded into a metal tube. After drawing, the wire is heat treated (typically at 600-800 ºC) and MgB_2 is formed by the reaction: $Mg + B \Rightarrow MgB_2$. Although the MgB_2 grains are well connected, high porosity is unavoidable (Figure 12).

The IMD method is different from either the *ex situ* route or the *in situ* PIT route. A Mg rod is placed along the axis of a B powder filled metal tube. The composite is then drawn to wire and heat treated at 600-800 ºC. As with the Mg-RLI method, during heat treatment the Mg rod melts, infiltrates into the surrounding B layer and reacts with it. Thus, after the reaction a MgB_2 layer is formed surrounding a cylindrical hole along the axis of the wire. Since this is also an *in situ* method, the porosity from the MgB_2 formation cannot be avoided. However, by using this method, all pores are concentrated at the center hole so that the formed MgB_2 layer is dense and well connected along the longitudinal axis. Therefore, the transport performance viz. J_c of the IMD wires is generally better than the *in situ* PIT wires with the same overall porosity. Figure 24 shows a reacted IMD monofilamentary MgB_2 wire with a dense MgB_2 reaction layer and the central hole.

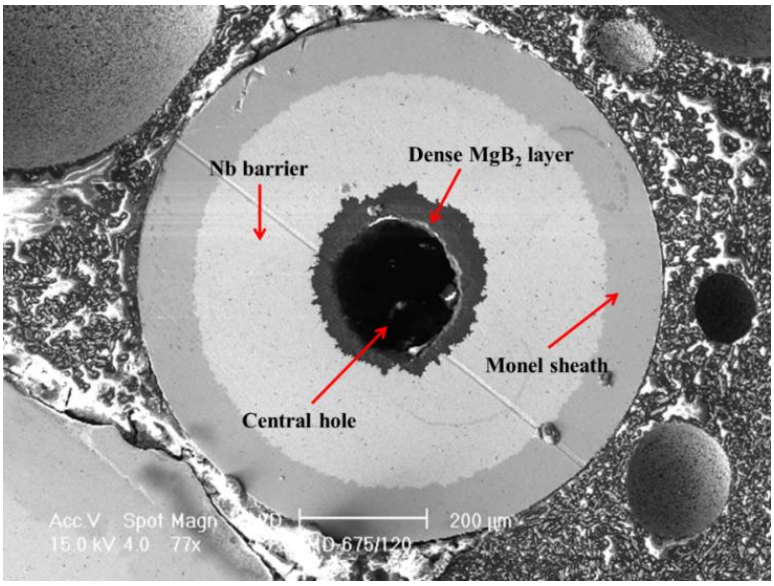

Figure 24 A reacted IMD monofilamentary MgB_2 wire shows dense MgB_2 layer surrounding a large central hole where the Mg rod was present before the reaction [125].

A "continuous tube filling and forming" process (CTFF) has been developed by our collaborator Hyper Tech Research, Inc, for the large scale manufacture of long-length MgB_2 wire [176]. In this process, the mixtures of Mg and B powders are continuously dispensed onto a strip of a metal (e.g. Nb and Fe) which is overlap-closed to form a precursor-filled tube. Then the tube is either inserted into an outer sheath material with a good workability (typically Monel) in preparation for drawing down to a monofilamentary wire, or bundled with other precursor-filled tubes to make a multifilamentary wire. The CTFF process not only reduces cost by the use of inexpensive metal strips instead of expensive metal tubes but increases the efficiency of MgB_2 superconducting wire manufacture.

All MgB_2 PIT wires mentioned in this work are fabricated by the CTFF process. For convenience, they will be referred to as PIT wires.

2.3 High-Pressure and High-Temperature Method

As mentioned in Section 1.5, chemical doping is critical to the improvement of the superconducting properties of MgB_2. However, there are many roadblocks to clarifying the true role of chemical doping in MgB_2: Homogeneous doping is hard to achieve. Traditional powder synthesis is generally performed at 600 - 1000 °C -- too low to form homogeneous samples. Moreover, the solubility of doping species within the MgB_2 grains controls the actual doping amount after heat treatment, which limits the doping efficiency, especially at low HT temperatures (<1000 °C). The grain size in PIT is small (~ 30 – 100 nm). Although such small grains are needed for optimization of flux pinning and high J_c in wires, it is difficult to perform microstructural and compositional analysis on them. The above difficulties obscure the outcome of chemical doping studies.

To overcome these problems, the high pressure and temperature (HPT) equipment developed by Bohnenstiehl [98] was used to synthesize MgB_2 bulk samples at very high temperatures (≥ 1500°C). Based on the Arrhenius equation $D = D_0 e^{-E_A/(kT)}$, the HPT process strongly enhanced diffusion during the sample synthesis. MgB_2 bulk synthesized by HPT have minimal porosity, large grain size (over 5 μm), and presumably better homogeneity due to fast diffusion at high temperatures. Figure 25 illustrate the HPT process and its use to fabricate MgB_2 bulk (see also [98,127]): (i) B powder (hand mixed with the dopant powder if the aim is to make a doped MgB_2 sample) is high energy ball milled for 15 min in an Ar atmosphere; (ii) the B powder is then pressed into ~8 mm tall by ~ 13 mm diameter pellets and placed in an MgO crucible; (iii) Mg turnings are placed

on the top of the B pellets (the Mg:B ratio in the crucible was about 1:1 to avoid possible Mg deficiencies during heat treatment); (iv) the crucible is then capped and placed inside the sample assembly, Figure 25 (e); (v) the whole assembly is placed in the HPT's pressure vessel, Figure 25 (f).

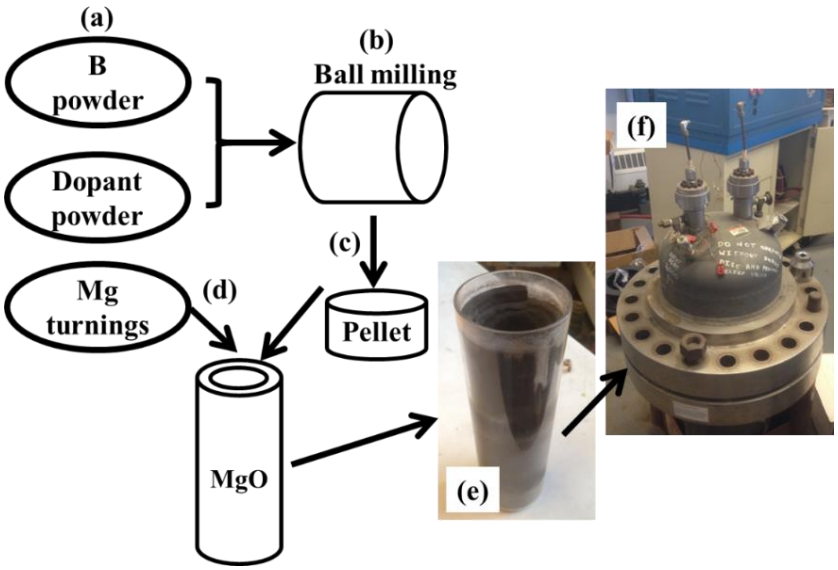

Figure 25 The schematic diagram of the HTP process involved (a) hand mixing; (b) ball milling; (c) pressing into pellets; (d) filling Mg turnings; (e) assembling; and (f) induction heating.

The HPT rig includes a high pressure vessel with a built-in induction coil, an induction power supply (Lepel T-5-3 induction heating power supply, 5 kW at 450 kHz), temperature controller (Eurotherm 3504 with 0-10 V signal), a water cooling system (Haskris water chiller), a vacuum pump and high purity Ar gas cylinders connected to the pressure vessel. Most of the components are shown in Figure 26.

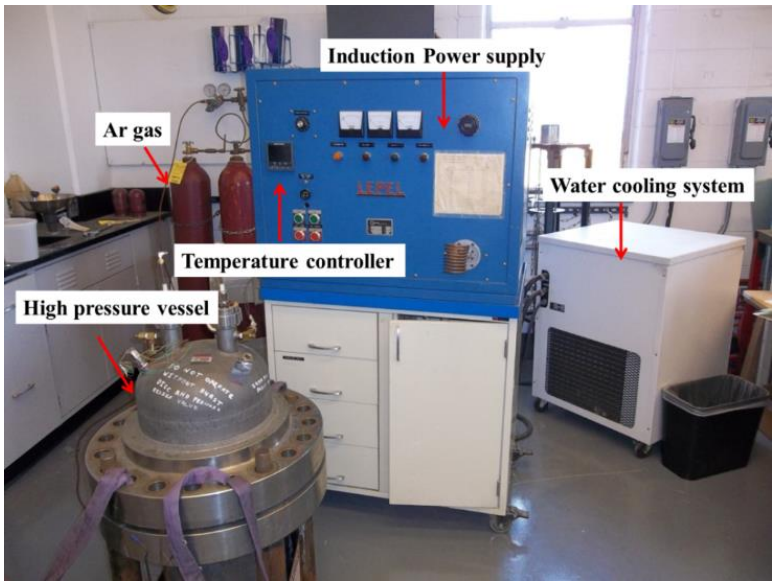

Figure 26 A picture of the HPT rig with important components labeled.

The pressure vessel consists of two hemispherical halves bolted together. The maximum pressure capacity of this vessel is 2000 psi (13.79 MPa). For safety reason, a rupture disc is mounted on a port of the vessel in combination with a 10 MPa safety relief valve. High purity Ar gas is used to provide the gas pressure and maintain an inert environment. An induction coil which is installed inside the pressure vessel works as an induction heater. Induction heating is the process of heating an electrically conducting material (a susceptor) by inducing a high-frequency AC current in it. An electronic oscillator is used to produce the high-frequency AC current which generates a rapidly alternating magnetic field. This magnetic field penetrates the material and generates eddy currents that flow through the material and generate resistive loss to heat the material. The sample is induction heated via a susceptor surrounding the sample through heat conduction.

The frequency of current used depends on the sample size, material type and coupling between the work coil and the materials to be heated.

A Lepel T-5-3 induction heating power supply with a maximum power output of 5 kW at 450 kHz is used here. The Eurotherm 3504 controller has multiple thermocouple inputs and a high resolution output with a 0-10 V signal to control the Lepel power supply. The induction coil is a water-cooled copper tube with a 6.3 mm OD and 5.1 mm ID. A Haskris water cooling system is connected to the Lepel power supply.

The sample assembly displayed in Figure 25 (e) contains three components: (i) a susceptor assembly, which includes a graphite susceptor surrounded by graphite felt; (ii) a crucible with a ceramic lid as the sample container; (iii) a closed-bottom fused quartz tube which is used to hold the susceptor assembly. The graphite susceptor contains the sample crucible. Graphite felt is used to prevent heat loss by convection and conduction. Two type C thermocouples are inserted into the sample assembly (one is in the sample crucible and the other contacts with the graphite susceptor) to accurately measure the temperature during the heat treatment. The whole sample assembly is carefully placed in the center of the induction coil.

Several materials, e.g. alumina, silica and metals have been considered as possible sample containers. Since the temperature can be as high as 1700 °C and Mg is very reactive at high temperatures, magnesia (MgO) crucibles were used as MgO does not react with the Mg/B samples even at 1700 °C. The MgO crucibles with 2.5 cm OD and 1.3 cm ID (from Ozark Technical Ceramics) were used in this work. In order to further reduce the oxygen

contamination, Ta foil with a 0.3mm thickness covering the MgO crucible provided oxygen gettering.

The type C thermocouples used in this work were custom made by using type C thermocouple wires (W-5%Re / W-26%Re) 0.13 mm in diameter (from Concept Alloys, Inc.), high purity alumina 2-hole insulators (from Omega Engineering, Inc.) and Ta tubes to protect the wire from reacting with Mg, B and C. A TIG welding machine was used to weld the wires and the Ta tube together. During the measurement, an ice bath cools is used as the thermocouple cold junctions to ensure the output is stable and accurate. The thermocouple wire is certified to be within 1% of the standard tables for thermoelectric output via NIST-traceable standards.

2.4 X-Ray Diffraction

X-ray diffraction (XRD) was used for determination of crystal structure lattice constants and chemical phases. In XRD a coherent X-ray beam (most often Cu K_α wavelength λ = 1.5408 Å) strikes a material, and it is scattered by atoms into many specific directions. These directions are controlled by Bragg's Law $n\lambda = 2d\sin\theta$ for coherent scattering, where λ is the wavelength of the incident radiation, n is an integer, d is the inter-planar spacing of a crystal, and θ is the angle of diffraction. As shown in Figure 27 coherent scattering occurs when the path length $2d\sin\theta$ is an integer of the incoming wavelength $n\lambda$.

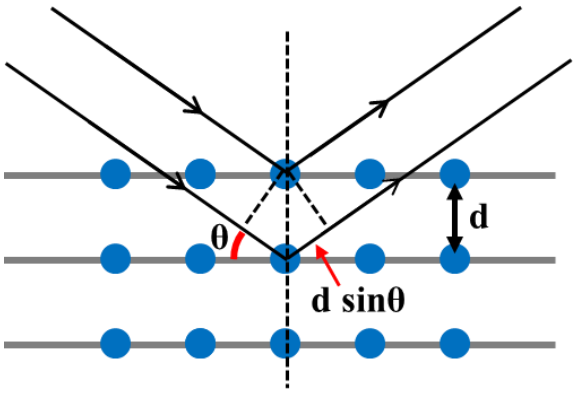

Figure 27 A schematic diagram of the Bragg's law condition where the incident beam and diffracted beam follow $n\lambda = 2d\sin\theta$.

XRD has been widely used to determine the changes in lattice parameters of MgB_2 samples with accuracies of 0.001Å [8, 9, 13, 15, 16, 43, 46, 48, 62, 81-86, 93, 98, 105, 106, 108, 109]. The XRD data of this research was performed on a Rigaku MiniFlex 600. This system utilizes a Cu K_α X-ray tube (λ = 1.5406 Å) operating at 40 kV and 15 mA and uses a vertical goniometer with Bragg-Brentano configuration to achieve the centering and parallelism of the beam without adjustment of the system. This goniometer is able to maintain the 2θ accuracy of 0.02°. Since the experimental errors are $\Delta d=\lambda/2\sin\theta-\lambda/2\sin(\theta+\Delta\theta)$ assuming low noise [206], this system can perform lattice parameters measurements with accuracies of 0.001 Å at 40° and 0.0005 Å at 60°, respectively. Alignment of the instrument was checked with a NIST traceable LaB_6 powder standard. The compositional resolution of this system is ~ 0.1 wt.% (provided by the manufacturer). The PDXL software with ICDD Powder Diffraction File (PDF2) data base and Rietveld refinement function was used for phase identification and the comparison of sample lattice parameters with literature values.

2.5 Electron Microscopy

Scanning electron microscopy (SEM), transmission electron microscopy (TEM) and scanning transmission electron microscopy (STEM) were used for microstructure characterization. These facilities are located at the Center for Electron Microscopy and Analysis (CEMAS) in The Ohio State University.

SEM produces images of the surface of a material inside a high vacuum chamber by scanning it with a focused beam of electrons in a raster pattern. When the electron beam interacts with the specimen, both backscattered electrons (BSE) and secondary electrons (SE) are generated and collected by different detectors for imaging. The SE imaging collects the electrons excited from the *K* shell of the specimen atoms and it commonly uses for surface imaging since most of the secondary electrons are produced within a 5 – 50 nm thick surface layer of the specimen. The BSE imaging uses the beam electrons which are reflected back from the specimen by the elastic scattering. The intensity of the BSE signal is strongly related to the local atomic number (Z) because the material with a higher atomic number is more likely to reflect the beam electrons. Therefore, BSE can be used to image compositional differences in the sample, via. *Z*-contrast.

In this research, both SE and BSE imaging were performed on either a Philips (FEI) Sirion field emission source SEM or a Philips (FEI) ESEM field emission SEM. The accelerating voltages of 10-25 kV were used depending on samples and applications.

TEM produces images through the interaction of an electron beam transmitted through a very thin specimen. This interaction can provide useful information about the microstructure, crystal structure and chemical composition. The accelerating voltages in TEM are generally over 100 kV, much higher than those in SEM. Such high accelerating voltage can produce a strong electron beam able to transmit through a very thin specimen and form a magnified image. TEM is capable of imaging at a much higher resolution than SEM, an advantages that comes at the expense of increased difficulty in sample preparation. Additionally, due to the nature of TEM which is only imaging a very small region of a sample, it is difficult to apply statistics in TEM imaging.

In this work, a FEI CM 12 with a W electron source was used for low resolution imaging; a FEI CM 200 with a LaB_6 electron source was used for high resolution imaging; and a FEI Technai with a field emission source was used for scanning transmission electron microscopy (STEM). In STEM the electron beam converges into a narrow spot (< 1 nm) and is scanned across the specimen in a raster pattern for detailed compositional analysis of small areas (~ 5 nm) and high angle annular dark field imaging (HAADF).

TEM Samples were prepared by ion-milling techniques using an FEI Helios 600 dual-beam focused ion beam (FIB). A Pt strip is deposited across a ~20 μm length of the specimen surface. A focused Ga^+ ion beam is then used to mill the specimen surface such that only a narrow wall of the material protected by the Pt remains. The TEM film is extracted with the Omniprobe micro-tool and secured to a special Cu grid with more Pt. Finally, the sample is thinned with a grazing incident Ga^+ ion beam at lower energies (5

keV) and angles (± 1.5°) to prevent Ga redeposition on the specimen surface and MgB_2 amorphization by the Ga^+ ion.

Energy-dispersive X-ray spectroscopy (EDS) is a powerful analytical technique which can be used to detect the composition of a specimen. When the electron beam excites an inner shell electron from the specimen, a hole is formed; an outer shell electron with higher energy then fills the hole and releases X-rays with a wavelength of the energy difference between these shells ($\Delta E=hc/\lambda$). These characteristic X-rays can be used to determine the composition of elements in the specimen. The number and energy of the X-rays emitted from a specimen can be measured by an energy-dispersive spectrometer. While EDS can be used to quantitatively detect heavy elements such as Mg, Zr, Ti, Nb, and Dy (with errors ~ 1 at. % based on the equipment specifications and [207]), it is not particularly useful for light elements (e.g., B and C) due to the low fluorescence yield (less X-ray generated) and the low value of the *K*-absorption energy (easily cutoff by windows of the detectors). Fortunately, with Si drift detectors (SDD), the characteristic X-rays of B and C can be effectively collected with reasonable accuracy. Most of the SEM and TEM instruments used in this work have EDS components for composition analysis. Moreover, the FEI CM 12 and FEI Technai are equipped with SSD. The interaction volume of EDS analysis is controlled by electron beam size, electron energy, sample thickness and sample composition. By using Monte Carlo simulation (Casino 3.2), I determined the EDS interaction volumes were ~ 1 μm^3 in the Sirion SEM at 15 keV, ~10^{-4} μm^3 in the CM-12 at 120 keV, and ~10^{-7} μm^3 in the Technai at 200 keV, respectively. Therefore, EDS in TEM

and STEM has much higher spatial resolution than that of SEM, which makes it possible to perform in-grain composition analysis.

2.6 Transport J_c Measurements

The transport J_c measurements in this work were performed in a 15 T Oxford Instrument research magnet in pool-boiling liquid helium (Figure 28). The four-point method was used to determine the voltage-current (*V-I*) transition of the MgB_2 superconducting wires in various temperatures and magnetic fields. A HP 6671 current power supply was used to provide a DC current up to 220 A, while three HP 6681 current sources connected in parallel were used when the required current was above 220 A. A Keithley 182 nanovoltmeter was used to accurately measure the voltage across the separation of the voltage taps, viz. the voltage gauge length. Generally, wire samples were tested in transverse magnetic fields ranging from 0 T to 15 T at 4.2 K. For the "short samples" (see below), *V-I* curves were obtained at temperatures of 4.2 to 35 K. This whole system was controlled by a LabVIEW interface.

Two types of MgB_2 samples were measured in this research: (i) "ITER barrel" samples consisted of 1.5 m-long length of wire helically wound onto 32-mm-diameter Ti-Al-V alloy holders. The voltage gauge length was 500 mm; (ii) "Short samples" were straight wires with 50 mm long for the 4.2 K measurements and 35 mm long for the variable-temperature measurements. The voltage gauge length was 5 mm.

Three sample probes were used to measure the transport J_c of MgB_2 samples, Figure 28: (i) A short sample probe was designed to test the short samples at 4.2 K with the current ranged from 0 to 220 A, Figure 28 (a). (ii) A variable-temperature probe was designed for short sample measurements at 10 - 35 K, Figure 28 (b). (iii) An ITER barrel probe was designed for testing the ITER barrels at 4.2 K with currents up to 1740 A, Figure 28 (c). For the variable-temperature probe, a custom sample chamber was made. It consisted of a brass can 150 mm long and 52 mm in diameter. The sample chamber was evacuated and sealed with Lipowitz's alloy (viz. Wood's metal), a eutectic, fusible alloy of 50 wt.% bismuth, 26.7 wt.% lead, 13.3 wt.% tin, and 10 wt.% cadmium. Inside the chamber, the sample was soldered between two Cu leads (square cuboid, $1.1 \times 1.1 \times 9.8$ cm^3) separated by a G-10 block. A 50 Ω Kapton heater was placed across two Cu leads and a Cernox temperature sensor was mounted onto one of the Cu leads close to the sample location. Temperature control was accomplished through a Lakeshore Model 330 temperature controller and thermal equilibrium was established between cooling along the current leads and resistive heating.

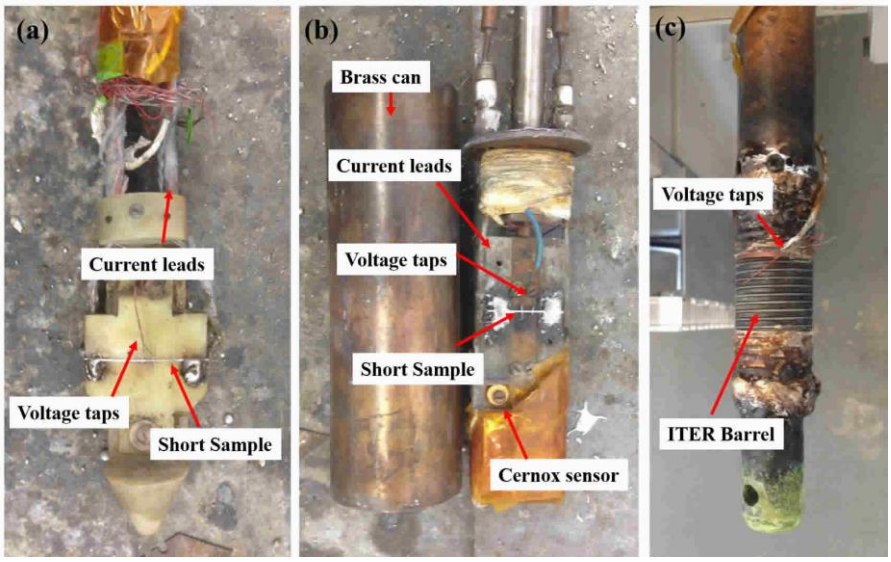

Figure 28 Three sample probes used in the transport measurements: (a) 4.2 K Short sample probe; (b) Variable temperature short sampe probe (10 - 35 K); (c) 4.2 K ITER barrel probe.

The transport critical current I_c was determined by evaluating the *V-I* transitions with an electric field criterion E_c of 1 μV/cm. The transport J_c was given by I_c / A_{sc}, where A_{sc} is the cross-sectional area of MgB_2 core in the wire. In the literature this transport J_c is also called the non-barrier J_c, in contrast to the engineering critical current density J_e given by I_c/A in which A is the whole cross-sectional area of the whole). Another important result deriving from the transport measurements is the *n*-value defined by:

$$\frac{E}{E_c} = (\frac{J}{J_c})^n \tag{28}$$

in which *E* and *J* are the electric field and current density, respectively. The *n*-value characterizes both transport performance and sustainability for industrial applications, as it represents the sharpness of the superconducting transition. Defects in practical wires

(e.g., wire sausaging, inhomogeneity and filament cracks) can cause reductions of the *n*-value, which can be used as an indicator of the quality of a practical superconductor.

2.7 Physical Property Measurement System

A Quantum Design Model 6000 Physical Property Measurement System (PPMS) was used for measuring numerous properties of the MgB_2 specimens. The PPMS has multiple options including DC resistivity, vibrating sample magnetometry (VSM), AC magnetic susceptibility (ACMS), heat capacity and thermal transport over a temperature range of 1.8 K to 400 K and in magnetic fields up to 14 T.

2.7.1 Vibrating Sample Magnetometry

The VSM option of the PPMS was used to determine the magnetization, *M*, of the samples. In VSM the oscillating field associated with the moment induced by a static magnetic field in an oscillating sample will induce an oscillating voltage in a set of pickup coils. Suitably calibrated this voltage leads to the sample's moment and hence to its magnetization (moment/volume). The measurement ranges of the VSM are $1.8 < T < 400$ K and $-14\ \text{T} < B < 14\ \text{T}$. The resolution is 1×10^{-6} emu at data rate of 1 Hz.

The magnetization from the VSM can provide very important superconducting properties, e.g. the T_c, J_c, B_{c2} and B_k. After measuring *M* at various temperatures and fields,

both the *M*–*B* curves at a particular *T* or the *M*–*T* curves at a particular *B* can be recorded and analyzed. Figure 29 shows a typical *M*-*B* curve of a MgB_2 specimen at 15 K measured by the VSM. The "magnetic critical current density", J_{cm}, can be calculated from the *M*-*B* curve by using the Bean critical state model:

$$J_{cm} \propto A \cdot \Delta M \tag{29}$$

where ΔM is the width of the *M*-*B* loop at a given *B*, Figure 29, and A is a geometrically dependent factor.

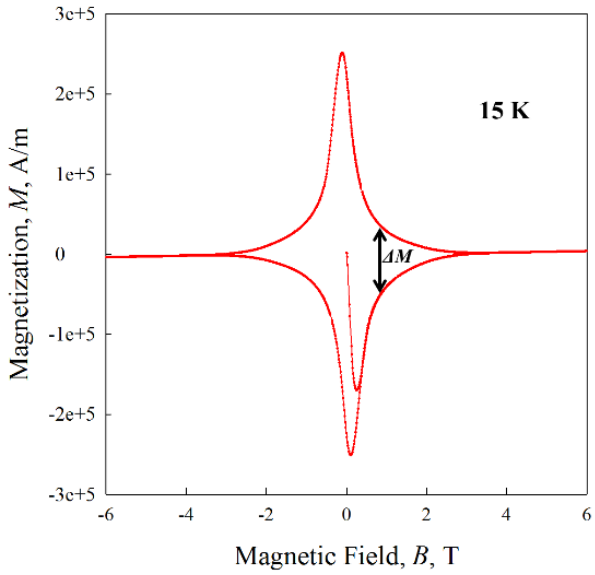

Figure 29 A typical VSM-measured *M*-*B* curve of a MgB_2 specimen.

M-*T* measurement can be used to determine both T_c and B_{c2}. Generally, *M* can be replaced by the DC magnetic susceptibility $\chi = M/\mu_0 B$. When a material is in the superconducting state, its χ is – 1, cf. the Meissner effect described in Section 1.4.1. Figure 30 is the χ -*T* (bottom) and $d\chi/dT$-*T* (top) curves of a MgB_2 sample at 10 mT. The T_c is

determined by the temperature at which the material completely transitions from the superconducting state to the normal state. Repeated recording of T_c at various B can produce a T_c vs B curve. The same data can also be replotted in the format of B_{c2} vs T. The T_c distribution can be expressed by $d\chi/dT$-T and it can be used to indicate the sample homogeneity.

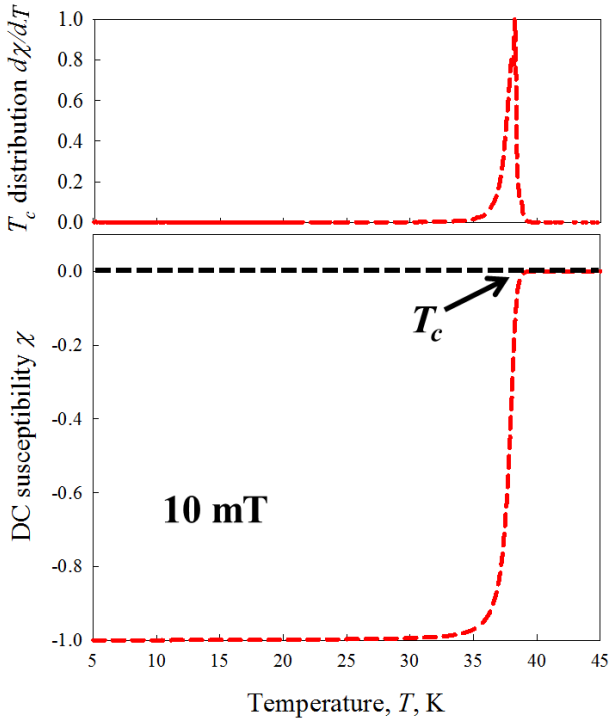

Figure 30 (Bottom) the superconducting critical transition temperature T_c is determined by a DC susceptibility χ vs. T curve. (Top) the T_c distribution expressed by $d\chi/dB$ vs. B plot.

2.7.2 Resistivity Measurements

The DC resistivity measurements were taken with the resistivity option of the PPMS. For this purpose, a sample is mounted on a DC sample puck and its resistivity is measured by the four-point method. To reduce the contact resistance between the sample and the current leads / voltage taps, silver paint is commonly used. The resistivity option has a current limit of 5 mA, with a voltage resolution of 20 nV. During the measurements, the temperature dependent resistance *R(T)* was recorded with a temperature ramp rate less than 1 K/minute to maintain a temperature equilibrium in the sample. As with *M(T)*, the *R(T)* curves can also be used to obtain T_c and B_{c2}.

2.8 Error Analysis

The experimental errors in this work can come from two areas: (i) the measurement techniques and (ii) the sample preparation process. In this section the uncertainties from these two areas are discussed.

a) **Experimental errors caused by the measurement techniques**:

As described in section 2.6, the transport measurements are performed on wire samples to obtain their *V-I* behaviors under certain *B* and *T* by using the four-point method. The current resolution of this technique is 0.01 A. Common errors are: (i) instrumentation issues, such as absence of equipment calibration; (ii) operation issues, such as samples are not placed in the homogeneous-field portion of the magnet; (iii) sample mounting issues, such as voltage taps are not soldered on the center segment of the sample or the voltage tap

separation is too large; (iv) sample damage issues, such as bending and dropping which can cause significant damage. To eliminate these errors, routine inspection and calibration are required for all the equipment in the transport measurement system. Samples need to carefully handled and mounted onto the sample probe. During the measurements, all operations need to be careful and slow to reduce the chance of damaging the samples. To demonstrate the repeatability of the transport measurement system, a standard NbTi sample was measured multiple times at 4.2 K and its *V-I* curves were consistent with each other. Based on the study on this NbTi, the intrinsic error of the transport measurement is about 2%.

The magnetic measurements in this work are mainly performed on a Quantum Design Model 6000 Physical Property Measurement System (PPMS) described in the section 2.7. For each technique in this instrument, the measurement resolutions were already described in the section 2.7.1 – 2.7.3.

b) **Experimental errors caused by the sample preparation**:

Two types of samples are involved: wires and bulk. As described in the section 2.2, all wires in this work are fabricated by the CTFF process. To ensure the wire quality, repeated studies are performed on various long MgB_2 wires made by the CTFF process. In each of these studies, multiple samples were taken from different locations in the long MgB_2 wires and their J_c values were measured at 4.2 K. After comparison, a 10% deviation in their J_c-B performance at 4.2 K was observed. Figure 31 shows the results of the repeatability tests on a 2% C doped MgB_2 PIT multifilamentary wire.

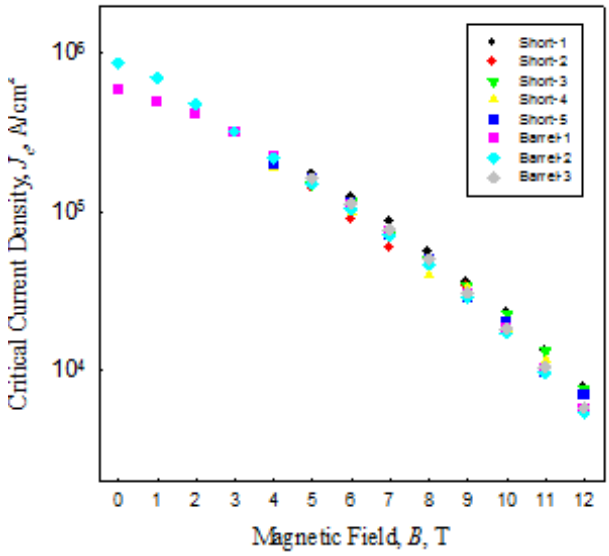

Figure 31 4.2K transport measurements were made on eight samples from a 2% C doped MgB_2 PIT multifilamentary wire. The gauge lengths of barrels and short samples were 50 cm and 50 mm, respectively. The electric field criterion E_c=1μV/cm [199].

In the MgB_2 bulk synthesis, the sample quality is mainly controlled by the purities of the starting materials, the material handling, and the accuracy of the heat treatment furnaces. All materials used in this work (mainly purchased from Alfa Aesar and Sigma-Aldrich) had very high purities (e.g. Mg turnings: 99.8%, B powder: 99.98%) and were carefully stored in inert gas (e.g. Ar). During the sample fabrication, the precursors were carefully weighted and mixed in a Ar-filled glove box. In some cases, ball milling was used to mix and refine the precursor powders. In doing so, a stainless steel jar and stainless steel ball media were used. All precursors were placed in the stainless steel jar with stainless steel ball media in the glove box to ensure that the materials were milled in Ar environment. After milling, the jar was opened in the glove box. All bulk samples were heat treated in an Ar environment. To further prevent contamination (especially oxygen contamination),

oxygen getters (e.g., Nb strips, Ta foils) were added during the heat treatment. Two furnaces were used in this work. A tube furnace was used to make the conventional *in situ* bulk, and an induction furnace was used to synthesize the HPT bulk as described in Section 2.1. For the tube furnace, a type K thermocouple probe from Omega with was used. The temperature equilibrium zone of this tube furnace is 15 cm, which a temperature deviation of ± 5°C at 800 °C. For the induction furnace, two custom type C thermocouple probes with a cold junction were used to ensure temperature accuracy.

Chapter 3: Carbon Doping in *in situ* MgB_2 Superconducting Wires

MgB_2 superconducting materials and strands are relatively simple to make, are available at a reasonable cost. They also have performance specifications that make them of interest for a number of applications, such as MRI, fault current limiters, motors, generators, and various special applications. Numerous successful efforts in MgB_2 wire development have been undertaken [11,126,128-137]. In order to further improve the in-field performance of MgB_2 wires, we try to apply chemical doping on MgB_2 wires.

In this chapter we focus on studying the influence of C doping on transport performance in MgB_2 monofilamentary wires and use the finding to improve the efficiency of C doping. The transport J_c and n-values of MgB_2 wires with various C concentrations were studied and compared. Property optimization of MgB_2 PIT wires consisted of variation of doping concentration and heat treatment parameters. Flux pinning potential U in the undoped PIT, C-doped PIT and C-doped IMD wires was studied by three different approaches and the intrinsic n-values of these samples were calculated and compared. Finally, the C doping in a set of MgB_2 multifilamentary wires was investigated in terms of transport properties, doping techniques, B types, wire structure and strain tolerance.

3.1 Fabrication of *in situ* MgB_2 Wires

State-of-the-art MgB_2 superconducting wires were fabricated by a variant of the *in situ* PIT method, namely the CTFF process described in Section 2.2. The basic procedures and the resulted wire structures are in Figure 32. A series of monofilamentary and multifilamentary strands (the latter with 18 and 36 filaments) were produced. Most of the strands were 0.83 mm in diameter; they included a thick chemical barrier (typically of Nb but in some cases Fe), and outer sheaths of either Monel 400® (henceforth "monel", a nickel-copper alloy) or monel associated with Cu, GlidCop® (henceforth "glidcop", an oxide-dispersion-strengthened Cu), or Nb. The basic powder ingredients were commercial Mg powders (99%, ≈ 20-25 μm particle size) and B powder from one of two sources: (i) "Ts-boron" from the Tangshan Weihao Magnesium Powder Co. Ltd., produced using the Moissan process; and (ii) "SMI-boron" from Specialty Metals Inc., produced in a plasma torch by the reduction-by-hydrogen of BCl_3. Also included from time to time in the starting B powders were small percentages of the dopant C, introduced: (i) by the moderate temperature drying out of a slurry of B mixed in with a malic-acid-toluene solution, during which the malic acid decomposed leaving C as the only solid residue [89, 91], and (ii) direct C doping of the SMI-produced B by including a known percentage of CH_4 into the plasma flame [92]. After being drawn to size the strands were heat treated at temperatures of 675°C to 750°C for times of 20 to 120 min.

Two set of MgB_2 monofilamentary wires were fabricated through the IMD process described in Section 2.2, in which both Ts B and SIM boron with 2 at. % C was used. These wires all had Nb barriers and a monel outer sheaths.

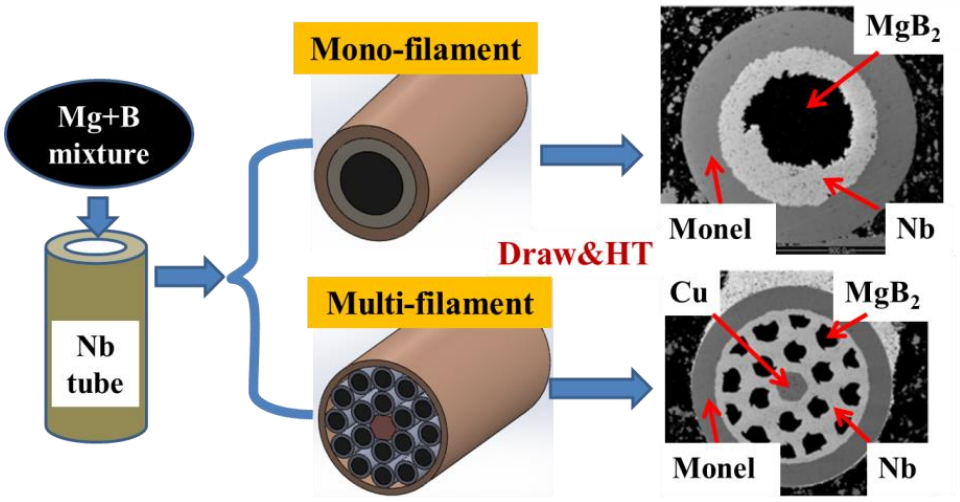

Figure 32 A schematic diagram of monofilamentary and multifilamentary MgB_2 PIT wires fabricated by the *in situ* PIT process.

Niobium was used as the "chemical barrier" material for most of the wires described here since it has minimal reaction with the Mg and B powders during the reaction heat treatment. Iron was used as a chemical barrier (as a replacement for Nb) for a few strand types, but required some intermediate annealing during wire drawing. Monel was the outer sheath for most strands because of its high flow strength in combination with its ductility, although it was in a few cases laminated with glidcop or pure Cu in the interests of electric stability. Microstructure images were obtained for several samples using a Sirion field emission SEM in backscatter mode in Figure 33. Figure 33 (a) shows a simple

monofilament with Nb barriers and an outer monel sheath. Figure 33 (b)-(g) show the various multifilamentary strand geometries. Strands (b) and (c) are 18 and 36 filament variants of Nb-chemical barrier strands with the Nb-clad filaments packed together inside a monel sheath. In thesis cases no Cu matrix separates the Nb filaments. Instead a central Cu filament (Nb for strand b*) was placed in the center of the multifilamentary arrangement, for both mechanical and electric reasons -- (i) to minimize centerburst (an instability related to flow stress gradients through the strand diameter during wire drawing), and (ii) to aid strand stability. Strand (d) consisted of 36 filaments in a double wall sheath of Cu and monel (and a central Cu filament), while strand (e), with 18 superconducting filaments plus a central Cu filament, used a monel/glidcop double wall sheath. Strand (f) which consisted of 18 filaments protected by Fe chemical barriers, had no Cu matrix, and used a monel outer sheath. Strand (g) had a Nb wrap around the Fe-clad filaments but otherwise was similar to strand (f). Figure 33 (h) shows the structure of an IMD wire with a Nb barrier and a monel outer sheath.

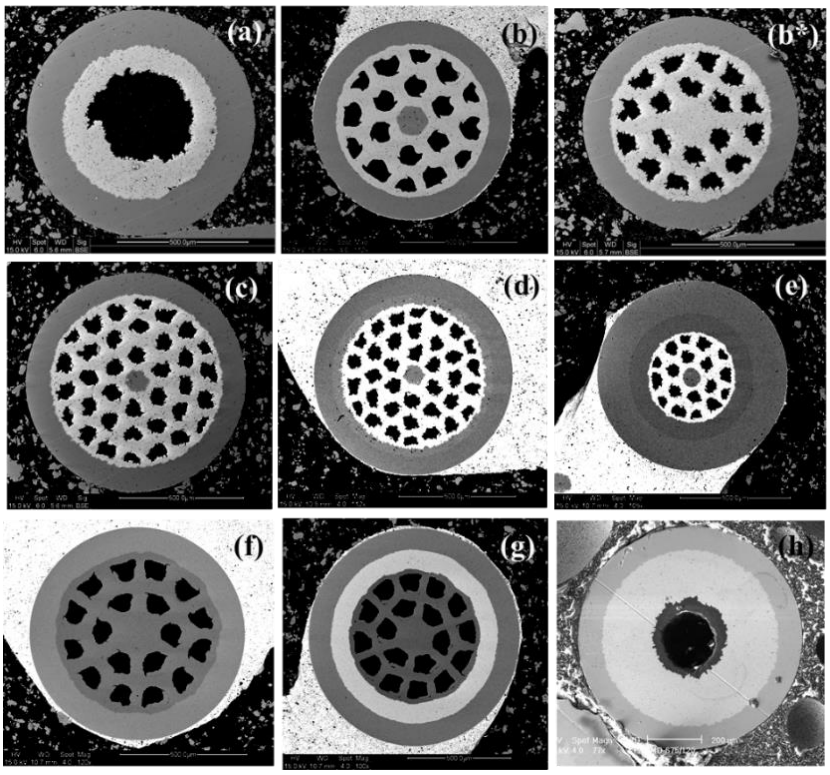

Figure 33 SEM-backscatter images of a set of representative strands [192].

3.1 Enhanced Transport properties in the MgB_2 Monofilamentary Wires by Using C pre-doping method

Transport measurements were made on the MgB_2 monofilamantary PIT wires with various C amounts from 0 at. % to 4.32 at. % in the "short sample" form at the usual gauge length of 5 mm. The sample specifications are listed in Table 2. The actual C amounts in the wires as listed in Table 2 were estimated using LECO CS600 inorganic combustion analyzer on the SMI predoped B powders.

Table 2 Sample specification for C doped MgB_2 PIT wires

Sample	Tracer No[1]	Actual C (at. %)[2]	%SC[3]	OD (mm)
P-00	2134	0	25.2	0.834
P-01	1990	1.25	18.3	0.834
P-02	1650	2.09	15.2	0.834
P-03	1991	3.15	13.1	0.834
P-04	1952	4.32	11.5	0.834

[1] Tracer No is the internal tracking numbers for MgB_2 wires fabricated by Hyper Tech Research Inc.;
[2] Actual C (at. %) is calculated by assuming all C in the pre-doped SMI B was doped in the MgB_2;
[3] %SC is the average area fraction of MgB_2 core in the MgB2 wires: $\%SC=A_{MgB2core}/A_{wire}$;

Each sample was reacted according to two different heat treatment plans: (i) 675 ºC for 20 minutes and (ii) 700 ºC for 20 minutes. The field dependent transport J_c of these wires at 4.2 K is represented in Figure 34 and the values at 6T and 10T are given in Table 3. It is clear that the transport J_c especially at high field regime (B>5T) gradually increased with increasing C amount until the C doping level was above 3.15 at.%. For instance, at 10 T the J_c of the P-03 with 3.15 at% C is ~3.2×10^4 A/cm^2 which is about 60 times higher than that of the undoped sample P-00. The best J_c value of this series at 14T and 4.2K, viz. 7×10^3A/cm^2, was obtained in P-03.

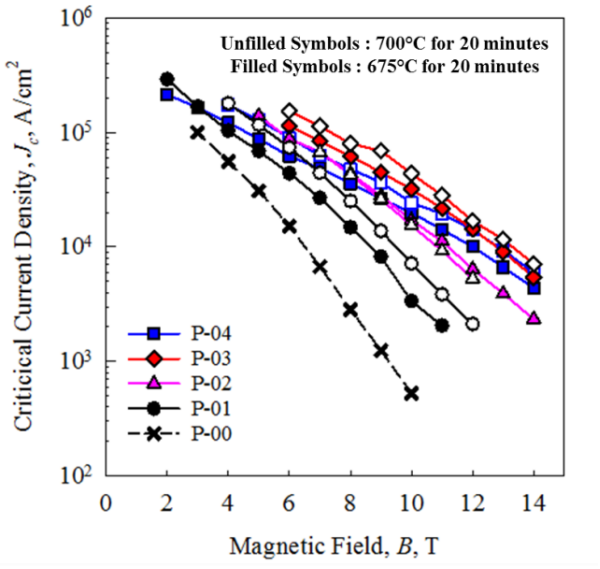

Figure 34 4.2 K transport J_c vs. B for MgB_2 wires with various C amounts [193].

Table 3 4.2K J_c for the MgB_2 wires at 6T and 10T.

Sample	HTs	J_c (A/cm^2)	
		6T	10T
P-00	675°C/20min	15197	528
P-01	675°C/20min	43987	3360
	700°C/20min	73720	7167
P-02	675°C/20min	87995	17122
	700°C/20min	87802	15483
P-03	675°C/20min	113397	31778
	700°C/20min	154179	43620
P-04	675°C/20min	62060	19846
	700°C/20min	90302	24309

Figure 35 illustrates field enhancement at J_c=10^4 A/cm^2, B(10^4 A/cm^2), with respect to C doping amounts. Beyond 3 at. % C doping, the J_c decreases suggesting that the saturation of C doping under the heat treatments specified. Adding more C possibly causes

the formation of C contained non-superconducting phases which reduce the connectivity in the MgB_2 wires [93], and hence the transport J_c. Generally, it was seen that, all other parameters being equal, samples treated at a higher temperature (700°C) showed better transport properties than those samples treated at a lower temperature for the same duration (675°C), except P-02 which contained 2.09 at. % C. This observation stimulates us to study the effect of heat treatment temperature and duration on the C doping efficiency, to be discussed in Section 3.2, below.

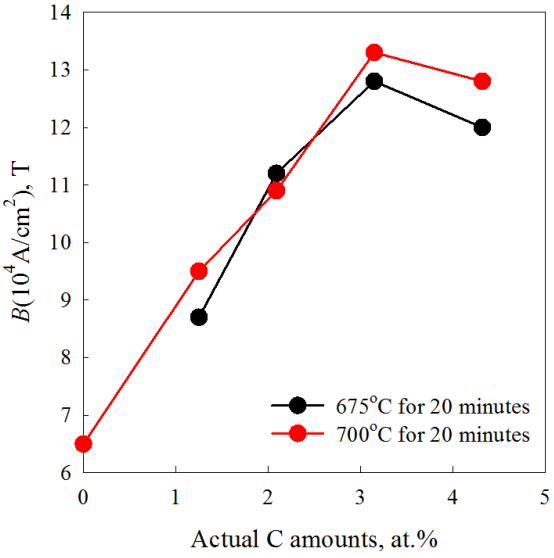

Figure 35 The magnetic field B (at which J_c can arrive $10^4 A/cm^2$) vs. actual C doping amounts at different heat treatment parameters.

Further research by Susner et al. [93] on the samples HTed at 700°C for 20 minutes showed that the B_{c2} at low temperatures (T<20K) was to be increased by C doping. However, the B_{c2} at high temperatures (T>25K) of the C doped samples was decreased, Figure 36. This disadvantage of C doping (mentioned in Section 1.5.1) has been studied by

many authors [83-86]. By way of explanation we note that T_c decreases in response to C doping.

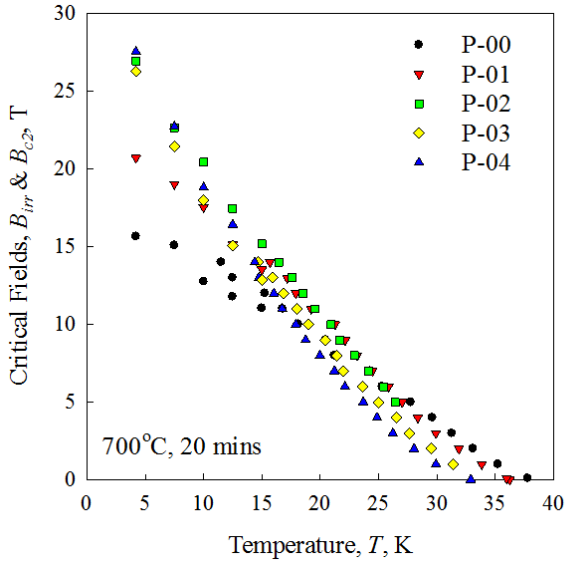

Figure 36 B_{c2} vs. T curves of the MgB_2 wires with various C amounts [93].

Variable-temperature J_c measurements up to 25 K were performed on the P-00 and P-03 HT at 700 ºC for 20 minutes. As shown in Figure 37, P-03 showed better J_cs at all measured fields than those in the undoped P-00 at low temperatures (T≤17.5K); at 20 K the C doped sample still showed better transport performance at high fields (B>2T), e.g., the J_c of P-03 at 4T is 2×10^4A/cm^2 which is about 3 times higher than that of P-00; however, when T increase above 20K, the J_c values of P-03 are comparable to, if not worse than, those of P-00 at all measured fields. This observation is consistent with the B_{c2} vs T results in Figure 36 and supports that C doping is in effective at high temperatures (T>20K).

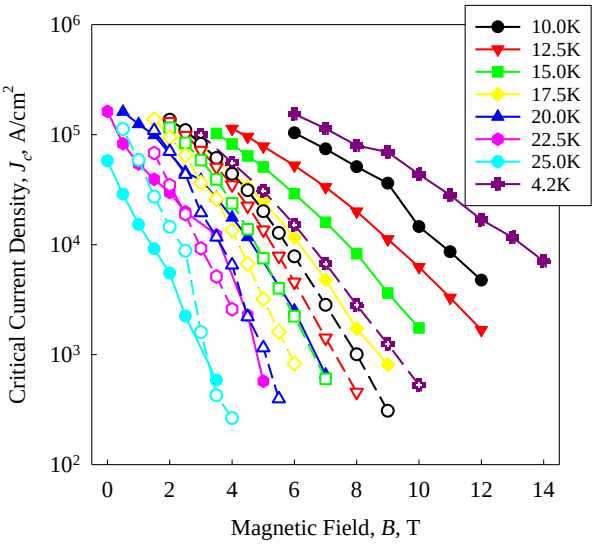

Figure 37 Transport J_c vs. B curves at various T of P-00 (filled symbols) and P-03 (unfilled symbols) [194].

3.2 The Influence of Heat Treatment Parameters on the C Doping Efficiency in the MgB_2 Monofilamentary Wires by Using C Pre-Doping Method

Carbon doping is useful for increasing the B_{c2} and the high field J_c and therefore is especially important for the windings of high field magnets [8, 70, 87, 88, 93]. In order to improve the C doping efficiency, further research is needed. Variable heat treatments (625°C - 750°C and 30 minutes – 480 minutes) were applied on the 2% C doped wire P-02 and the related parameters are listed in Table 4. For the high HT temperatures (700°C and 750°C), short to medium durations t were used to prevent the possible reaction between MgB_2 core and the Nb chemical barrier as well as leakage through gaps in the sheath. All

HTs were performed in a tube furnace with a Ar gas flow to minimize the oxygen contamination.

Table 4 Heat treatment parameters of P-02

T_{HT},°C / t,min.	625	650	675	700	750
30	P-02-625-30	P-02-650-30	P-02-675-30	P-02-700-30	P-02-750-30
60	P-02-625-60	P-02-650-60	P-02-675-60	P-02-700-60	P-02-750-60
120	P-02-625-120	P-02-650-120	P-02-675-120	P-02-700-120	P-02-750-120
240	P-02-625-240	P-02-650-240	P-02-675-240	P-02-700-240	-
480	P-02-625-480	P-02-650-480	P-02-675-480	-	-

The transport J_c vs B curves are plotted in Figure 38 and the J_c values at 10 T are listed in Table 5 (the samples which were resistive are not present). The best transport J_c vs. B performance is exhibited by the samples heat treated at 625 °C for 480 minutes and at 650 °C for 120 minutes. For example, their $J_{c,4.2K}$(10 T) values are 2.33×10^4A/cm^2 and 2.17×10^4A/cm^2, which are about 10 times and 9 times higher than that of P-02-625-60, respectively. The results in Figure 38 and Table 5 indicate that HTs at low temperatures and long durations work best for MgB_2 wires made by the C pre-doping method. On the other hand, if a higher T_{HT} is used, a shorter HT time, t, is preferred to optimize the transport performance, e.g., P-02 HTed at 675 °C for 60 minutes and 700 °C for 30 minutes show good $J_{c,4.2K}$ results at 10 T (1.69×10^4A/cm^2 and 1.41×10^4A/cm^2, respectively).

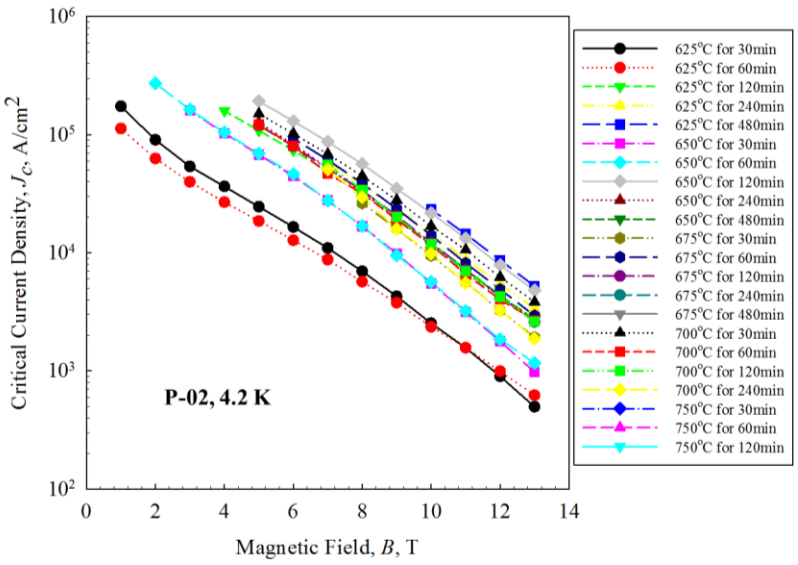

Figure 38 Transport J_c vs. B curves of P-02 with various different HTs at 4.2K [195].

Table 5 The 4.2 K J_c values of P-02 with various HTs at 10T in the decreasing order.

J_c at 10T, 10^4A/cm	Sample
2.33	P02-625-480
2.17	P02-650-120
1.69	P02-700-30
1.48	P02-625-240
1.41	P02-675-60
1.37	P02-700-60
1.22	P02-675-120
1.2	P02-625-120
1.17	P02-650-240
1.16	P02-700-120
1.06	P02-675-240
0.97	P02-700-240
0.95	P02-675-30
0.57	P02-650-60
0.55	P02-650-30
0.25	P02-625-30
0.24	P02-625-60

Figure 39 shows the 10 T $J_{c,4.2K}$ vs. t curves corresponding to various HT temperatures, T_{HT}. It is clear that the J_c increases strongly with increasing t at 625°C. Since this temperature is still below the melting point of Mg (650°C), the reaction between Mg and B is slow. Thus unreacted B could still exist even in the sample HT for 480 minutes. One can imagine that the J_c will keep increasing with longer t until all the unreacted B converts into MgB_2. When T_{HT} rises above 650°C, Mg melts and the reaction accelerates. As a result, it takes a shorter time to fully convert B to MgB_2. After this, longer HT time may cause negative effects on the properties of these samples by either grain coarsening (at higher T) or Mg deficiency (at T>650°C), e.g., the best t at 650°C is 120 minutes and longer t reduces its J_c, Figure 39. Further HT may also cause damage to the Nb barrier and monel outer sheath which eventually result in the failure of the wires. For example, the sample HT at 650°C for 480 minutes is resistive. Moreover, the higher T_{HT} requires shorter t to poison the superconductor. As shown in Table 5, the sample becomes resistive when HTed at 675°C for 480 minutes, while at 750°C the sample becomes resistive after only 30 minutes HT. With regard to practical wire manufacturing, both the superconducting properties and heat treatment parameters (T_{HT} and t) need to be balanced in terms of cost and efficiency. The best HTs for the C pre-doped MgB_2 wires are 675°C for 60 minutes and 700°C for 30 minutes.

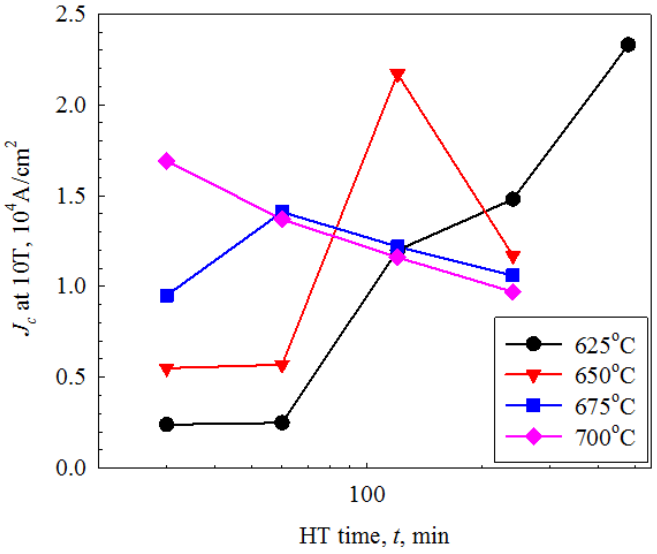

Figure 39 The 10 T J_c of P-02 with various HT parameters.

3.3 The Effects of C Doping on the *n*-Values and Flux Pinning Potential *U* in the MgB_2 Wires

The *n*-value is a parameter in both transport performance and industrial application. Not only does it represent the sharpness of the superconducting transition of practical conductors but it is directly related to the flux pinning potential *U* [153,197,198]. As described in Section 2.6, sausaging, cracks, inhomogeneity and low connectivity can degrade *n*-value, making it difficult to deduce the intrinsic *n*-value of MgB_2 wires. In this section three approaches are applied to a set of MgB_2 monofilamentary wires to investigate the effects of C doping on the intrinsic *n*-value, viz. transport, magnetic, and resistive measurements.

To eliminate the influence of sample inhomogeneity and wire structure, three MgB_2 monofilamentary wires including a undoped PIT wire (P-00), a 2 at. % C doped PIT wire (P-02) and a 2 at. % C doped IMD wire (I-02) were selected. The sample specifications are listed in Table 6. Both P-02 and I-02 were fabricated by the C pre-doping process. All samples were heat treated at 675°C for 60 minutes. In these three samples, I-02 has much higher connectivity (close to 100%) than those of P-00 and P-02 (about 30%) as I-02 was made by previous mentioned IMD method (Section 2.2).

Table 6 Specifications of samples of intrinsic *n*-value study

Sample	Tracer No	Actual C (at. %)	%SC	OD (mm)
P-00	2134	0	25.2	0.834
P-02	1650	2.09	15.2	0.834
I-02	2281	2.09	5.2	0.834

3.3.1 Transport measurement of *n*-value

First, variable-temperature transport measurements were performed on these samples and their *V*-*I* curves at various *B* and *T* were recorded. Based on equation (28), the *n*-values were extracted from the slopes of linear regressions of log*V*-log*I* plotted data. For example, Figure 40, the log*V* vs. log*I* of P-02 at 4.2 K. The solid lines are linear fits and the *n*-value is the slope of these lines [199] which were based on the data ranging from E_c to $20E_c$, where E_c is the electric field criterion (E_c=1μV/cm). The resulting transport-based

n-values, viz. tran-*n*-values, for all three samples are plotted in Figure 41. As described in Section 2.2, the IMD processed MgB_2 wires have much higher longitudinal connectivity than those of PIT wires. As a result, it is to be expected that the sample I-02 has the best tran-*n*-values at all measured *T* and *B* since the transport results are directly affected by the sample connectivity.

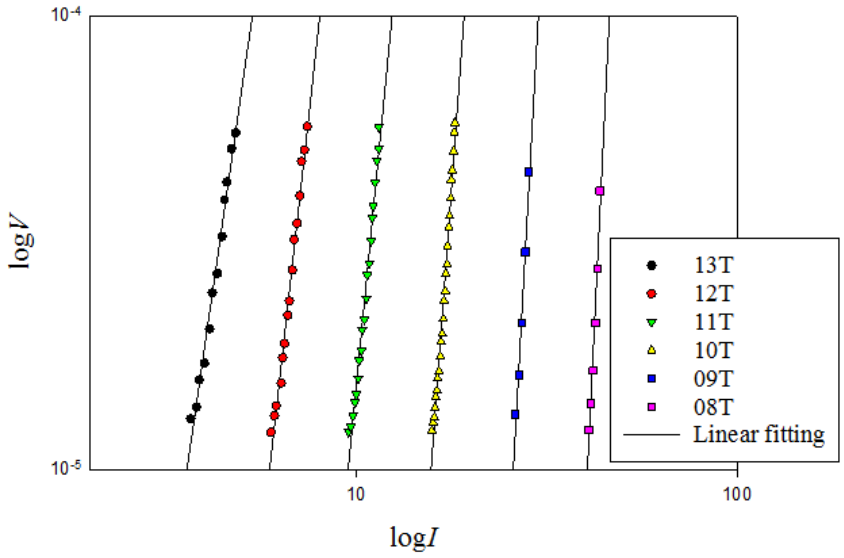

Figure 40 The log*V* vs. log*I* of P-02 at 4.2K. The solid lines are linear fits and the *n*-values are the slopes of these lines [199].

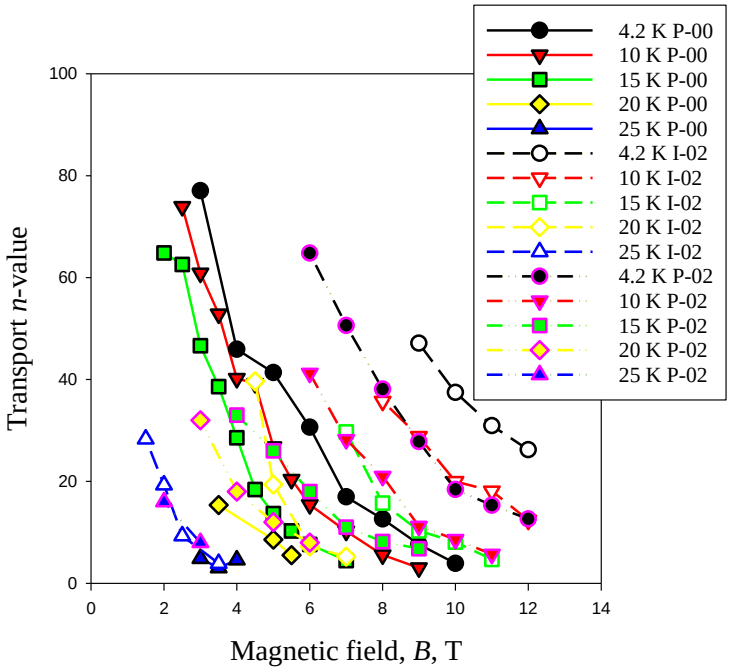

Figure 41 The *n*-values of P-00, P-02 and I-02 extracted from transport measurements.

Many authors [148,150,151,166,204] observed *n*-value field dependencies of the form:

$$n \propto e^{-m \cdot B} \tag{30}$$

where *m* is a fitting parameter. Figure 42 shows the fitting for the tran-*n*-values of the present three wires at 4.2 K. It is clear that these tran-*n*-values are a good fit to equation (30).

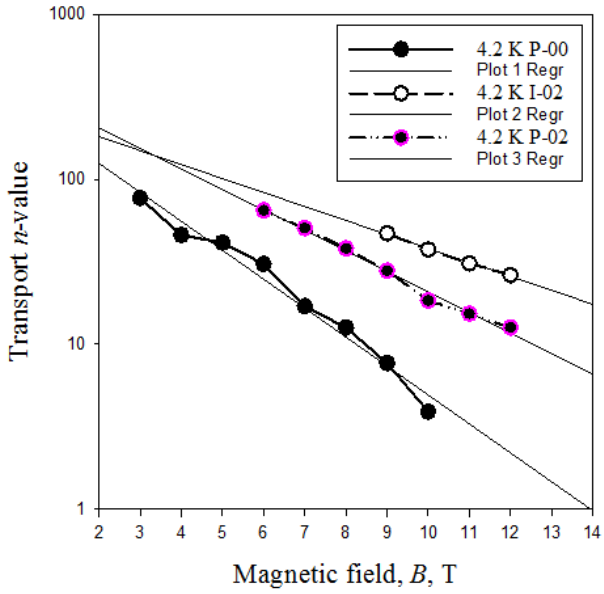

Figure 42 The tran-*n* vs. *B* curves at 4.2 K fitted to $n \propto e^{-m \cdot B}$.

Based on the Anderson-Kim model [198], the intrinsic *n*-value can be related to the pinning potential by:

$$n(T) = \frac{U}{k_B T} \tag{31}$$

where U is the pinning potential and k_B is the Boltzmann constant. Thus the pinning potential U can be calculated by substituting the tran-*n*-values in the equation (31). The 4.2 K results are listed in Table 7. The values marked (*) are taken from the fitting in Figure 42. Compared with the literature values for MgB_2 in columns 7-9, the deduced U in P-00 is relatively small. On the other hand, the U values of the C doped wire P-02 are comparable to those of a SiC doped MgB_2 wires [200]. The C doped IMD wire I-02 has higher U which exceeds the literature values at B > 6T. Based on the comparison of the U values between these three samples, it seems that there are two factors contributing to the difference in the

pinning potentials: (i) the C doping, which can significantly increases *U* from ~11 meV to ~23 meV at 6 T and 4.2 K with 2 at% C; (ii) the connectivity (I-02 has much higher connectivity than P-02), which causes the artifacts (mentioned earlier) in the *n*-value measurements, hence affects calculated *U*, e.g., at 10T the *U* value of I-02 is about twice as high as that of P-02.

Table 7 Comparison of the tran-*n*-values and *U*. The marked (*) values are estimated by the fits for the equation (30)

B, T	P-00		P-02		I-02		*U*, meV [200]	*U*, meV [201]	*U*, meV [202]
	Tran-n 4.2K	*U*, meV	*Tran-n 4.2K*	*U*, meV	*Tran-n 4.2K*	*U*, meV			
2	123.00*	44.52*	195.00*	70.57*	181.00*	65.51*	178.00	86.17	129.26
3	77.06	27.89	157.00*	56.82*	142.00*	51.39*	71.00		
4	45.92	16.62	109.00*	39.45*	115.00*	41.62*	42.00	25.85	34.47
5	41.33	14.96	85.00*	30.76*	98.00*	35.47*			
6	30.61	11.08	64.80	23.45	82.00*	29.68*	12.2		
7	16.96	6.14	50.60	18.31	67.00*	24.25*	9.10		
8	12.60	4.56	38.10	13.79	58.00	20.99	6.40		
9	7.67	2.78	27.80	10.06	47.10	17.05	4.70		
10	3.90	1.41	18.40	6.66	37.50	13.57	3.8		
11	3.00*	1.09*	15.30	5.54	30.90	11.18			
12	2.00*	0.72*	12.60	4.56	26.20	9.48			

3.3.2 Magnetic measurement of *n*-value

Magnetic measurements at field sweep rate *dB/dt* varying from 3 mT/s to 13 mT/s were performed at various temperatures based on which the magnetic critical current density J_{cm} was calculated by using the equation:

$$J_{cm} = \frac{3\pi\Delta M}{4d} \tag{32}$$

where d is the diameter of MgB_2 core in the wire. The field dependent J_{cm}s of P-00 at 4.2 – 25 K are plotted in Figure 43.

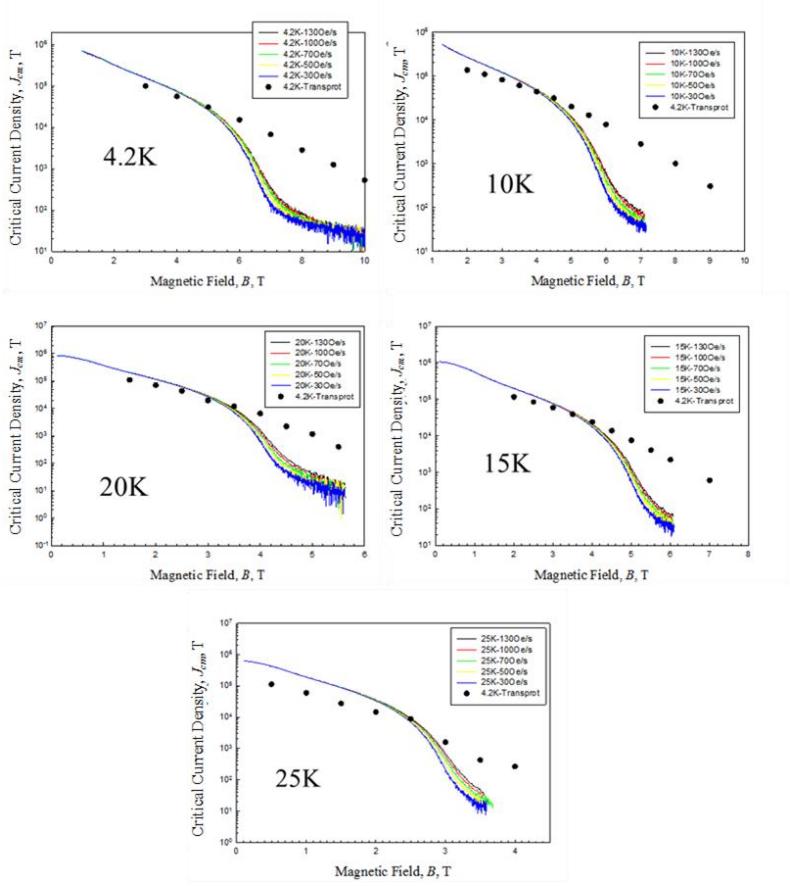

Figure 43 The J_{cm} vs. B of P-00 at various T. The sweep rate *dB/dt* is from 3 mT/s to 13 mT/s [199].

The mag-*n*-values are deduced by applying the Maxwell-Faraday equation:

$$\nabla \times E = -\frac{\partial B}{\partial t} \tag{33}$$

where E is the electric field. A time-varying magnetic field dB/dt can generate an electric field E in the same direction as longitudinal magnetic J_c, similar to the transport situation. Therefore, the electrical field criterion E_c for each sweep rates are given by:

$$\frac{dE_c}{dx} = -\frac{dB}{dt} \rightarrow E_c = -\int \frac{dB}{dt} dx = -\frac{dB}{dt} \times \frac{d}{2} \tag{34}$$

where d is the diameter of MgB_2 core in the wire. Each E_c associates with a J_c-B curves. Use equation (28) again, plot *logE* vs. *logJ* and linearly fit the results to get the slopes which are *n*-values (viz. mag-*n*-value) for magnetic measurements in Figure 44.

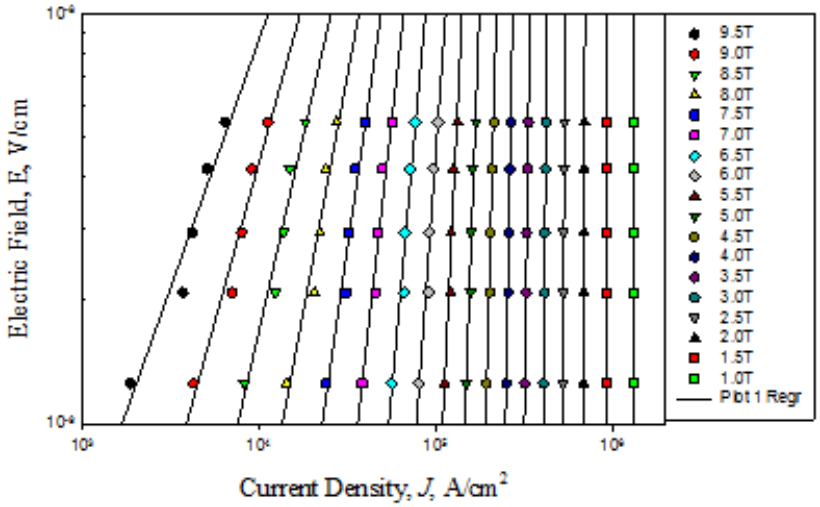

Figure 44 The log*E* vs. log*J* of P-00 at 4.2K. The solid lines are linear fitting and the *n*-value is the slope of these lines [199].

The mag-*n*-values for the undoped P-00 are plotted in Figure 45. Similar to the tran-*n*-values, the field dependency of mag-*n*-values also obeys the equation (30). However, the fitting parameters *m* (viz. the slopes of the linear fitting in Figure 45) of the mag-*n*-values are much larger than those of the tran-*n*-values over the whole temperature range of 4.2K – 25K. Therefore, the field dependencies of these *n*-values (both transport and magnetic) pivot at certain field below which the mag-*n*-values are much better above and visa vice.

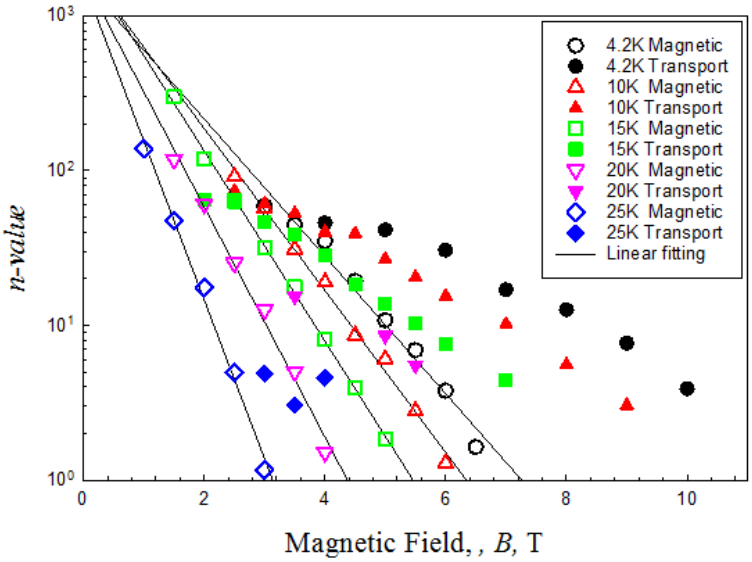

Figure 45 The *n*-values of P-00 obtained from magnetic measurements (unfilled symbols) and transport measurements (filled symbols). The solid lines are fits of mag-*n*-values to $n \propto e^{-m \cdot B}$[199].

Two factors may cause this pivoting behavior. First, the ranges of the electric field *E* are different. In the transport measurements, *E* is usually from 0.1μV/cm to 100 μV/cm, while the sweep rate induced *E* in the magnetic measurements are much smaller (0.006μV/cm – 0.027μV/cm). This difference in the electric field ranges of these two

measurements can lead to variations in the slope values taken from the linear fitting of log$E$-log$J$ curves. The other factor is that the pinning potential U can be significantly lower than its intrinsic value by the presence of macroscopic currents in the sample [153]. In comparison to the transport measurement in which the current flows only in the longitudinal direction, the current in the magnetic measurement, which flows in a loop, consists of a transverse component and a longitudinal component. At high fields, the transverse component of J_{cm} limits the overall current in the loop, which causes the deviation of the J_{cm} from the transport critical current density J_{ct} [200]. This phenomenon has been investigated by Shi *et al.* [200] and a "rooftop" model has been developed to explain this deviation.

3.3.3 Resistive measurement of *n*-value

Based on the discussion above, it is clear that the n-value and the pinning potential U taken from both transport and magnetic measurements are underestimated. This underestimation is caused not only by the electric field variations but also by reduction due to the sample connectivity (transport) and the transverse current limitation (magnetic). Also, a macroscopic current present in the sample can reduce its U hence n-value below their intrinsic values. How to eliminate these three problems? One approach is the in-field resistivity measurement. In this measurement, a very small DC current (5 mA) flows into the wire sample and the voltage is recorded on a ~2.5 mm gauge length at temperatures

ranging from 5 K to 45 K as well as magnetic fields ranging from 0 T to 14 T. Since the current used in the resistivity measurement is very small compared to those of the transport and magnetic measurements, the influence of connectivity is negligible. Also the current only flows in the longitudinal direction as in the transport measurement, therefore there are no limitation due to cause by the transverse current. Further, the reduction of the pinning potential U caused by the present current is also very small. Based on these advantages, the resistivity measurement provides a chance to investigate the intrinsic values of n and U in MgB_2 wires.

The resistivity ρ introduced by thermally activated flux creep during the transition correlating to the Arrhenius equation [153,203] is:

$$\rho = \rho_o \exp(-\frac{U}{k_B T}) \tag{35}$$

Assuming U to be temperature independent, the slope of ln ρ vs. $1/T$ is equal to $\sim U/k_B$. Figure 46 (a) shows the results obtained from the resistivity measurement on P-00. Only the ρ-T data at the transition region ($\Delta T<5K$) are used to calculate U. Figure 46 (b) shows the ln(ρ) vs. 1/T curves. The U is determined by the slope of the linear fitting and the RT-n-value can be deduced using the equation (31).

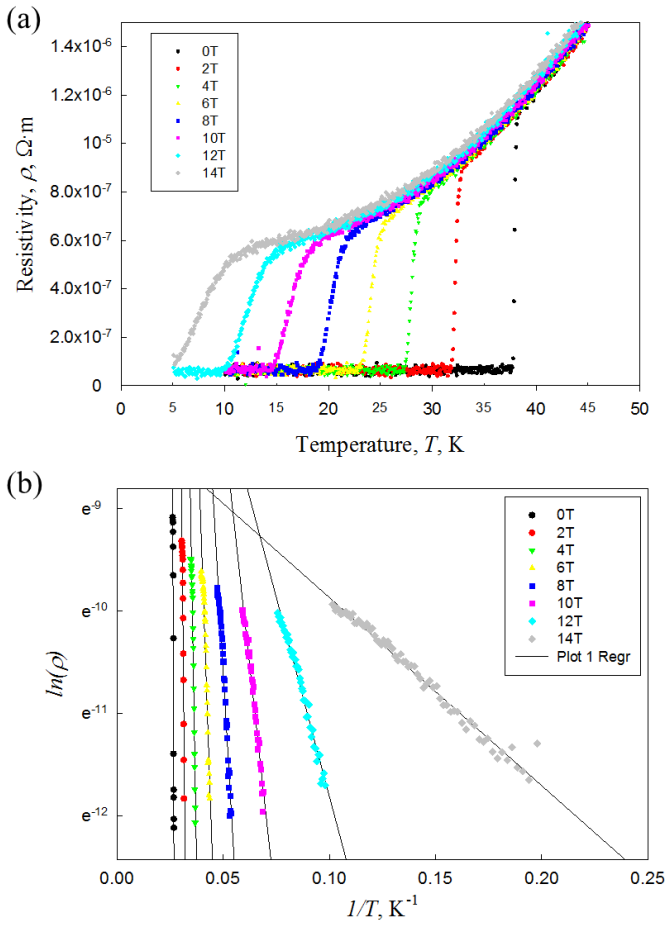

Figure 46 (a) ρ-T curves of P-00 at various B; (b) ln(ρ) vs. 1/T curves of the transition regime in (a). Solid lines in (b) are linear fittings [199].

3.3.4 Comparison of *n*-value

The 4.2 K RT-*n*-values for all three samples (Table 6) are plotted in Figure 47. These values are notably higher than those obtained by both transport measurement and magnetic measurement, which may be close to the intrinsic *n*-values. Compared to those

of P-02, the *n*-values of I-02 are slightly higher and their log *n*-*B* curves are more or less parallel (viz. *m* is the same). This observation supports the idea that resistivity measurement eliminates the connectivity-caused variations, recognizing that I-02 has much higher connectivity than P-02. Comparing P-00 and P-02, their RT-*n*-values are identical at 0T; however, P-02 has larger *n*-values than P-00 at any field above 0 T. The slope of the log *n*-*B* curve of P-00 is greater than that of P-02. Since both P-00 and P-02 were made by using the same process and materials except that P-02 has the 2 at. % C addition, this difference in the log *n*-*B* behaviors is caused by C doping. Thus, both the intrinsic *n*-values and the pinning potential *U* can be enhanced by C doping, especially at high fields.

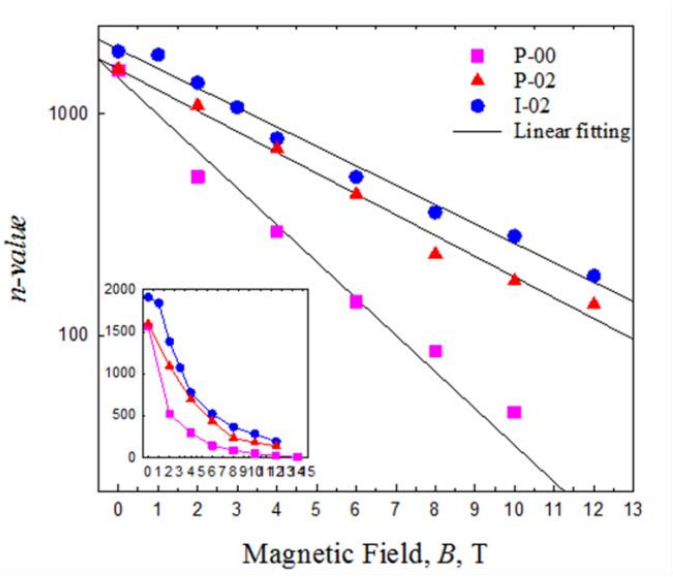

Figure 47 The RT-*n*-values of P-00, P-02 and I-02. Solid lines are the fits to $n \propto e^{-m \cdot B}$. Inset are the same data plotted linearly [199].

3.4 Transport properties of MgB_2 PIT Multifilamentary Wires by Using C Pre-Doped Boron

For practical applications, MgB_2 wires are required to be multifilamentary. Thus this section focuses on the effects of C doping in MgB_2 PIT multifilamentary wires. A series of MgB_2 strands was fabricated by Hyper Tech Research, Inc. (HTR) from SMI-boron pre-doped with three different levels of carbon. Their specifications are listed in Table 8. Transport J_c measurements were performed on these MgB_2 strands in the ITER barrel form with the gauge length of 500 mm and at an electric field criterion of 1 μV/cm. The J_c values and *n*-values are depicted in and presented in order of decreasing 5 T and 10 T J_c in Table 9. Carbon levels for distinct mixtures of SMI C-doped powders were confirmed by C-analysis performed by LECO. The strands designated SMI-C1%, SMI-C2%, and SMI-C4% had measured C levels of 1.29 mol.%, 2.10 mol.%, and 4.0 mol.%, respectively. These strands had 18 sub-filaments, 0.83 mm OD, with Nb chemical barriers and an outer monel sheaths.

Table 8 Specifications of C pre-doped wires

Sample Name	HTR Tracer No	Actual C (mol %)[c]	Chemical Barrier	Sheath	Fil. Count	HT (C°/min)	%SC	OD (mm)
SMI Boron Samples								
B-SMI-C1%-675/20	2110	1.4%	Nb	M	18	675/20	23.6	0.834
B-SMI-C1%-700/20	2110	1.4%	Nb	M	18	700/20	23.6	0.834
B-SMI-C2%-675/60-a	2115	2.3%	Nb	M	18	675/60	22.7	0.834
B-SMI-C2%-675/60-b	2163	2.3%	Nb	M	18	675/60	25.8	0.834
B-SMI-C2%-700/120	2115	2.3%	Nb	M	18	700/120	20.1	0.984
B-SMI-C2%-700/60	2163	2.3%	Nb	M	18	700/60	25.8	0.834
B-SMI-C2%-T-675/60	2115T	2.3%	Nb	M	18	675/60	22.7	0.83
B-SMI-C2%-T-700/60	2115TA	2.3%	Nb	M	18	700/60	22.7	0.83
B-SMI-C4%-675/60	2158	4.8%	Nb	M	18	675/60	15.4	0.834
B-SMI-C4%-700/60	2158	4.8%	Nb	M	18	700/60	15.4	0.834[1]

Explanation of the Sample Name:
(1) The prefixes "B" refers to the strand architecture (b) depicted in Figure 1
(2) The letters "a" and "b" attached to otherwise "similar" samples designate variations in %SC as listed. The letter 'T" indicates twisted.
(3) Here mol % is relative to the final MgB2 compound but does not presuppose complete substitution of the C into the B sublattice.

Table 9 4.2 K transport J_c values of SMI-boron strands directly doped with nominal levels of 1%C, 2%C, and 4%C at 5T and 10T, respectively.

Name	J_c at 5T (10^4 A/cm^2)	*n*-value	J_c at 10T (10^4 A/cm^2)	*n*-value
B-SMI-C4%-700/60	20.0†	--	4.6	10.7
B-SMI-C4%-675/60	19.9	21.2	4.1	14.5
B-SMI-C2%-675/60-b	17.1	14.5	2.1	8.9
B-SMI-C2%-700/60	16.0†	--	1.9	8.4
B-SMI-C1%-700/20	6.4	4.3	0.7	5.7
B-SMI-C1%-675/20	4.6	9.5	0.4	6.9

Figure 48 shows J_c increasing rapidly with increasing levels of C doping. The two SMI-C4%-based strands have J_c values of more than 10^4A/cm^2 at 13 T – higher than those of HTR's best SiC-doped strands. The $J_c(B)$ results depicted in Figure 48 clearly indicate their division into three groups depending on C content. At 10 T the J_c of the SMI-C4% pair, at $4x10^4$ A/cm^2, is an order of magnitude higher than that of the SMI-C1% pair and that of the SMI-C2% pair has an intermediate value. An increase of the HT temperature from 675°C to 700°C (both for 60 min) uniformly raises the J_c of SMI-C1% but produces little change in the J_c values of the other strands.

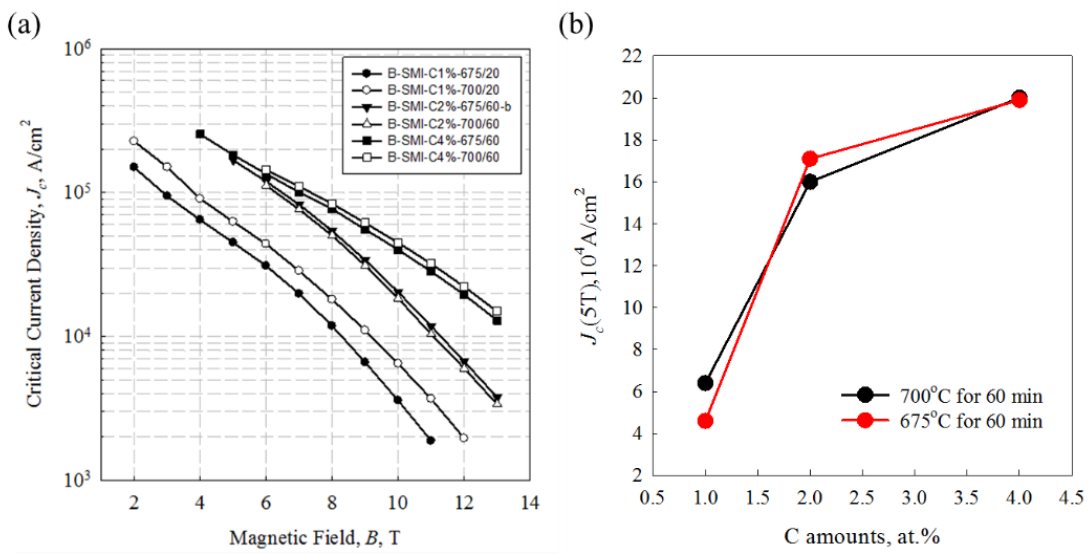

Figure 48 (a) 4.2 K transport J_c vs. B and (b) J_c(5T) vs. %C for SMI-boron strands directly doped with nominal levels of 1%C, 2%C, and 4%C [192].

To a first approximation, the J_c has an exponential field dependence expressed in the form [28]:

$$J_c = J_{c0}.\exp(-B/B_0) \tag{36}$$

in which J_{c0} is the zero-field J_c and B_0 is a fitting parameter (indirectly related to the upper critical field B_{c2}). It follows that

$$LnJ_c = LnJ_{c0} - \alpha B \tag{37}$$

in which $\alpha = 1/B_0$. In this model LnJ_c decreases linearly with B with slope -α; hence the J_c field dependence of a class of superconductors can be characterized in terms of a single

parameter α. This fit works well below a field B^*. The associated B_0, J_{c0}, and B^* values are given in Table 1, where a clear increase in B_0 is seen with C-additions.

Table 10 B_0, B^*, and J_{c0} values of SMI-boron strands directly doped with nominal levels of 1%C, 2%C, and 4%C.

Name	$B_0(T)$	$J_{c0}(10^6 A/cm^2)$	$B^*(T)$
B-SMI-C1%-675/20	1.6	1.6	7
B-SMI-C1%-700/20	1.7	2.0	8
B-SMI-C2%-675/60-b	1.8	5.0	8
B-SMI-C2%-700/60	1.8	4.7	8
B-SMI-C4%-675/60	2.8	1.5	8
B-SMI-C4%-700/60	2.7	1.8	9

While many critical current density studies of MgB_2 have been performed, the *n*-value is less frequently reported. The results of some studies with *n*-value as a central focus were reported above. Measuring *in-situ* HTR-fabricated strands Flukiger *et al.* [135] found *n*-values of about 5 at 8 T, 4.2 K, rising to 20-30 at 4 T, 4.2 K. They noted an unspecified but non-linear variation of *n* with *B*, and that cold high pressure densification of the pre-reacted strands improved the *n*-values. Goldacker *et al.* [134], measuring both *in-situ* and *ex-situ* wires, saw an exponential field dependence, with *n*-values of 10-20 at 8 T, 4.2 K, and 20-40 at 4T, 4.2 K. Kitaguchi *et al.* [148], measuring *in-situ* processed strands, obtained *n*-values of 17 at 10 T, 4.2 K, values which increased to 27 with SiC doping additions. Suo [149] *et al.*, achieved *n*-values of 15-30 at 8 T, 4.2K, and above 60 at 4T, 4.2 K. Martinez [150] using magnetization measurements to extract *n*-values, found an empirical relationship between *n*-value and J_c. Similar correlation of *n*-value and J_c were seen in the work of Kim *et al.* [151], among samples where values of about 30 were seen at 8T, 4.2K. It should be noted that all of these studies were performed on short samples,

and for that reason we might expect that they would be less susceptible to extrinsic limitations of *n* value. As a limit, the intrinsic *n*-value is determined by the pinning potential [153,197,198,201-203]. In any case, shorter samples should be less susceptible to the extrinsic *n*-variations brought on by I_c variations.

As stated above the present transport J_c measurements were performed on ITER barrels wound with 1.5 m lengths of MgB_2 wire; *n*-values were obtained from the accompanying voltage-current data within the electric field range of 0.4 μV/cm to 4 μV/cm. The 5 T and 10 T results for the strands are presented in Table 9. The J_c results for the strands with various SMI-C doped starting powders shown in Figure 48 are complemented by the *n*-values shown in Figure 49. Here are displayed several different behaviors of *n* as functions of field. For some samples the *n* vs *B* curve is nearly flat, while for others *n* increases with field. It seems that samples with higher C content may have a better *n*-value at high fields. It appears that some mixture of intrinsic and extrinsic contributions to *n*-value may be present.

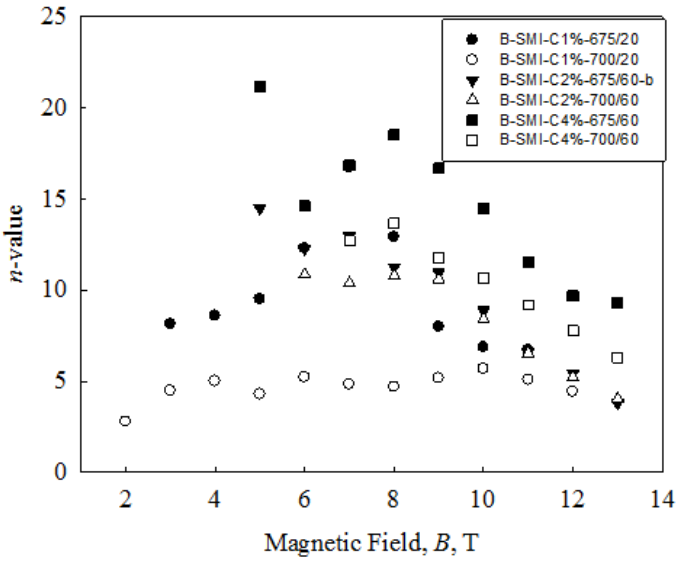

Figure 49 *n*-value vs. *B* for SMI-boron strands directly doped with nominal levels of 1%C, 2%C, and 4%C [192].

In order to make more general use of this data, it is useful to rearrange equation (28) into the form:

$$E = E_c\left(\frac{J}{J_c}\right)^n \tag{38}$$

This allows the curvature of the *I-V* curve to be described, where E_c is a given electric field criterion, J_c is the J for that criterion, and E and J are the electric field and current density. If we chose to use a different criterion E_c', say

$$E = E_c'\left(\frac{J}{J'_c}\right)^n \tag{39}$$

Then

$$\frac{J_c'}{J_c} = \left(\frac{E_c'}{E_c}\right)^{1/n} \tag{40}$$

Using this expression, it is possible to predict the value of J_c associated with a new electric field criterion given the J_c at one criterion and the associated index number.

Consider now two strands with different *n*-values but which are otherwise identical. Let one of the strands have an infinite *n*-value. This strand will transition to the normal state with infinite sharpness, at a current density we can define as J_∞. If we let the second strand have some finite *n*-value, then the J_c of this strand using the same electric field criterion E_c will be lower than the first. Let us consider the condition of this strand at $J = J_\infty$. Here the electric field will be that of the wire at the transition to the normal state, which we can take to be $E_{m.}$, Equation (39) then becomes:

$$\frac{E_m}{E_c} = \left(\frac{J_\infty}{J_c}\right)^n \tag{41}$$

which can be re-written:

$$J_c = J_\infty \frac{1}{\left(\frac{E_m}{E_c}\right)^{1/n}} \tag{42}$$

or alternatively:

$$LnJ_c = LnJ_\infty - \frac{1}{n} Ln\left(\frac{E_m}{E_c}\right) \tag{43}$$

i.e.:

$$LnJ_c = A - \frac{1}{n} D \tag{44}$$

Where A and D are constants. Equations (43) and (44) indicate that for a given strand, all other factors being equal (including the intrinsic J_c, J_∞), as n decreases so does J_c, which explains the observation in the literature [149-151].

3.5 Transport Properties of Malic-Acid-Doped MgB_2 PIT Multifilamentary Wires Made Using Two Boron Types

The two B-powder types used by HTR in the fabrication of malic-acid-doped strands were Tangshan B (TsB) and plasma spray powders (SMI). Two plasma spray powders were used, one with no C added during the plasma spray process (A-SMI-Malic2%)-1F), and one with 1% C added during plasma spray (B*-SMI-C1%-Malic2%). In both cases 2% malic acid was added, see in Table 11. Here the 2%malic refers to a nominal mol.% of malic in the final MgB_2 compound, and the C1% associated with the SMI powder name refers to a nominal molar addition of C to the B in the gas stream. However, the actual mol. % of C relative to the final MgB_2 compound is listed for all strands in column 3 of Table 11. Carbon levels for all distinct mixtures of SMI C-doped powder and malic acid doped powder have been confirmed by C-analysis performed by LECO Corporation. We note that this C analysis only measures the total amount of C present in the sample, and does not claim to be the level to which the C has entered the B sublattice. The two SMI strands had 0.8mol%C (A-SMI-Malic2%-1F) and 1.7mol% C (B*-SMI-C1%-Malic2%), respectively. Also included in this comparison were two strands

with 4.77 mol% malic acid doped TsB boron (leading to a final C content of 1.6 mol% in the MgB_2), an 18 stack Type (b) with Nb barriers and an 18 stack Type (g) with Fe barriers, i.e. Type (b) and (g) of Figure 33.

Table 11 Specifications of malic acid doped wires

Name	Tracer No	Actual C (mol %)[c]	Chemical Barrier	Sheath	Fil. Count	HT (C°/min)	%SC	OD (mm)
SMI Boron Samples								
A-SMI-Malic2%-1F-700/20[a]	1980	0.8%	Nb	M	1	700/20	16	0.834
B*-SMI-C1%-Malic2%-675/30[a]	2061	1.7%	Nb	M	18	675/30	21.3	0.834
B*-SMI-C1%-Malic2%-750/30[a]	2061	1.7%	Nb	M	18	750/30	21.3	0.834
Ts-Boron+Malic-Acid-Treated Samples								
B-TsB-Malic5%-675/60[b]	2056	1.6%	Nb	M	18	675/60	14.3	0.83
B-TsB-Malic5%-700/30[b]	2056	1.6%	Nb	M	18	700/30	14.3	0.83
G-TsB-Malic5%-Fe-NbM-675/60[b]	2017	1.6%	Fe	Nb/M	18	675/60	13.2	1.008

The J_c vs. B curves for these samples are shown in Figure 50. Table 12 lists the strands of Figure 50 in descending order of 5 T (left three columns) and 10 T (right three columns) 4.2 K J_c. The SMI B samples with 2% malic doping in addition to 1% C pre-doping (B*-SMI-C1%-Malic2%) have greater high field J_c values than does the sample with malic acid doping and non-pre-doped SMI B (A-SMI-malic2%-1F), due to greater C doping level (2x). At lower fields the C-doping is less important, although the sample with the higher HT temperature performs better. Specifically, at 4.2K the J_c of B*SMI-C1%-Malic-750/30 is about $10^5 A/cm^2$ at 5 T and more than $10^4 A/cm^2$ at 10 T. This suggests that malic acid doped SMI samples prefer higher heat treatment temperatures. The TsB-based samples, although they have a similar levels of C as the B*-SMI-C1%-malic2% samples, perform similarly to the lower C doped sample A-SMI-malic 2%-1F. This might be either because of smaller grain sizes which are known to be present for the SMI powders, or

because of a difference in the amount of C uptake into the lattice [93]. For the TsB-based samples, the best transport J_c was obtained for the higher reaction temperature. Heat treated for 30min/700 ^oC the TsB-malic strand attained a J_c of $5x10^4$ A/cm^2 at 5 T and more than 10^4 A/cm^2 at 8 T. We also note that the Fe barrier sample showed lower J_c value especially at high fields.

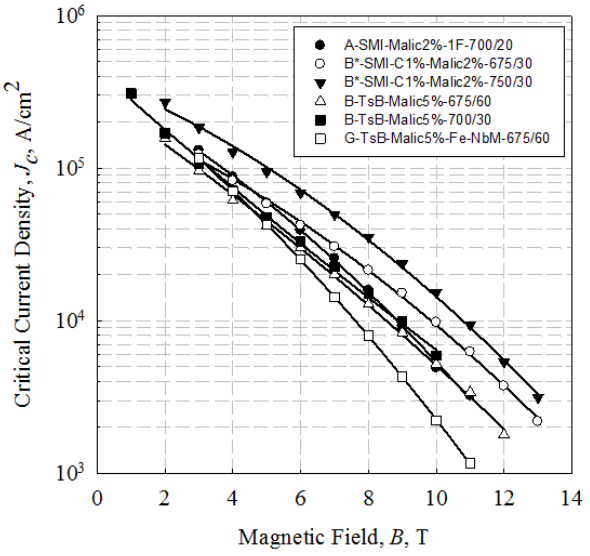

Figure 50 4.2 K transport J_C vs. B for SMI-boron strands doped with a nominal 2% malic acid and Ts-boron strands doped with a nominal 5% malic acid [192].

Table 12 4.2 K transport J_c values of SMI-boron strands doped with a nominal 2% malic acid and Ts-boron strands doped with a nominal 5% malic acid at 5T and 10T, respectively.

Name	J_c at 5T (10^4 A/cm^2)	n-value	Name	J_c at 10T (10^4 A/cm^2)	n-value
B*-SMI-Malic2%-750/30	9.6	6.7	B*-SMI-Malic2%-750/30	1.6	10.9
A-SMI-Malic2%-1F-700/20	6	5.9	B*-SMI-Malic2%-675/30	1	12.9
B*-SMI-Malic2%-675 /30	5.5	20.5	B-TsB-Malic5%-700/30	0.61	3.5
B-TsB-Malic5%-700/30	5	8.1	B-TsB-Malic5%-675/60	0.53	2.4
G-TsB-Malic5%-Fe-NbM-675/60	4.3	11.2	A-SMI-Malic2%-1F-700/20	0.5	1.9
B-TsB-Malic5%-675/60	4.2	5.1	G-TsB-Malic5%-Fe-NbM-675/60	0.23	6.5

As before the $J_c(B)$ results were fitted to Equation (37). The resulting B_0 and J_{c0} values extracted from the fit are shown in Table 13. Unlike in the the C pre-doped samples (Table 10), the B_0 values found in the malic acid doped samples do not increase monotonically with C concentration. For example, A-SMI-Malic2%-1F contained 0.8 mol.% C, much less than that of B-TsB-Malic5% (~ 1.7 mol.% C), but their B_0 values are similar. Also, the B_0 values in the SMI-B wires are insensitive to the heat treatment temperatures, while the values of B_0 in the Ts-B wires drops about 45 % (from 2.3 T to 1.6 T) by increasing the heat treatment temperature from 675 °C to 700 °C. The reason behind these observation is that SMI-B is amorphous and nano-size powder, while TS-B is crystalline and micronized powders, causing the malic acid doping in the Ts-B wires is less effective.

Table 13 B_0, B^*, and J_{c0} values of SMI-boron strands doped with a nominal 2% malic acid and Ts-boron strands doped with a nominal 5% malic acid.

Name	$B_0(T)$	$J_{c0}(10^6 A/cm^2)$	$B^*(T)$
A-SMI-Malic2%-1F-700/20	1.9±0.05	1.1	6±0.2
B*-SMI-Malic2%-675/30	2.1±0.06	1.2	8±0.3
B*-SMI-Malic2%-750/30	2.0±0.04	2.4	8±0.2
B-TsB-Malic5%-675/60	2.3±0.04	0.4	5±0.1
B-TsB-Malic5%-700/30	1.6±0.05	1.1	3±0.2
G-TsB-Malic5%-Fe-NbM-675/60	1.6±0.03	1.1	5±0.4

3.6 Mechanical Bending Induced Degradation in C Doped MgB_2 Wires

In addition to satisfactory current transport properties (J_c and n-value), the ability of a strand, and indeed a conductor assembled from it, to withstand bending strain is of interest for applications. It is of course possible to construct magnets using a wind-and-react technique, in which case bending strain is not a consideration, but insulation and the heat treatment of the coil former become issues. Magnets can also be constructed using a react-and-wind approach, which allows more flexibility in insulation, but requires that the strands be tolerant to post reaction bending during magnet winding. This type of strain is distinct from that experienced by the strand during magnet excitation in which case well-defined tensile, compressive, or transverse pressure induced strains will be applied at the operating temperature (4-30 K for MgB_2). Such effects, resulting for example from thermal cycling stresses and Lorentz forces generated in MgB_2 strands during magnet operation have been investigated [160-164]. This section focuses on the effect of bending strain applied to reacted strands at room temperature, the relevant condition for developing magnet winding procedures, cabling, and the spooling and re-spooling of reacted strands.

Table 14 Specifications and properties of the strands for mechanical tests

Name	Fil.#	Chemical Barrier	Outer sheath	Central filament	B source	Mg:B ratio	OD (mm)	% SC	J_c(4.2K,5T) 10^5 A/cm^2
PIT-36	36	Nb	Monel®	Cu	2%C SMI	1:02	0.84	12.9	2
AIMI-18	18	Nb	Monel®	Nb	2%C SMI	1.37:2	0.83	28.2	2

Specifications of the two types of MgB_2 multifilamentary strands that were fabricated by HTR for bend-tolerance studies are given in Table 14. Optical images of the strand cross-sections are shown in Figure 51. The strand PIT-36 fabricated by HTR using the CTFF process had a Cu central filament and a Nb chemical barrier. The strand AIMI-18 was fabricated at HTR by a modified IMD process designated "advanced internal Mg infiltration" (AIMI) [165]. It had 18 sub-filaments, each of which made by placing a Mg rod along the axis of a B-power-filled Nb tube. These filaments, along with a central Nb filament, were bundled and placed inside a Nb/monel bi-layer tube. The composite was then drawn to an OD of 0.83 mm. Commercial Mg powder, 99%, 20-25 μm particle size, was used for the PIT strands. The amorphous 2% C pre-doped B, manufactured by Specialty Metals Inc. (50-100 nm in size) was used in PIT-36 and AIMI-18. For all strands, a heat treatment of 675 ^{o}C for 60 min under flowing Ar was applied.

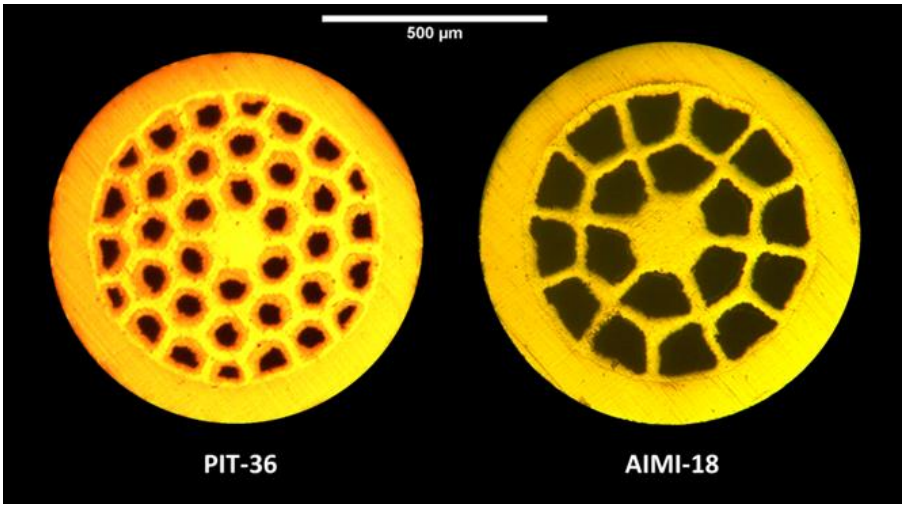

Figure 51 Optical cross-section images of PIT-36 and AIMI-18 after reaction for 675^{o}C/60min [196].

Bend-tolerance tests were performed on PIT-36 and AIMI-18 strands after HT. The strands were straight during reaction. Afterwards they were uniformly bent at room temperature, a set of arc-shape dies made with G-10 material being used to control the bending Figure 52. Assuming the neutral axis to be at the geometric center of the strands, the maximum bending strain ε_B is given by:

$$\varepsilon_B = \frac{R_W}{R_W + R_B} \tag{45}$$

where R_w is the strand radius and R_B is the radius of the G-10 die. The values of R_B and the corresponding maximal bending strains experienced by a 0.83 mm OD strand are listed in Table 15. The strand was allowed to relax mechanically, mounted onto the J_c test probe (without straightening even if deformation remained), cooled to temperature, and measured. In contrast to previous bend test measurements in which application of bending in-situ after cool down or the application of bending at room temperature and its retention during cool down [160,161,163], the present tests were designed to evaluate the tolerance of the strand to bending during react-and-wind coil fabrication or cable winding followed by operation at cryogenic temperatures.

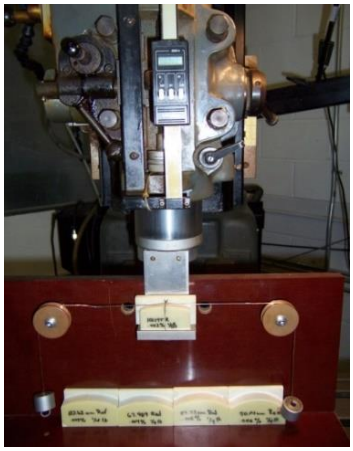

Figure 52 Apparatus used to apply a bending strain at room temperature. The wire to be bent is run between two pulleys, with weights used to apply a constant force. A shaped piece of G-10 in then raised until the bent wire lays along its whole curvature. The G10 piece is then retracted and the wire removed. (Picture was provided by Matt Rindfleisch)

Table 15 Bending radius and bending strain for a 0.8 mm OD strand.

Bending radius, R_B, mm	Maximum bending strain, %
Inf.	0
379.3	0.1
180	0.2
125.5	0.3
94.6	0.4
76.3	0.5
63.1	0.6

Figure 53 represents the 4.2 K transport $J_c(B)$s for (a) strand PIT-54 and (b) strand PIT-36. The temperature dependence of transport $J_c(B)$ for strand AIMI-18 is presented in Figure 53 (c). At 4.2 K, 5T, the J_c of PIT-36 was more than three times that of PIT-54 the increase being attributable to the effect of C doping. The 4.2 K, 5 T J_c values of PIT-36 and AIMI-18 were fortuitously about equal. However, increases in the latter's MgB_2-layer

area would lead to superior performance, as discussed in [165].

At 20 K, the non-barrier transport J_c of AIMI-18 is ≈ 10^4A/cm^2 at 5 T. Even at 25 K a transport J_c of 10^4A/cm^3 was obtained at 2 T. It is worth noting that these results for a multifilamentary AIMI strand offer promise for applications in the 20 K regime. A modified Eisterer percolation model [56] was used to fit the J_c vs B curves for various temperatures, Figure 53 (c). Figure 53 (d) displays vs the n vs B curves at various temperatures. The n-value is observed to follow Equation (30).

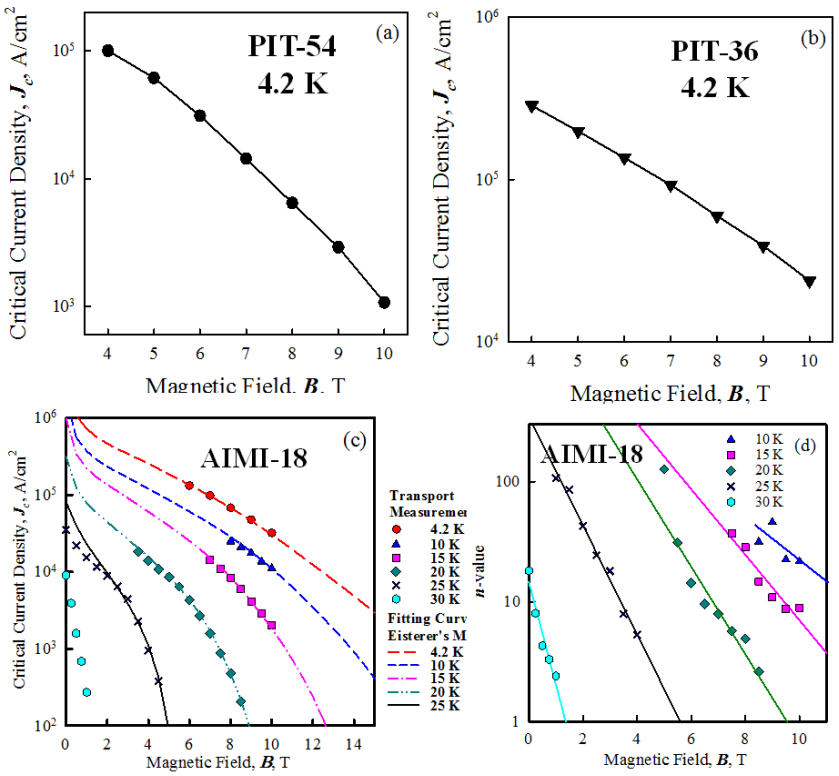

Figure 53 Transport properties of the starting strands: J_c vs B for (a) PIT-54, (b) PIT-36, and (c) AIMI-18. The n-value vs B of AIMI-18 is also represented in (d). Lines in (c) are fitting curves based on a modified percolation model for MgB_2 strands [56]. Lines in (d) are fits to $n \propto e^{-m \cdot B}$ [196].

Figure 54 shows the 4.2 K transport results for PIT-36 in response to initial bending strains of 0 to 0.4% followed by release in terms of: (a) $J_c(B)$ as function of applied field up to 10 T; (b) the relative change of $J_c(B)$ as function of bending strain, defined as $\Delta Jc(B) = \frac{J_c(B,Bend) - J_c(B,Unbend)}{J_c(B,Unbend)}$, in which $J_c(B,Bend)$ and $J_c(B,Bend)$ are the values of J_c in the bent sample and unbent control at B, respectively. Figure 54 (b) shows that bending strains of up to 0.4% have only a small influence (< 5%) on $J_c(B)$; (c) *n*-value vs bending strain at various *B* up to 10 T.

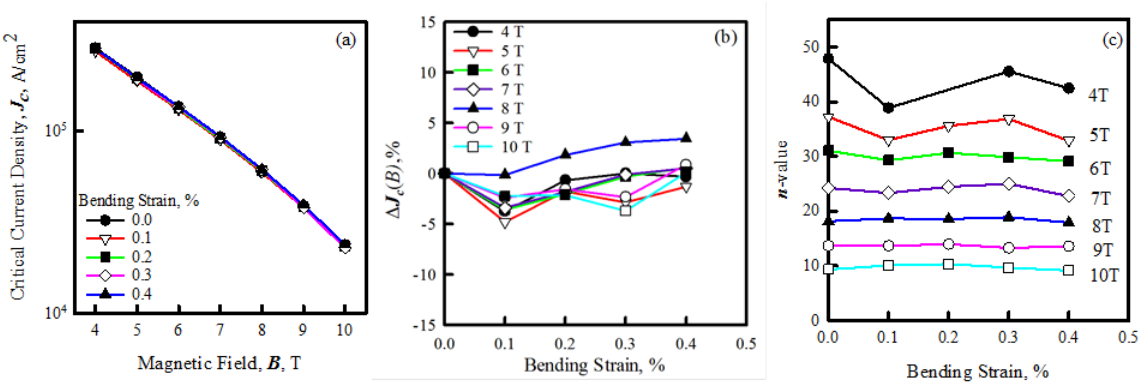

Figure 54 4.2K transport results for PIT-36 in response to bending strain plus release: (a) J_c-B behavior, (b) the relative change of $J_c(B)$ vs bending strain, and (c) *n*-value vs bending strain at various *B* [196].

Figure 55 show that this AIMI-18 exhibits measurable bending strain sensitivity, in particular: (i) Figure 55 (a) indicates a small shift in J_c(B) in response to strain; (ii) Figure 55 (b) shows ΔJ_c to be weakly bend-strain dependent. For example, at 8 T J_c rises by about 12% from 6.7 to 7.5x10^4 A/cm^2 at 0.3% strain, drops to the starting value at 0.5% strain and continues to decreases to 6.2x10^4 A/cm^2 at the equipment's bend-strain limit of 0.6%;

(iii) Figure 55 (c) depicts the strain dependence of *n*-value at selected applied fields; only in fields of 8 T and above is any approximation to a trend observable. The $J_c(B)$ is relatively unchanged at 0.1% bending strain, which is probably due to the absence of plastic deformation at this stage; an increase in J_c with a further increase of bending strain up to 0.3% indicates that the strand is becoming plastically deformed and the internal strain state of the MgB_2 filaments is starting to release; further increase in bending strain gradually decreases the $J_c(B)$ due to the breakage of MgB_2 intergrain connection. All these bending strain influences on $J_c(B)$ are field-independent. Compared to the results of PIT-36, AIMI-18 exhibits a much larger pre-strain, which cannot be completely cancelled by the negative effect from the compression portion. Nishijima [162] found the reversible tensile strain of a single-filamentary IMD strand at 4.2 K and 10 T to be 0.67%, and the value for a single-core PIT strand to be 0.54%. Kováč [163] showed the reversible tensile strain of a four-filamentary IMD strand to be 0.43% at 4.2 K and 5 T, higher than the value of four-filamentary PIT strand (0.38%). An increase in the transport performance of AIMI-type strand of up to 10% as the bending strain increased to 0.3% was followed by a monotonic decrease with further increases in strain.

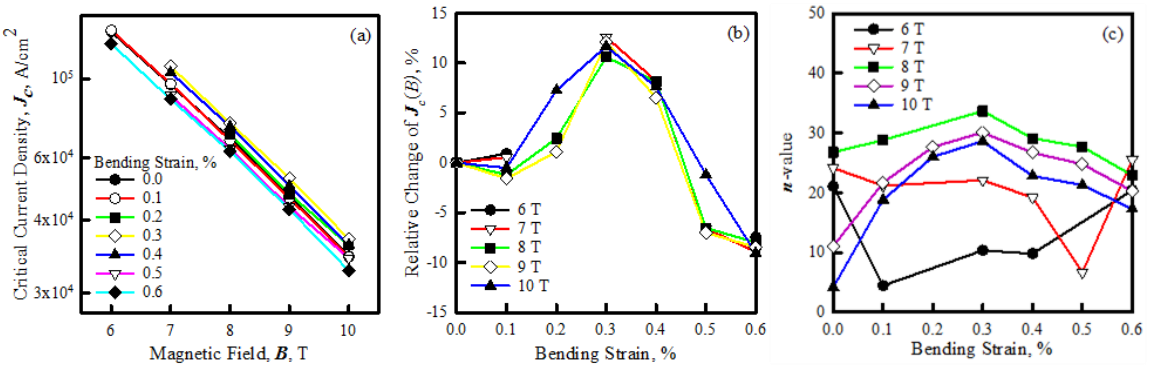

Figure 55 4.2K transport results for AIMI-18 in response to bending strain plus release: (a) J_c-B behavior, (b) the relative change of $J_c(B)$ vs bending strain, and (c) n-value vs bending strain at various B [196].

3.7 Summary of C Doping in MgB_2 Superconducting Wires

In this chapter, the influence of C doping on transport performance of MgB_2 monofilamentary wires were studied. Compared to the literature values of the previous research [11, 126, 128-137], the high field J_c, n-values and B_{c2} were enhanced by C doping in the MgB_2 wires. For example, the best 10 T J_c obtained by 3 at. % C doping was 4.4×10^4 A/cm^2 which is higher than those of [11, 126, 128-137] (~ $0.5\text{-}3.0\times10^4$ A/cm^2). However, T_c was reduced, causing C doping less effective at temperatures above 20 K; Moreover, we showed that the J_c values of the C doped MgB_2 wires at high temperatures (T > 20 K) were also reduced. Thus, C doping can only be used at low temperatures (T < 20 K). We observed that the heat treatment parameters, e.g. temperature T and duration t, played important roles in the C doping efficiency. A 4.2 K J_c of 2.3×10^4A/cm^2 was achieved by HT the 2 at. % C added MgB_2 PIT wire at a low T (625°C) for a long t (480 minutes). Moreover, the n-values

and the pinning potentials U in the undoped PIT, C doped PIT and C doped IMD samples were studied in detail by three different approaches; we showed that C doping can improve both n and U in high magnetic fields. Finally, C doping in a set of MgB_2 multifilamentary wires was investigated in terms of transport properties, doping techniques, B types, wire structure and strain tolerance with the goal of optimizing the performance of practical MgB_2 multifilamentary wires.

Chapter 4: Rare Earth Oxide Doping in MgB_2 Bulk and Wires

REO doping can improve the superconducting properties of MgB_2 (Section 1.5.3). However, the mechanism behind REO doing is still unclear. Also, most studies are focusing on REO doping in MgB_2 bulk, few research focuses on REO doping in MgB_2 wires. In this chapter, the rare earth oxides (REO) as Dy_2O_3 and Nd_2O_3 are used as additives to study their influences on MgB_2 Bulk. In doing so, two sets of REO doped MgB_2 bulk samples were fabricated and examined by XRD, SEM and TEM. Magnetization measurements at various temperatures were performed on these bulk samples. Then a series of Dy_2O_3 doped MgB_2 strands were fabricated by the CTFF method using C pre-doped B powder from SMI. The transport and magnetic critical current densities, J_{ct} and J_{cm}, were measured and compared. In-field resistivity measurements were performed on the wires. Flux pinning behaviors and Kramer irreversibility fields B_k were compared in response to Dy_2O_3 doping.

4.1 Sample Preparation and Measurements

Both bulk (B) and wire (W) samples were prepared for measurement. Three traditional bulk samples were fabricated: (i) pure MgB_2 bulk **B-00** made by mixing Mg powder (99%, < 44μm particle size) and B powder (99%, from Alfar Aesar) according to the molar ratio of Mg:B=1.1:2; (ii) Dy_2O_3 added bulk **B-DY** made by adding 0.5 wt.% Dy_2O_3 powder (>99.9%, <100 nm particle size, ALDRICH); and (iii) Nd_2O_3 added bulk **B-ND** made by using 0.5 wt.% Nd_2O_3 powder (>99.9%, <100 nm particle size, Aldrich). After 1-hour grinding in a mortar, the mixtures were uniaxially pressed into ~ 4 mm tall by ~ 8 mm diameter pellets, encapsulated in quartz tubing, and heat treated in an Ar atmosphere at 700 °C for 30 minutes.

Monofilamentary wires, manufactured by the CTFF process [126], were provided by Hyper Tech Research Inc. (HTR). The strands which were 0.83 mm in diameter included thick chemical barriers of Nb and outer sheaths of monel. Commercial Mg powder (99%, < 44 μm particle size) and 2 at. % C pre-doped SMI boron from Specialty Metals Inc. (SMI) were used [92]. Three strands were fabricated: (i) with no Dy_2O_3 additions, labeled as **W-00**; (ii) with 0.5 wt.% Dy_2O_3 nano-powder added MgB_2 strands which were labeled as **W-DY**; and (iii) with 2.5 wt.% Dy_2O_3 nano-powder added MgB_2 strands which were labeled **W-DY-02**. Sample information is listed in Table 16.

Table 16 Doping additions amount and heat treatments for undoped and REO doped MgB_2 bulk samples (B) and wires (W).

Sample	Dopant additions	HTs
B-00	None	700ºC, 30min
B-DY	0.5wt%Dy_2O_3	700ºC, 30min
B-ND	0.5wt%Nd_2O_3	700ºC, 30min
W-00	2at. %C	650ºC, 30min
		675ºC, 30min
		700ºC, 30min
W-DY	2at%.C+0.5wt%Dy_2O_3	650ºC, 30min
		675ºC, 30min
		700ºC, 30min
W-DY-02	2at. %C+2.5wt%Dy_2O_3	675ºC, 30min

XRD analysis, SEM, TEM and EDS were performed on equipment described in Section 2.4 and 2.5. TEM samples of **B-DY** and **B-ND** were prepared by grinding the specimens into a fine powder for ~10-20 min in an agate mortar and pestle. A small amount (< 1 mg) of the ground powder was placed into a glass vial and mixed with isopropanol. The powder/isopropanol mixture was ultrasonicated to create a uniform dispersion of MgB_2 particulates. A small quantity of this dispersion was pipetted out and dripped onto a lacey carbon TEM grid where it was allowed to dry.

Transport measurements were performed on all strands at 4.2K in pool-boiling liquid helium in transverse magnetic fields ranging from 0T to 13T. Strands were prepared in the form of "short samples" (3 cm in length) with a gauge length of 5 mm. Magnetic properties were measured using a Quantum Design Model 6000 PPMS at temperature of 4.2 K to 300 K and at fields of ± 13 T. The superconducting critical transition temperature T_c and T_c-distribution were determined by DC magnetic susceptibility methods. The upper critical field B_{c2} was evaluated by resistivity measurements in transverse magnetic fields.

The B_{c2} data below 13 T were measured at The Ohio State University and those above 13 T were obtained at National High Magnetic Field Laboratory. The magnetization measurements were performed on all the bulk samples polished into a cuboid shape, as well as all the wire samples. The magnetic critical current density J_{cm}, Kramer irreversible field B_k and the bulk pinning force density F_p were extracted from the magnetization results at various temperatures.

4.2 REO Doping in MgB_2 Bulk

4.2.1 Influence of REO Doping in XRD Results and Lattice Constants of MgB_2 Bulk

The X-ray diffraction data for the three bulk samples are presented in Figure 56 where the Bragg reflections are indexed for only the MgB_2 phase for simplicity. Some MgO (< 2 wt. %) and Mg (< 3 wt. %) existed in all samples. Modest levels of MgO is known both to act as a pinner, as well as in some cases reduce connectivity [205]; but any small MgO effects should be present in all samples. Given the relatively small amounts they should not strongly affect the superconducting B_{c2}, J_c, T_c, or T_c distribution of MgB_2. No peak shifting at both (110) and (002) was observed in any of the doped samples. Peaks corresponding to rare earth (RE) containing phases were observed in all the doped samples. The lattice parameters extracted from pseudo-Voigt fitting of the MgB_2 peak reflections are listed in Table 17. Both lattice parameters *a* and *c* were unchanged after adding REO,

unlike C doping in MgB_2 [97]. Therefore, it confirms that Dy_2O_3 and Nd_2O_3 did not substitute into the MgB_2 lattice at least to an extent detectable by XRD, unlike reported by other authors.

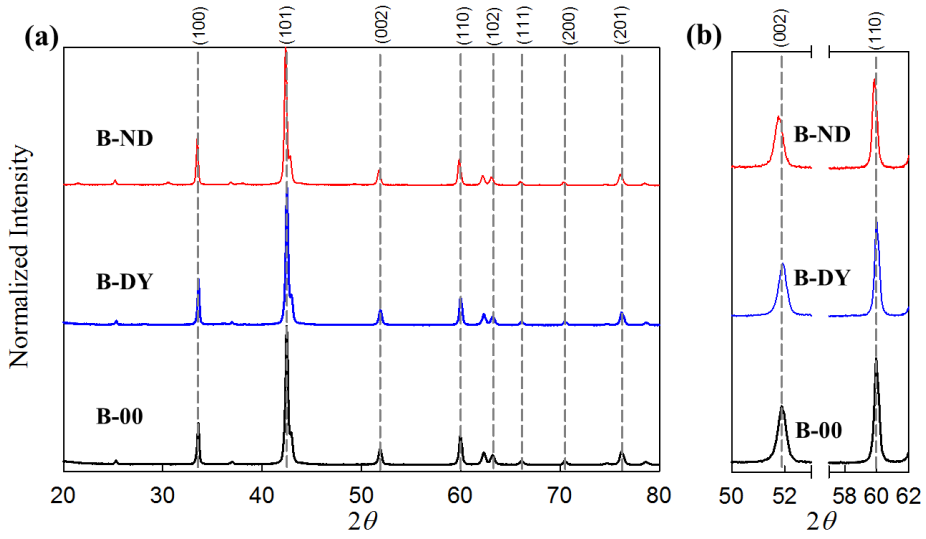

Figure 56 (a) X-ray diffraction characterization of undoped MgB_2 sample B-00, and the two REO doped samples; (b) Peaks (110) and (002), as these two peaks are directly related to lattice parameter *a* and *c*, respectively. Note for the REO doped samples, no peak shifting is observed.

Table 17 Lattice parameters and RE contained impurities in the undoped and REO doped MgB_2 bulk samples.

Sample	Dopant additions	*a* (Å)	*c* (Å)	RE contained impurities
B-00	None	3.082(8)	3.522(1)	None
B-DY	0.5wt%Dy_2O_3	3.082(3)	3.520(8)	DyB_4
B-ND	0.5wt%Nd_2O_3	3.081(9)	3.519(2)	NdB_6

4.2.2 Influence of REO Doping on the Microstructures of MgB_2 Bulk

The results based on fracture secondary electron (SE) images by 'through the lens' (TTL) detection of the REO doped bulk samples are presented in Figure 57(a) – 2(c). Most of the grains in these three traditional bulk samples had a hexagonal plate-like shape interspersed with small spherical grains located in micro-voids between them. The size of these hexagonal plate-like MgB_2 grains (confirmed by EDS analysis) was expressed in terms of an average diameter, *D*, according to:

$$D = \frac{2\sum\sqrt{A_i/\pi}}{N} \tag{46}$$

where *N* is the total number of grains in the examined area (in order to maintain statistically accurate, N > 30), A_i is the area of the i^{th} grain. The values of *D* for the bulk samples are listed Table 18. Compared to the undoped MgB_2 bulk B-00, the hexagonal plate-like MgB_2 grains were significantly smaller in the REO doped samples.

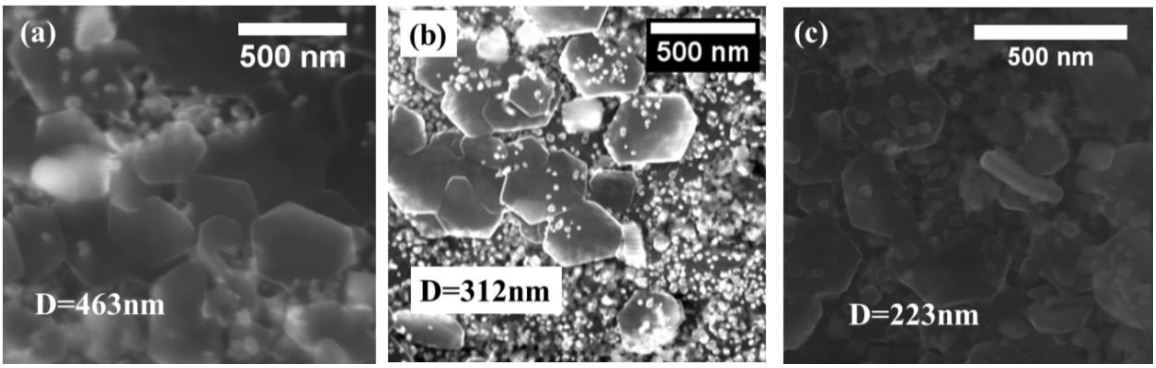

Figure 57 (a) Secondary electron imaging (SE) by through-the-lens detection (TLD) on a fractured surface of B-00. Some MgB_2 grains are dimensioned; (b) a fractured surface of B-DY; (c) a fractured surface of B-ND. Note that the grain size in the undoped sample B-00 is much larger than those in the REO doped samples.

Table 18 Grain sizes for undoped and REO doped MgB_2 bulk samples

Sample	Dopant additions	*D* (nm)
B-00	None	463(5)
B-DY	0.5wt%Dy_2O_3	312(6)
B-ND	0.5wt%Nd_2O_3	223(5)

Figure 58 (a) and (b) and Figure 58 (c) and (d) represent the bright-field TEM images obtained from fine powders of **B-DY** and **B-ND**, respectively. Nano-size inclusions about ~20 - 50 nm were observed inside the MgB_2 grains and some larger inclusions (> 50 nm) were found outside them. The in-grain nano-inclusions can act as new pinning sites and enhance flux pinning in MgB_2, while the nano-inclusions found at MgB_2 grain boundaries possibly worked as grain growth inhibitors to prevent grain coarsening. This observation supports the grain refinement noted in the both Dy_2O_3 and Nd_2O_3 doped bulk, Table 18. It is hard to perform direct EDS analysis on these nano-size particles as they were too small. Even though, based on the XRD results, these nano-size particles were likely to be DyB_4 in B-DY and NdB_6 in B-ND, respectively.

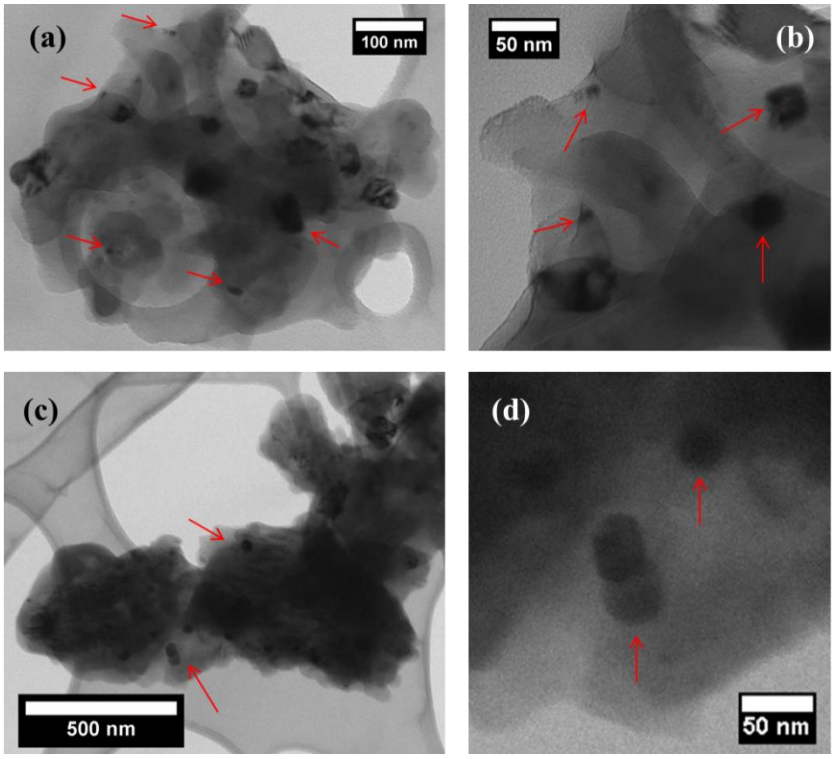

Figure 58 Bright-field (BF) TEM imaging of (a) an agglomeration contained grains of B-DY; (b) nano-size inclusions inside MgB_2 grains of B-DY; (c) an agglomeration contained grains of B-ND; (d) nano-size inclusions inside MgB_2 grains of B-ND.

4.2.3 Influence of REO Doping in Superconducting Transition Temperature T_c and T_c Distribution in MgB_2 Bulk

The T_c and T_c distributions of the three bulk samples were obtained by magnetization measurement, Figure 59. The T_c was defined as the onset of superconductivity from the normal state at 10 mT and the T_c distribution was expressed in terms of $d\chi/dT$, where χ is the DC susceptibility.

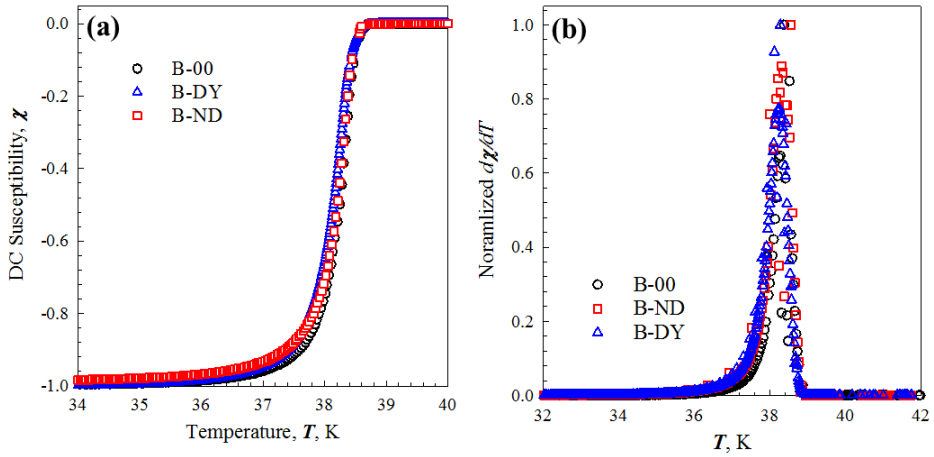

Figure 59 (a) DC susceptibility χ vs. T at 0.01 T and (b) the T_c distribution - dχ/dT vs. T for the undoped bulk sample B-00 and the doped bulk sample B-DY and B-ND.

Table 19 T_c and FWHM of MgB_2 bulk samples

Sample	Onset T_c (K)	FWHM of T_c (K)
B-00	39.2(2)	0.4(1)
B-DY	39.2(2)	0.5(1)
B-ND	39.2(2)	0.4(1)

The onset T_c and the full-widths at half maximum (FWHM) of all samples are listed in Table 19. The undoped sample B-00 shows a sharp superconducting transition with T_c of 39.2 K and a FWHM of ~ 0.4 K. The T_c did not change after adding Dy_2O_3 and Nd_2O_3. Unlike substitutional doping with Al [94,103-109] or C [91,93,94,96-98] which cause notable changes of T_c, our REO doping did not alter the T_c and T_c distribution of MgB_2 within measurement error. Again, these observations suggest that Dy_2O_3 and Nd_2O_3 doping did not result in elemental substitution for Mg or B atoms during reaction.

4.2.4 Influence of REO Doping on the Upper Critical Fields B_{c2} of MgB_2 Bulk

The T dependencies of the resistively measured B_{c2} of the three bulk samples are presented in Figure 60. It is clear that REO doping had no effect on the B_{c2} values within error. For example, a B_{c2}(20 K) of ~6.5 ± 0.2 T includes both the undoped sample (B-00) and the doped bulk (B-DY and B-ND). The unchanged B_{c2} of these REO added samples are expected and consistent with the XRD results and T_c.

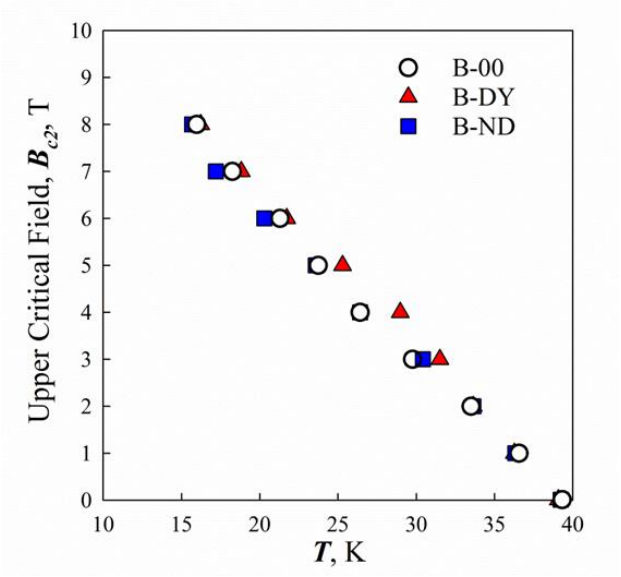

Figure 60 The temperature dependency of B_{c2} for the undoped bulk sample B-00 and the doped bulk sample B-DY and B-ND.

4.2.5 Influences of REO Doping on Critical Current Density, Irreversibility Field, and Flux Pinning of MgB_2 Bulk

The magnetic critical current densities (J_{cm}) of the bulk samples were calculated based on Bean's critical state model:

$$J_{cm} = \frac{3\Delta M}{b(1 - b/3a)} \tag{47}$$

where ΔM is the width of the hysteresis loop at a given field, a is the length of the sample's longer edge and b that of its shorter edge. Both a and b are orthogonal to B. The J_{cm} values vs. B at 10 K are plotted in Figure 61 (a). It is clear that the J_{cm}s were increased by doping in all measured fields. The irreversibility field, B_k, and the bulk pinning force density, F_p, of the MgB_2 bulk are listed in Table 20. B_k was deduced from the cross-intercepts of linear fittings to Kramer plots (inset in Figure 61 (a)). F_p ($F_P = J_{cm} \times B$) is plotted against normalized magnetic field $b = B/B_k$ in Figure 61 (b), B_k did not increase in response to REO doping (Table 20). Increases in $F_{p,max}$ were achieved in response to Dy_2O_3 and Nd_2O_3 doping. For example, at 10 K, $F_{p,max}$ increased from 0.49 GN/m^3 for the undoped bulk to 0.66 GN/m^3 and 0.93 GN/m^3 after adding Dy_2O_3 and Nd_2O_3, respectively. Since MgB_2 grain refinement was observed in REO doped bulk, we conclude that the flux pinning enhancement is driven by grain size reduction. We noticed that $F_{p,max}$ is proportional to the reciprocal of D:

$$F_{p,max} \propto \frac{1}{D} \tag{48}$$

Figure 61 (c) shows this to be the case for the bulk samples. Our data fit equation (48) well indicating that the grain refinement observed in these REO doped samples is responsible for the enhancement of flux pinning.

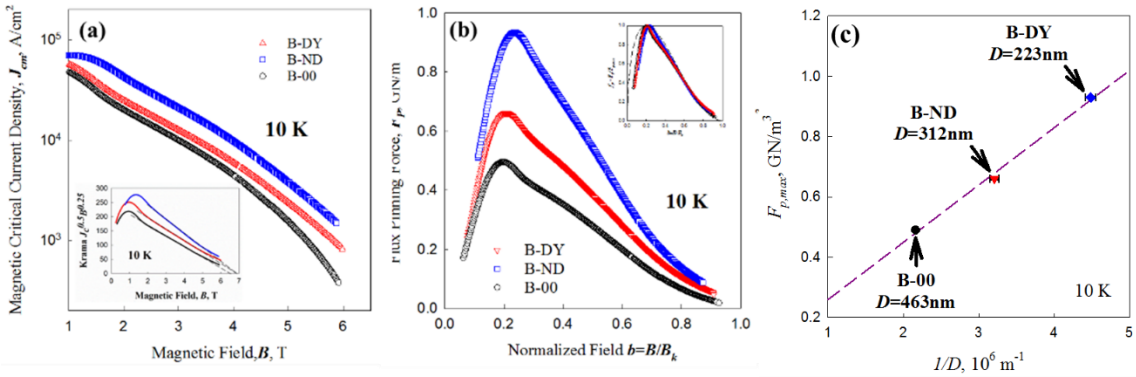

Figure 61 (a) Magnetic critical current density J_{cm} vs. B (Inset is Kramer plot $J_c^{0.5}B^{0.25}$ vs. B); (b) the flux pinning density F_p vs. b (Inset is f_p vs. b where $f_p = F_p/F_{p,max}$); and (c) $F_{p,max}$ vs. $1/D$ (dash line is the linear fitting) for B-00, B-DY and B-ND.

Table 20 B_k and flux pinning properties of the MgB_2 bulk.

Sample	B_k (T)			b_{peak} at 10 K	$F_{p,max}$ (GN/m^3) at 10 K	$1/D$ ($\times 10^6$ m^{-1})
	4.2 K	10 K	15 K			
B-00	7.7(1)	6.6(1)	5.6(1)	0.20(1)	0.49	2.16(2)
B-DY	7.9(1)	6.9(1)	5.9(1)	0.21(1)	0.66	3.21(6)
B-ND	7.8(1)	6.9(1)	5.9(1)	0.23(2)	0.93	4.48(7)

4.3 Influence of Rare Earth Oxide Doping in MgB_2 PIT Wires

4.3.1 Influence of Dy_2O_3 Doping on the Microstructure and Grain Size in MgB_2 wires

The microstructures of W-00 and W-DY HT at various temperatures were revealed by fracture secondary electron (SE) imaging, Figure 62. In order to make sure that our results were statistically accurate, the MgB_2 grain sizes were evaluated over a 3 μm × 3

μm area on the fractured surfaces of all wires (described in Section 4.2.2). For the undoped wire W-00, HT at 650 °C most of the MgB_2 was in a form of loosely interconnected fine spherical grains with a size of ~55(3) nm, most of which were loosely connected to each other, Figure 62 (a). As the HT temperature increased to 675 °C most of the MgB_2 grains coarsened and transformed into hexagonal plate-like grains 134(3) nm, Figure 62 (b). The intergranular connection strongly improved though some nano-size voids could still be observed. With further increase of HT temperature to 700 °C, most of the MgB_2 grains continued to convert into coarse and well-connected hexagonal plate-like grains and their average size increased to 215(4) nm, Figure 62 (c).

For the Dy_2O_3 doped wire W-DY, HT at 650 °C, spherical fine grains with a size of 59(2) nm were formed, Figure 62 (d). However, at 675 °C coarse plate-like MgB_2 grains 99(4) nm existed in the MgB_2 layers while the spherical fine grains could still be observed, Figure 62 (e). With further increase in HT temperature to 700 °C, the thickness of the MgB_2 layers formed by coarse grains 151(5) nm increased to ~ 2 μm and all the spherical fine grains transformed into hexagonal plate-like MgB_2 grains which were still smaller than those in the MgB_2 layers, Figure 62 (f). Comparing these results to those of the wire without the Dy_2O_3 addition, we conclude that Dy_2O_3 inhibits MgB_2 grain growth, restricting the grain size. These observations in W-DY were consistent with those observed in B-DY. For example, a grain size reduction of about 35% was achieved in the Dy_2O_3 doped wire and a reduction of about 40% in the Dy_2O_3 doped bulk. This result suggests that even through the bulk and wires were processed using different sources of B (crystalline micro-size B in

the bulk samples vs. C doped amorphous nano-size B in the wires) grain refinement by doping with Dy_2O_3 was still observed.

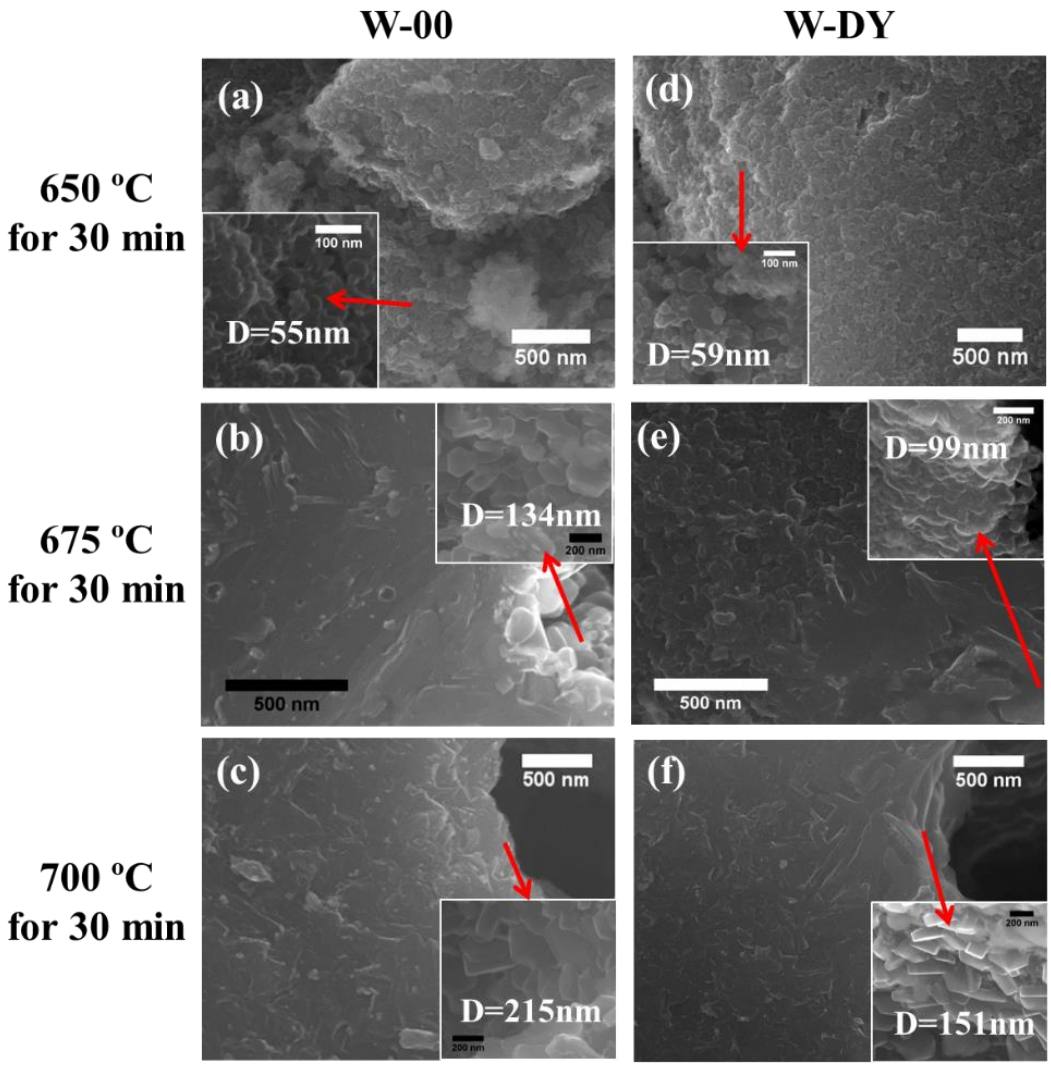

Figure 62 Secondary electron imaging (SE) by through-the-lens detection (TLD) on fractured surfaces: (a) – (c) W-00 and (d) - (f) W-DY. Three heat treatments were included: (a) (d) 650 °C for 30 min; (b) (e) 675 °C for 30 min; and (c) (f) 700 °C for 30 min. Insets are enlarged SEM images.

4.3.2 Influence of Dy_2O_3 Doping on Transport and Magnetic Critical Current Densities

The transport J_{ct} vs. B of all wires HT at 675 °C at 4.2 K is plotted in Figure 63. Results of an undoped MgB_2 wire from [93] were plotted for comparison. This wire was fabricated by the same process and materials except that undoped SMI boron was used. Compared to the undoped MgB_2 wire, the C doped sample W-00 showed much better transport performance, especially at higher fields (> 6 T). Moreover, J_{ct} was further improved by co-doping with Dy_2O_3. The best J_{ct} was obtained in the 0.5 wt.% Dy_2O_3 added wire W-DY. At 10T and 12 T, its J_{ct} values were about 3.0×10^4 A/cm^2 and 1.7×10^4 A/cm^2, which are about three times and four times, respectively, those of the C doped sample W-00. After increasing the Dy_2O_3 concentration to 2.5 wt.%, J_{ct} was reduced. Even so, its J_{ct} at 12 T was still about two and half times as high as that of W-00. This transport performance of these Dy_2O_3 added wires augurs well for applications in the 4.2 K high-field regime.

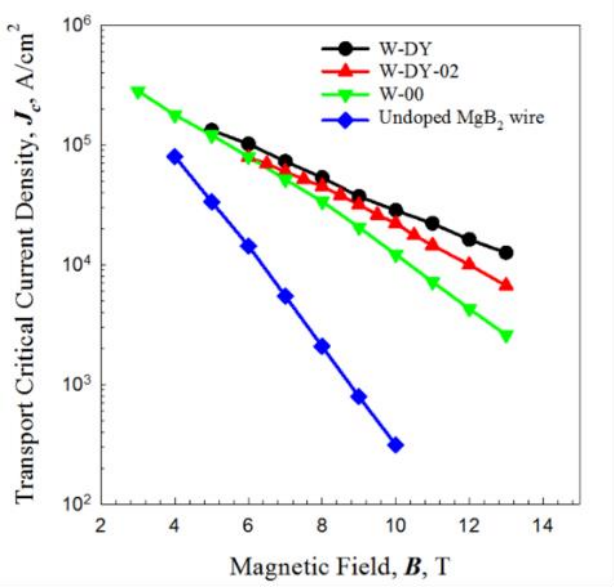

Figure 63 Transport critical current density at 4.2 K for the Dy_2O_3 added wire W-DY and the control W-00. The results of an undoped MgB_2 wire (blue square) from [93] are plotted for comparison.

Figure 64 shows the magnetic J_{cm} vs. B of selected wires at various temperatures calculated according to:

$$J_{cm}=\frac{3\pi\Delta M}{4d} \tag{49}$$

where ΔM is the width of the hysteresis loop at a given B, and d is the OD of superconducting core of the wires. As expected from the transport results (Figure 63), Dy_2O_3 increases the J_{cm} of MgB_2 wires. For example, at 4.2 K the 12 T J_{cm}s values were 1.3×10^5 A/cm^2 and 1.0×10^5 A/cm^2 in W-DY and W-00, respectively. This J_{cm} increase is larger at higher temperatures. For instance, at 20 K, the 3 T J_{cm} of W-DY was 6.5×10^4 A/cm^2, about twice of that of W-00 (~3.2×10^4 A/cm^2).

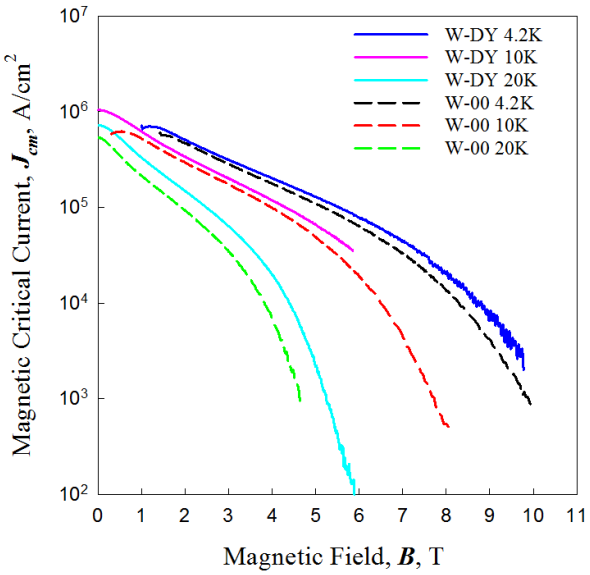

Figure 64 Magnetic critical current density J_{cm} vs. B of for the Dy_2O_3 added wire W-DY and the control W-00.

4.3.3 Influence of Dy_2O_3 Doping on Irreversibility Field and Flux Pinning Behavior

The field dependency of the bulk flux pinning force density F_p with respect to the normalized field $b=B/B_k$ is presented in Figure 65 (a). The irreversibility fields B_k extracted from Kramer plots are listed in Table 21. Similar to the results of REO doped bulk, B_k shows small increases with doping at all temperatures (4.2 – 20 K). $F_{p,max}$ as shown in the table increased with doping. For example, $F_{p,max}$ at 20 K increased by more than 50% (from 2.2 GN/m^3 to 3.3 GN/m^3) in response to the addition of 0.5 wt.% Dy_2O_3. Figure 65 (b) shows the field dependency of $f_P = F_p/F_{p,max}$ along with the grain boundary (GB) pinning curve based on from Dew-Hughes [65]. Clearly GB pinning is dominant in both the Dy_2O_3

added wire W-DY and the control wire W-00 at all temperatures. The GB pinning dominant behavior of Dy_2O_3 doped wire is similar to that observed in the bulk samples, Figure 61.

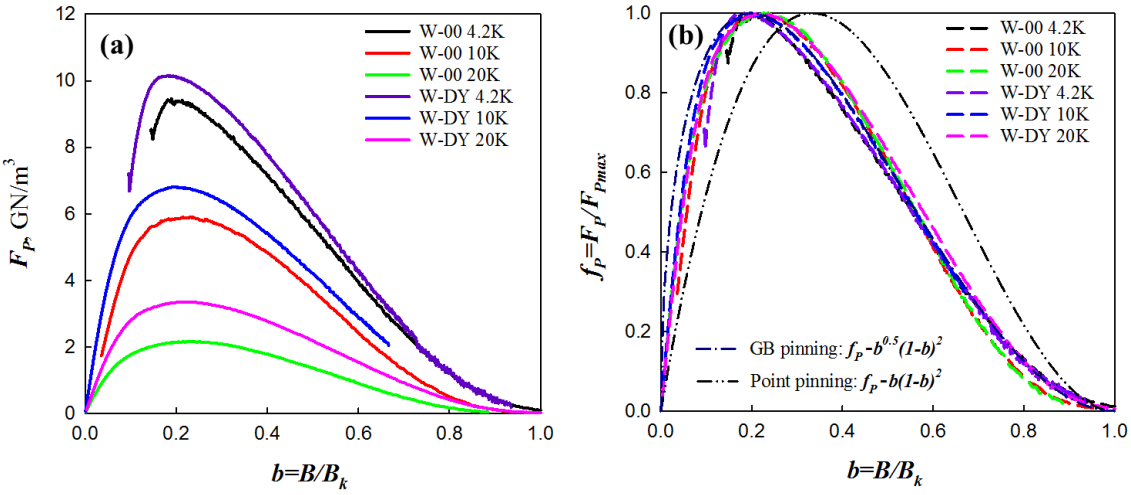

Figure 65 (a) the flux pinning density F_p vs. B; and (b) normalized flux pinning behavior f_p vs. b of for the Dy_2O_3 added wire W-DY and the control W-00.

Table 21 Superconducting properties of MgB_2 wires

Sample	J_{ct} at 12 T and 4.2 K	B_k (T)			$F_{p,max}$ (GN/m^3)			*1/D* (×10^7 m^{-1})
	(A/cm^2)	4.2 K	10 K	20 K	4.2 K	10 K	20 K	
W-00	4.2×10^3	9.9(1)	8.0(1)	5.1(1)	9.34	5.9	2.19	0.74(1)
W-DY	1.7×10^4	10.4(1)	8.7(1)	5.5(1)	10.11	6.83	3.37	1.01(1)
W-DY-02	1.1×10^4	-	-	-	-	-	-	-

4.3.4 Influence of Dy_2O_3 Doping on the Upper Critical Field B_{c2}

Resistively measured B_{c2} is plotted in Figure 66 which includes results for the undoped MgB_2 wire from [93] for comparison. The figure shows that the addition of 0.5 wt.% Dy_2O_3 to wire sample W-00 produces no change in B_{c2}. The same result was also observed in the bulk (Figure 60). This and the absence of XRD peak shift (Figure 56 and Table 17) and changes in T_c (Table 19) indicate that REO dopants do not alloy with MgB_2 during the formation reaction. We conclude by noting that the large increase in B_{c2} from that of undoped wire to those of W-00 and W-DY is due to the pre-doping of the latter by 2 at. % C. The improvement of J_c in response to Dy_2O_3 doping is of course a result of grain size reduction.

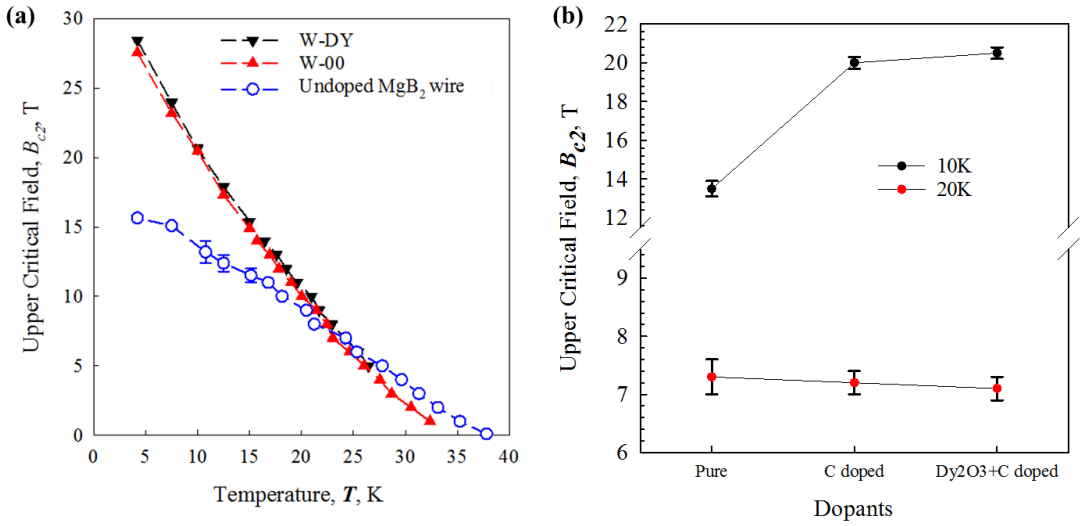

Figure 66 (a) The temperature dependency of upper critical field B_{c2} for W-DY and W-00. The values over 13 T were obtained from National High Magnetic Field Laboratory. The results of an undoped MgB_2 wire (blue circle) from [93] are also plotted for comparison. (b) The B_{c2} vs. Dopant types at 10 K and 20 K. The B_{c2} values were extracted by the linear fittings of the B_{c2} vs. T curves in (a).

4.3.5 Final Note on Flux Pinning and Grain Size in REO doped MgB_2 Bulk and Wires

In this section we discuss the relationship between $F_{p,max}$ and grain size for bulk (B) and wires (W) based on Equation (43), $F_p \alpha 1/D$. Instead of the proportionality we introduce a factor p such that $p = F_{p,max} \cdot D$, Table 22. As shown in Figure 67, $F_{p,max}$ vs. $1/D$ produces two lines, one of slope p_B (for the bulk prepared using pure B powder) and the other of slope p_W (for wire based on 2 at. % pre-doped SMI B). The ratio of the slopes, p_W/p_B =3.44, is attributed to the effect of C substitution on B_{c2} and the Ginzburg-Landau (GL) parameter, κ.

As shown by Dew-Hughes [65] and Kramer [63], in response to normal surface pinning (e.g. grain-boundary, GB pinning), the bulk pinning force density, F_p, vs. normalized field b maximizes at $b = 0.2$ according to:

$$F_p = 3.494 F_{p,max} b^{1/2} (1-b)^2 \quad (50)$$

in which, according to Ref [63]:

$$F_{p,max} = C_s B_{c2}^{2.5} / \kappa^2 \quad (51)$$

in which C_s is a microstructure-dependent parameter. As indicated above C_s under GB pinning will be proportional to $1/D$ and hence:

$$p \alpha B_{c2}^{2.5} / \kappa^2 \quad (52)$$

Using the B_{c2} values from Table 22 and equating p_W/p_B based on equation (52) to the above experimentally obtained 3.44 we find $\kappa_W/\kappa_B = 1.32$. This 24% increase in the GL parameter

we attribute to scattering by the C doping. A comparable increase of $\kappa = B_{c2}/2^{1/2}B_c$ in response to C doping can be deduced with the aid of B_c data published by Mudgel *et al.* [173] who reported that for 0 and 4 at. % C doping, B_c(0%C, 0K)/ B_c(4%C, 0K)= 15.7 T/23.2 T = 0.68. Combining this with the B_{c2} data of Table 22 it follows that $\kappa_W/\kappa_B \sim 1.39$, which is consistent with our results.

Table 22 Assembled Data from Section 4.2.1 to 4.3.4

Sample	$F_{p,max}$,10K, GN/m^3	B_{c2}, 10K T	D, nm	p, N/m^2	<p>, nm
B-00	0.49	10	463	227	**213**
B-DY	0.66	10	312	206	
B-ND	0.93	10	223	207	
W-00	5.9	20.5	134	790	**733**
W-DY	6.83	20.5	99	676	

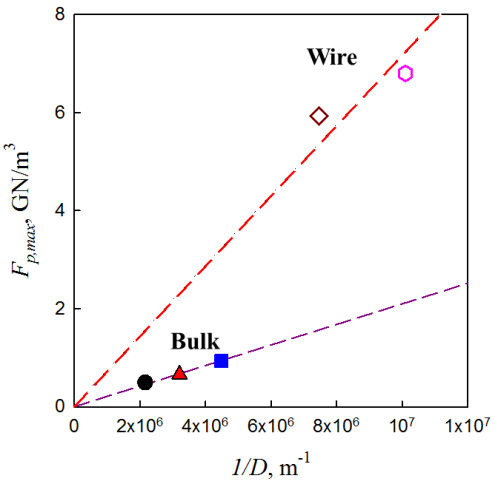

Figure 67 $F_{p,max}$ vs. *1/D* of the bulk samples (filled symbols) and wires (unfilled symbols). Dash lines are linear fitting of the data.

4.4 Summary of REO Doping in MgB_2

The effects of REO (Dy_2O_3 and Nd_2O_3) doping in MgB_2 were studied in both bulk samples and wires. Their microstructures and superconducting properties were carefully examined to reveal the corresponding relations. During the reaction, Dy_2O_3 and Nd_2O_3 additives were found to form nano-size DyB_4 and NdB_6 inclusions, respectively. These inclusions (20 nm – 150 nm) were observed both inside MgB_2 grains and on grain boundaries. No changes in B_{c2} and T_c were observed in the REO doped samples. Microstructural evidence shows the MgB_2 grain size to be reduced in response to REO doping and this grain refinement is more notable at higher HT temperatures. This grain refinement by REO doping increased both transport J_{ct} and magnetic J_{cm}. The peak positions of F_p in REO doped samples were all located at or near b=0.2; the $F_{p,max}$ of REO doped samples increased with the reciprocal of grain size 1/D as expected for GB pinning.

We provide a hypothesis to explain the mechanism of REO doping in MgB_2, Figure 68. During heat treatment, REO reacts with Mg and B, and forms nano-size REB_x inclusions. These inclusions stay on MgB_2 grain boundaries or inside MgB_2 grains. Those on MgB_2 grain boundaries act as grain growth inhibitors and slow down MgB_2 grain coalescing, leading to the observed grain refinement in the REO doped MgB_2; the inclusions inside MgB_2 grains, if with appropriate sizes, can act as pinning centers to enhance flux pinning. Thus, both of these two effects - grain refinement and new pinning centers - contribute to the improvement of F_p, which leads to the improvement of J_c. Because of these, MgB_2 bulk and wires can benefit from REO doping and REO doping is

useful to further improve the in-field performance of doped MgB_2 superconductors (e.g. C doped MgB_2 wires).

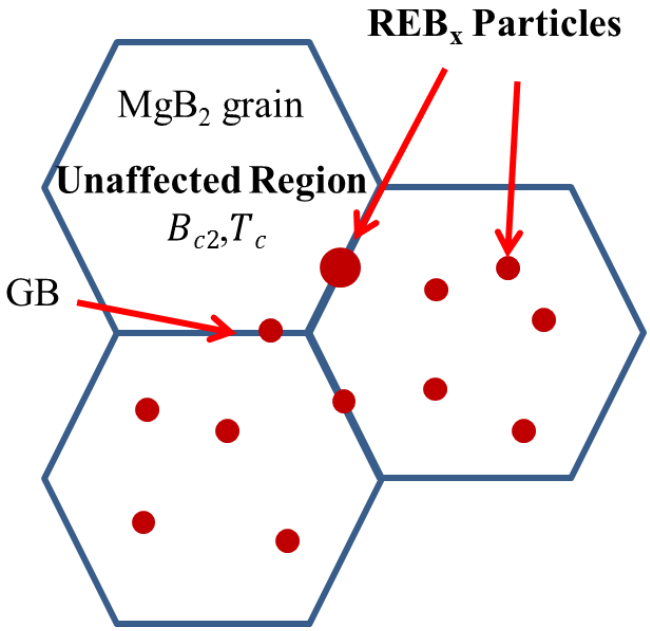

Figure 68 A schematic is used to describe the mechanism of REO doping in MgB_2. REB_x particles (red) do not distort MgB_2 grains around/containing them. Thus, the B_{c2} and T_c are unaffected by REO doping.

Chapter 5: Influence of Metal Diboride and Dy_2O_3 Additions on the Structure and Properties of MgB_2 Fabricated at High Pressures and Temperatures[1]

In this chapter, high pressure and temperature processing has been used to study the effects of chemical doping in MgB_2. The metal diborides ZrB_2, TiB_2 and NbB_2 were selected as additives since these compounds as well as MgB_2 all have AlB_2-type structure and similar lattice parameters. Dy_2O_3 was also selected as it has been reported to enhance the flux pinning in MgB_2. While C is known to enter the B-sublattice readily, attempts to dope Zr and other elements onto the Mg site have been less successful due either to their slow bulk diffusion, their low solubility in MgB_2, or both. We have used high-temperature, solid-state sintering (1500°C), as well as excursions through the peritectic temperature (up to 1700 °C), to investigate both of these limitations. Bulk MgB_2 samples doped with MB_2 (M = Zr, Ti and Nb) and Dy_2O_3 additions were synthesized. The resulting microstructures were observed using SEM, while atomic substitution and intra-/inter-granular impurities were evaluated by TEM and STEM. The upper critical field B_{c2}, irreversibility field B_k, the

[1] This chapter is based on the published article: Y. Yang *et al*., "Influence of Metal Diboride and Dy_2O_3 Additions on Microstructure and Properties of MgB_2 Fabricated at High Temperatures and Under Pressure", *Sci. Rep.* **6,** 29306 (2016).

superconducting transition temperature T_c and flux pinning were obtained from magnetic measurements.

5.1 Motivation of Metal Diboride Doping into MgB_2

In order to enhance the B_{c2} of MgB_2 in the higher temperature regime (T > 20 K), extensive efforts have been made to find effective dopants for Mg-site substitution to increase electron impurity scattering in both the σ-band and the π-band [11,43]. Due to lack of ternary phase diagrams of M, Mg and B, it is critical to find new criterions for potential chemical dopants. We selected Zr, Ti and Nb because the metal diborides ZrB_2, TiB_2 and NbB_2 as well as MgB_2 all have AlB_2-type structure and similar lattice parameters. Also, the use of existing metal diborides (MB_2) with a structure isomorphic to MgB_2 (P6/mmm) and lattice parameters close to those of MgB_2 as a vector for effective metal element doping is a promising way to investigate possible changes of superconducting properties. Thus, MgB_2 bulk samples doped with ZrB_2, TiB_2 and NbB_2 powders were prepared. As described in Section 2.3, HPT process is used to enhance diffusion during sample synthesis since HT temperatures used in HPT process is very high (above 1500 °C).

Most additions to MgB_2 tend to accumulate at the grain boundaries, with the exception of the above mentioned C-bearing additions. On the other hand, in Chapter 4 our study showed that a small amount of Dy_2O_3 can form nanoscale precipitates within the

MgB_2 grains and thereby enhance flux pinning without changing T_c. Thus a Dy_2O_3 doped MgB_2 HPT bulk was also included in this study for comparison.

5.2 Sample Synthesis

Three sets of MgB_2 bulk samples with various MB_2 (M=Zr, Ti and Nb) dopants were fabricated by the high pressure and temperature process (HTP) described in Section 2.1 [98,127]. A schematic of the HTP process is given in Figure 25. Three metal diborides with a structure isomorphic to MgB_2 (P6/mmm) were selected as vectors for Mg-site substitution: ZrB_2 (99.5%, Alfa Aesar), TiB_2 (99.5%, Alfa Aesar) and NbB_2 (99.5%, Alfa Aesar). To synthesize the Dy_2O_3 doped sample, Dy_2O_3 (>99.9%, <100 nm particle size, Aldrich) was used. Amorphous B powder (50-100 nm in size) manufactured by SMI [92] was used. All samples were heat treated at 10 MPa in an Ar atmosphere. Two heat treatment routes were used: Route 1, heating up to 1500 ºC and soaking for 30 min; Route 2, heating up to 1700 ºC and soaking for 20 min. A slow cooling rate of 5ºC/min was used in both HT routes to maintain thermal equilibrium. The first route limited the temperature to just below the peritectic decomposition point, T_p, thus preventing decomposition while maximizing the diffusion of the dopant species. The second route allowed the reaction to occur on the temperature upswing, and hence to form MgB_2 directly from MgB_4 and Mg+dopant species on cooling:

$T < T_p$ $$Mg + 2B \Rightarrow MgB_2 \quad (53)$$

$T > T_p$ $$2MgB_2 \Rightarrow MgB_4 + Mg \quad (54)$$

Cooling $$MgB_4 + Mg \Rightarrow 2MgB_2 \quad (55)$$

where T_p, the peritectic temperature, is ~ 1500 °C in our experiments. In this case we may increase our chance to inject the dopant species into the MgB_2. There are two main reasons for using HPT to fabricate doped MgB_2 bulk samples: (1) to explore the limits of the solubility of dopant species in doped MgB_2 bulk samples (Route 2); (2) to overcome the diffusion barrier and increase the diffusion based doping (Route 1). However, in addition to these two main reasons, with such elevated HTs, it is natural to produce much larger MgB_2 grain sizes, which are convenient for structural and intragrain chemical studies. In addition to this, such HPT processing will also promote sample homogeneity.

Table 23 Doping levels, heat-treatment parameters, lattice parameters and MB_x impurity amounts for the MgB_2 samples.

Sample	Dopant:B ratios[1]	HTs at 10MPa	a, Å[2]	a_{cal}, Å[3]	c Å	c_{cal}, Å	MB_x Impurities[4]
HPT-01	-	1500ºC, 30min	3.082(5)	-	3.521(7)	-	-
HPT-Zr-01	ZrB_2:B=1:40	1500ºC, 30min	3.086(4)	3.085	3.530(1)	3.522	1wt%ZrB_2
HPT-Zr-02	ZrB_2:B=1:19	1700ºC, 20min	3.090(2)	3.091	3.527(4)	3.522	8.6wt%ZrB_2
HPT-Ti-01	TiB_2:B=1:40	1500ºC, 30min	3.089(3)	3.082	3.523(8)	3.516	1.7wt% TiB_2
HPT-Ti-02	TiB_2:B=1:19	1700ºC, 20min	3.085(4)	3.077	3.520(2)	3.492	11.3wt%TiB_2
HPT-Nb-01	NbB_2:B=1:40	1500ºC, 30min	3.086(3)	3.084	3.517(4)	3.517	2.7wt%NbB_2
HPT-Dy	Dy_2O_3:B=1:800	1700ºC, 20min	3.082(9)	-	3.522(5)	-	1.4wt%DyB_4

[1]. These ratios were based on the mole ratios between the dopants and B in the mixtures;
[2]. The lattice parameters a and c were extracted from pseudo-Voigt fitting;
[3]. The a_{cal} and c_{cal} were the calculated values based on Vegard's law by assuming that all dopants form a homogeneous solid solution with MgB_2;
[4]. The x in MB_x are 2 in the MB_2 doped samples and 4 in the Dy_2O_3 doped sample, respectively.

5.3 Influence of MB_2 and Dy_2O_3 Doping on XRD and Lattice Parameters

The X-ray diffraction data for all HTP bulk samples are presented in Figure 69 where the Bragg reflections are indexed for only the MgB_2 phase for simplicity. MgO and Mg were present at some level in all samples (MgO was less than about 2 wt% for samples reacted below the peritectic). MgB_4 peaks are also present for samples HT at 1700 °C. Only a very small peak shift (less than 0.2 degree) at both (110) and (002) was observed in MB_2 doped samples while no peak shift was observed for the Dy_2O_3 doped sample. Peaks corresponding to MB_x impurity phases were observed in all MB2 doped samples. The lattice parameters extracted from pseudo-Voigt fitting the MgB_2 peak reflections and the calculated lattice parameters by Vegard's law are given in Table 23. For the Dy_2O_3 added sample HPT-DY, similar to Chen *et al.*'s report [119], the lattice parameters *a* and *c* did not change with Dy_2O_3 addition. Similarly, for the MB_2 added samples, lattice parameters *a* and *c* were changed within experimental uncertainty, which did not obey Vegard's law, unlike C-doped MgB_2 HTP bulk [97]. Therefore, it seems that even under HPT processing the metal borides (ZrB_2, TiB_2 and NbB_2) mainly acted as impurity phases and did not form homogeneous solid solutions with MgB_2, at least not to an extent detectable by XRD.

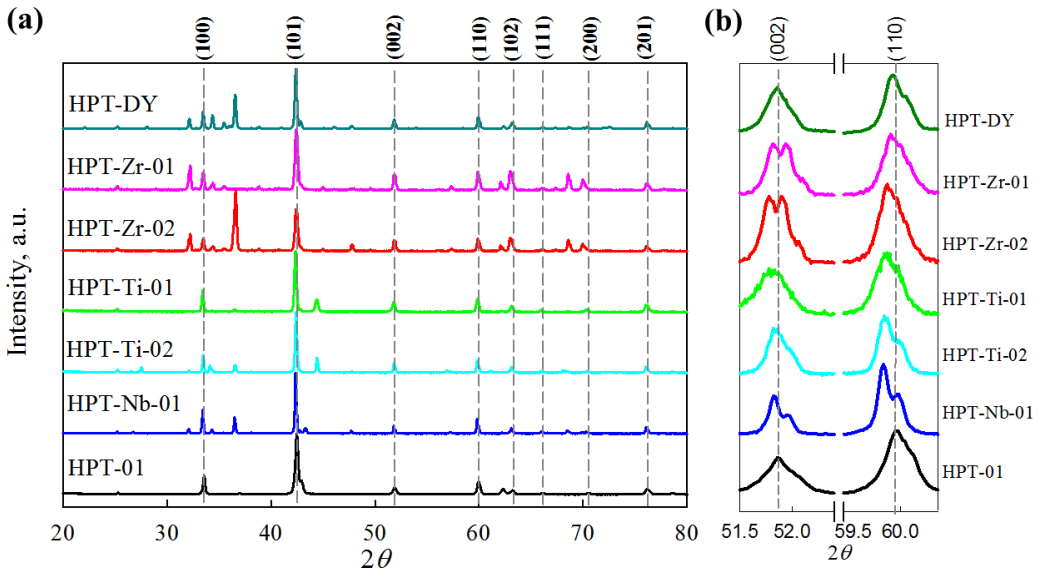

Figure 69 (a) X-ray diffraction characterization of undoped MgB_2 sample HPT-01, and all theMB_2 doped samples; (b) Peaks (110) and (002), as these two peaks are directly related to lattice parameter *a* and *c*, respectively. Note for the MB_2 doped samples, small peak shifting and MB_2 peaks are observed.

5.4 Influence of MB_2 and Dy_2O_3 doping on microstructure - SEM and TEM

5.4.1 Microstructures of ZrB_2 Added Samples

The results of back-scatter (BSE) SEM characterization performed on the ZrB_2 doped samples are presented in Figure 70. The microstructures of HTP-Zr-01 (1500 ºC, below the peritectic temperature) and HTP-Zr-02 (1700 ºC, above the peritectic temperature) are shown in Figure 70 (a) and 69 (b). Two phases are visible (Z-contrast) and confirmed by EDS: MgB_2 (majority phase, dark grey) and ZrB_2 (minority phase, white)

in HTP-Zr-01; while in HPT-Zr-02, Mg and MgB_4 phases were clearly present since it underwent the reaction $Mg+MgB_4 \rightarrow MgB_2$.

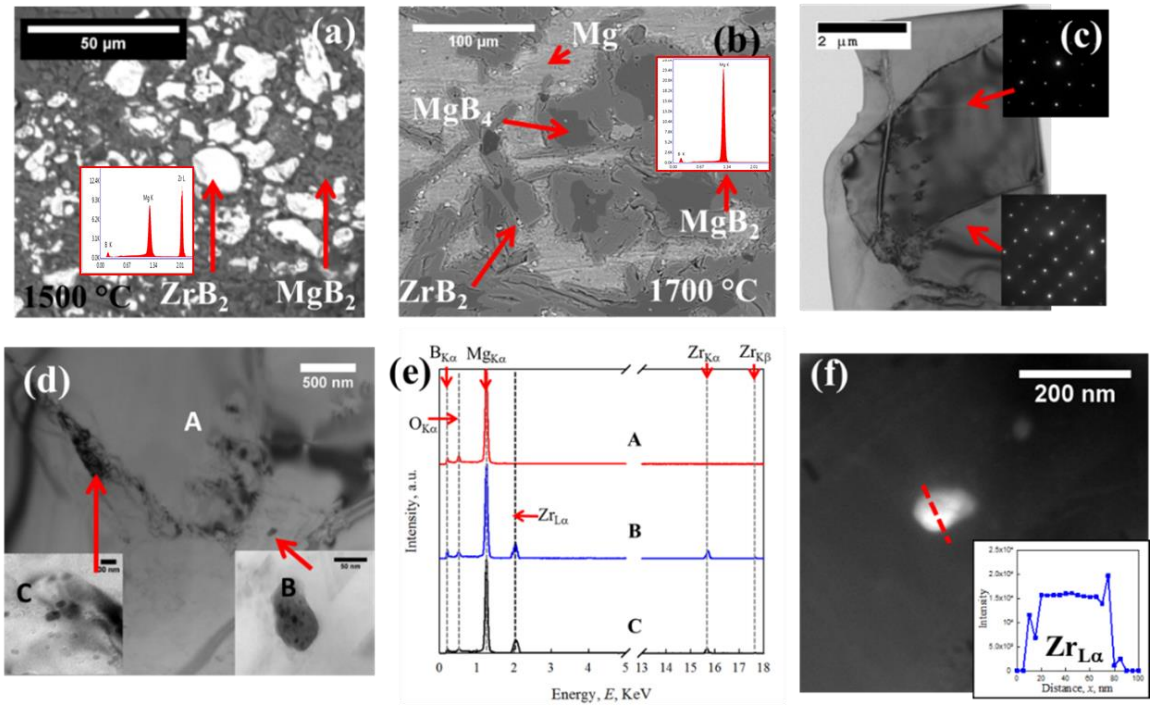

Figure 70 (a) BSE image of HTP-Zr-01; (b) BSE image of HTP-Zr-02; (c) BF TEM image of HTP-Zr-02. Insets are SAD of two distinct MgB_2 grains; (d) nano-size inclusions observed close to/at MgB_2 grain boundaries; (e) EDS spectra of spot A, B and C; (f) HAADF image of a nano-size inclusion close to MgB_2 grain boundaries. Inset is the intensity of Zr signal from STEM-EDS scanning across the inclusion (red dash line).

Figure 70 (c) represents the bright-field (BF) TEM image obtained from a thin foil extracted from HTP-Zr-02 (1700 °C). This foil contains a cross section of several grains. The results from the energy dispersive spectroscopy analysis (EDS) and selected area diffraction (SAD) confirm that these large grains are MgB_2. An intragranular crack and dislocation loops are present in one of the grains. Since HPT-Zr-02 was processed above

the peritectic, the crack presumably resulted from volume expansion taking place during cooling as the MgB_4 converted into MgB_2. TEM examination revealed a number of impurity phases in the form of 30–80 nm inclusions around the MgB_2 grains, Figure 70 (d). The results of EDS analysis performed on these inclusions are presented in Figure 70 (e). It is clear that these inclusions contain Zr, or possibly ZrB_2, which is likely dispersed around the MgB_2 grains in the bulk. Compared to other areas inside the MgB_2 grains, the regions around these ZrB_2 inclusions have much higher contrast under BF condition, which suggests that strain fields were generated around these inclusions and that the MgB_2 lattice was distorted locally. This speculation is based on the TEM imaging which is only sampling small regions of the samples and is not statistical in nature. This local lattice distortion may be the origin of the slight lattice parameter changes observed by XRD analysis in Section 5.4. Figure 70 (f) shows HAADF imaging for one of these nano-size inclusions. Since HAADF imaging is sensitive to variations in the atomic number (Z-contrast), these white inclusions should have a higher average atomic number than MgB_2. A STEM-EDS line scan applied using 21 distinct points over ~100 nm across this inclusion confirmed it was ZrB_2. The Zr signal dropped to zero quickly outside of the inclusion, beyond the ZrB_2/MgB_2 interface. The spatial resolution of the STEM-EDS line scans is about 5 nm, thus these observations indicate that Zr did not notably penetrate into the MgB_2 lattice.

5.4.2 Microstructures of TiB_2 Added Samples

Figure 71 shows the BSE images of the TiB_2 doped samples, HTP-Ti-01 (1500 °C, below the peritectic) and HTP-Ti-02 (1700 °C, above the peritectic). Similar to the behavior of ZrB_2, TiB_2 mainly acts as an impurity phase (light grey in Figure 71 (a) and (b)) and is widely distributed (confirmed by EDS). A TEM thin foil containing a cross section of both TiB_2 and MgB_2 grains was carefully extracted from HTP-Ti-01. A BF image including MgB_2, TiB_2, and their interface is represented in Figure 71 (c). A large number of defects can be observed inside the MgB_2 grains close to the MgB_2/TiB_2 interface. Inclusions 100–200 nm in size are found at the interface as well as at MgB_2 grain boundaries. EDS analysis confirms that these inclusions are MgO, Figure 71 (f). Dark-field (DF) imaging was also used to examine the dislocations and the interface since crystal defects have stronger contrast under DF conditions. In Figure 71 (d), the DF image clearly confirms that the MgB_2 grain contains a high density of defects. Detailed in-grain analysis was performed using HAADF imaging. Figure 71 (e) shows a HAADF image of MgB_2 grains with high defect density. Nano-size inclusions (~10–30 nm, white) dispersed both in and around MgB_2 grains were observed. EDS analysis performed on randomly selected white inclusions confirmed that they were TiB_2 (EDS spectrum of spot E (inclusion) in Figure 71 (f)). No Ti was detected by EDS in the other regions of MgB_2 grains (EDS spectrum of spot D (matrix) in Figure 71 (f)). STEM-EDS analysis was applied across inclusion E, and beyond the TiB_2/MgB_2 interface the intensity of the Ti signal quickly dropped to zero, indicating that Ti did not dissolve into the MgB_2 lattice. These nano-size

TiB_2 inclusions can also contribute to the high defect density observed in MgB_2 grains in Figure 71 (c) and (d).

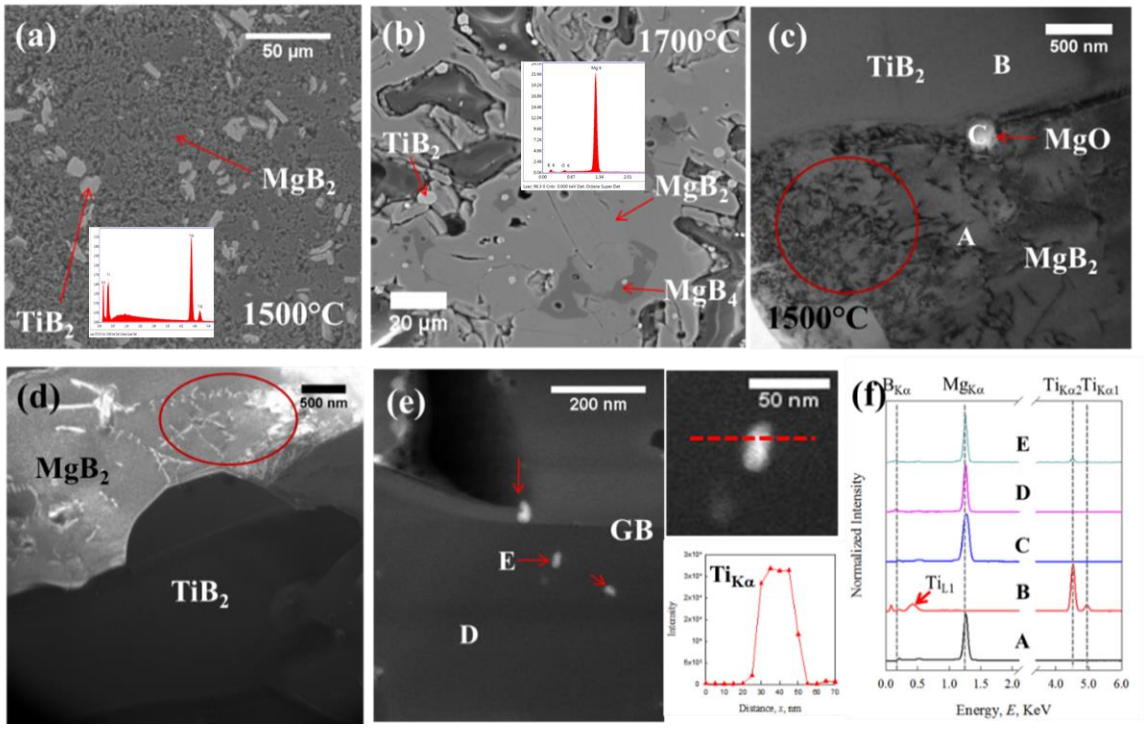

Figure 71 (a) BSE image of HTP-Ti-01; (b) BSE image of HTP-Ti-02; (c) BF TEM image of HTP-Ti-01. Large amount of crystal defects in MgB_2 grain close to MgB_2/TiB_2 interface; (d) DF TEM image of ingrain crystal defects in MgB_2 grain close to TiB_2; (e) HAADF image of MgB_2 grains with high defect density and STEM-EDS scanning across one of the nano-inclusions (red dash line). Inset is the intensity of $Ti_{K\alpha}$; (f) EDS spectra of spots A-E from (c) and (e).

5.4.3 Microstructures of NbB_2 Added Samples

In the NbB_2-added sample HTP-Nb-01 (HT below the peritectic), three phases are visible and confirmed by EDS in the BSE images of Figure 72 (a) and (b): MgB_2 (majority phase, dark grey), MgO (minority phase, light grey) and NbB_2 (minority phase, white). In Figure 72 (b), based on fractured secondary electron (SE) imaging by 'through the lens' (TTL) detection, NbB_2 particles are observed outside the MgB_2 grains. These particles are small (~300–500 nm), well connected with the MgB_2 grains, and dispersed throughout the bulk samples.

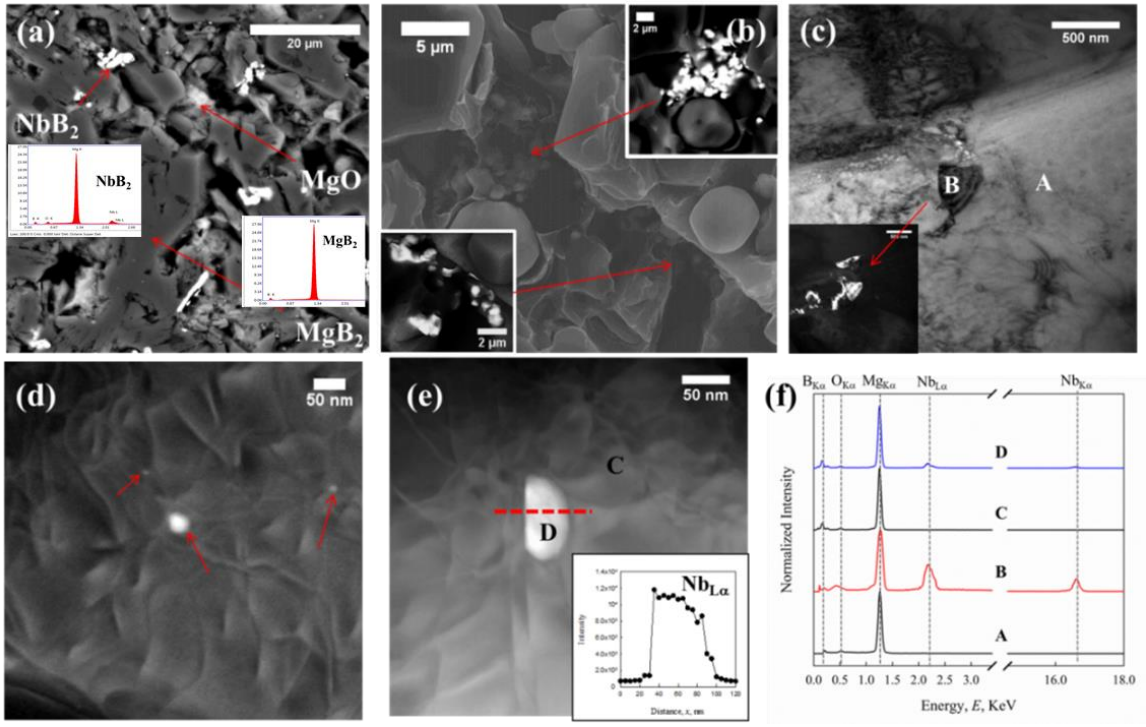

Figure 72 (a) BSE image of HTP-Nb-01; (b) fractured SE images, insets are BSE image of the fractured area; (c) BF TEM image of HTP-Nb-01 contained NbB_2 inclusions. Inset is the DF TEM image of NbB_2 inclusions; (d) MgB_2 grains with high density of defects; (e) STEM-EDS scanning across one of the nano-inclusions (red dash line); (f) EDS spectra of spot A-D.

Further analysis was performed on a TEM thin foil sectioned from HTP-Nb-01. Both BF (Figure 72 (c)) and DF images (Inset of Figure 72 (c)) show nano-size inclusions (~300 nm) embedded in the MgB_2 grain boundaries. Moreover, a large number of defects can be observed inside the MgB_2 grains around these inclusions, while the other MgB_2 grains have fewer intragranular defects. The EDS results in Figure 72 (e) confirm that these inclusions are NbB_2. HAADF imaging performed on MgB_2 grains with high density of defects is presented in Figure 72 (d) and (e). Nano-size inclusions (~10–50 nm, white) were found inside these grains and high strain fields were observed around them. EDS analysis was applied on these distinct inclusions and several randomly selected spots in the matrix; those for spot C (matrix) and spot D (inclusion) are presented in Figure 72 (f). These EDS results confirm that these white inclusions were NbB2. A STEM-EDS line scan was applied across inclusion D. The intensity of Nb signals abruptly decreased from ~ 10^4 to zero across the NbB_2/MgB_2 interface and no Nb was detected in the other regions of the MgB_2 grains.

5.4.4 Microstructures of Dy_2O_3 Added Samples

The microstructure of HTP-DY (HT above the peritectic) was investigated by back-scattered imaging, Figure 73 (a). Five phases are visible: MgB_2 (majority phase, dark grey), Mg (main phase, grey), MgB_4 (minority phase, black), MgO (minority phase, light grey) and Dy-containing inclusions (minority phase, white). These Dy-containing

inclusions (possible DyB_4 according to XRD results) with a size of ~ 100 nm were likely dispersed throughout the bulk. Bright-field TEM examination revealed a number of impurity phases in the form of ~ 10 - 50 nm inclusions inside the MgB_2 grains in Figure 73(b). A low density of large inclusions (over 100 nm) was also observed (Figure 73 (c)). The HAADF image of Figure 73 (c) showed that these nano-size inclusions had a higher average atomic weight as confirmed by EDS in Figure 73(d). These inclusions contained Dy and B which suggests that they were DyB_4 as shown in the XRD results. The Cu signals that were also collected in the EDS spectrums in Figure 73 (d) were most likely contributed by the Cu TEM grid. The STEM-EDS analysis with 21 distinct points was applied across the half of the inclusion B (the red dash line in Figure 73(c)) and the result is in Figure 73(e). No Dy was detected outside the inclusion.

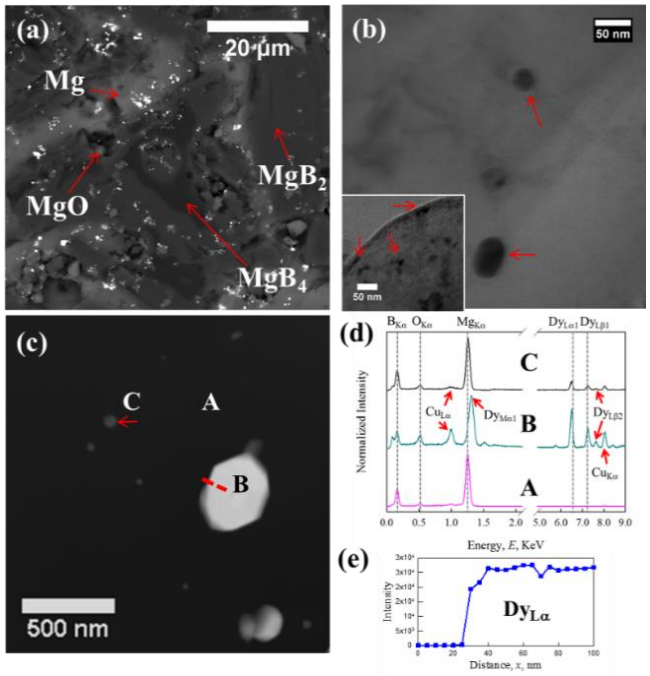

Figure 73 (a) BSE image of HTP-DY, four different phases (MgB_2, MgB_4, Mg and MgO) are labeled; (b) BF TEM image of nano-size inclusions (10 – 50 nm) are found inside MgB_2 grains; (c) HAADF image of one MgB_2 grain, white precipitates are Dy-containing; (d) EDS spectra of spot A-C in (c); (e) the intensity of $Dy_{L\alpha}$ from STEM-EDS scanning (red dash line in (c)).

5.5 Influence of MB_2 and Dy_2O_3 Doping on Superconducting Transition Temperature T_c and T_c Distribution

The T_c and the distribution of T_c were obtained by magnetization measurements, Figure 74. The onset T_c values and the full-width half maximum (FWHM) of all samples are listed in Table 24. The undoped sample HPT-01 shows a sharp superconducting transition with a T_c of 39.5 K and a FWHM of ~ 0.4 K. Below we describe the results for the doped samples.

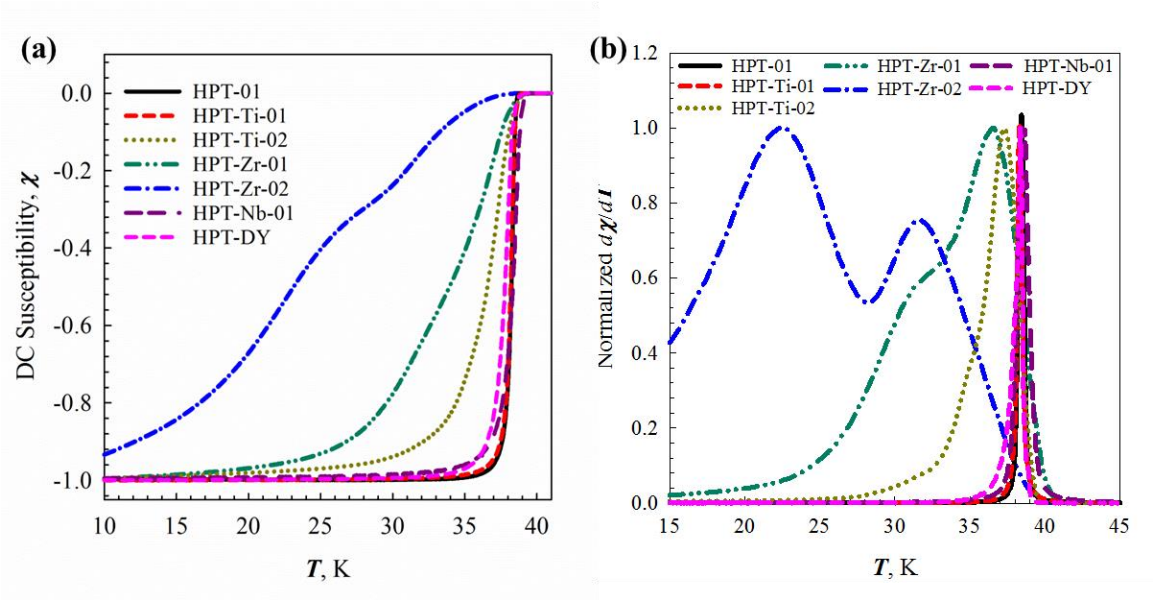

Figure 74 (a) DC susceptibility χ vs. T at 0.01 T; and (b) the T_c distribution - dχ/dT vs. T of the all MgB_2 samples.

Table 24 Comparison of the superconducting properties amount the MgB_2 samples

Sample	Onset T_c (K)	FWHM of T_c (K)	B_{c2} at20 K (T)	B_k at 15 K (T)	F_{pmax} at 15 K (GN/m^3)
HPT-01	39.5(1)	0.4	5.8(1)	3.6(1)	0.095
HPT-Zr-01	39.2(2)	~10	10.0(4)	2.5(3)	0.063
HPT-Zr-02	39.4(3)	>15	8.0(4)	-	-
HPT-Ti-01	39.5(2)	0.5	10.0(5)	3.3(2)	0.079
HPT-Ti-02	39.6(2)	2.8	8.2(4)	-	-
HPT-Nb-01	39.8(2)	1.0	9.0(3)	2.9(2)	0.091
HPT-DY	39.2(1)	0.5	5.6(2)	3.5(1)	0.134

In the ZrB_2 doped samples, the onset T_c values are 39.2±0.2 K in HPT-Zr-01 and ~ 39.4±0.2 K in HPT-Zr-02, respectively. The unchanged T_c values suggest that a portion of these ZrB_2 doped samples was unaffected with a T_c equal to that of the undoped sample.

Figure 74 (a) and 74 (b), show very broad transitions and bi-modal peak in the T_c distribution. This effect became more severe in HPT-Zr-02 indicating the presence of regions with various T_c values. Similarly, in the TiB_2 doped samples, the onset T_c values were unchanged, while their FWHMs were increased to ~0.5 K in HPT-Ti-01 and ~2.8 K in HPT-Ti-02, respectively. The NbB_2 doped sample HPT-Nb-01 has an onset T_c of 39.8 K and a FWHM of ~ 1.0 K. The Dy_2O_3 doped sample HPT-DY has an onset T_c of 39.2 K and a FWHM of ~ 0.5 K.

The results for each of the MB_2 samples was similar-after MB_2 doping, the onset T_c values were relatively unaffected within uncertainty, however their transition widths were significantly enhanced. We interpret this effect in terms of the presence of nanoscale MB_2 (where M = Zr, Nb, or Ti) second phases which produce locally distorted regions separated by large regions of unaffected MgB_2, leading to broadened T_c distributions with a wide T_c variation ranging from 39 K to low values. Since these MB_2 additives are isomorphic to MgB_2 and their lattice parameters are close to those of MgB_2, the localized distortion is probably due to the coherent strain generated around the MB_2 inclusions. However, in HPT-DY both the onset T_c and FWHM did not change by adding Dy_2O_3, which is consistent with Chen's observation [119]. The lattice parameters and crystal structures of Dy_2O_3 (cubic with space group Ia-3) [168] and DyB4 (tetragonal with space group P4/mbm) [169] are very different from MgB_2 (hexagonal with space group P6/mmm) [1], therefore it is unlikely that the Dy-containing inclusions in HPT-DY can generate coherent strain in the MgB_2 grains.

As indicated above the MB_2 dopants were mostly found as distinct impurity inclusions that only influenced the surrounding MgB_2 grains through the MgB_2/MB_2 interfaces. Increasing the concentration of MB_2 inclusions produced more "affected zones" leading to a wider T_c distribution, Figure 74(b). The behaviors of MB_2-doped samples are quite different from those of C-doped MgB_2 bulk samples [97]. After doping with 6.2 at. % C Susner *et al.* [97] observed a significant decrease in the onset T_c, from 39.5 K to ~ 24 K, while the FWHM changed from 0.65 K to 1.4 K [97]. Since C is known to be a substitutional defect, if homogeneous C doping is achieved, the onset T_c and the lattice parameter *a* will decreased simultaneously with increasing C doping levels [97]. Under MB_2 doping, it seems that Zr, Ti and Nb did not substitute for Mg or form homogeneous solid solutions with MgB_2, even under 1700 ^oC and 10 MPa. Based on the results in Section 5.5.1 - Section 5.5.3, the affected vicinities probably had a thickness similar to or smaller than 5 nm - the resolution of STEM-EDS line scans used in this study.

5.6 Influence of MB_2 and Dy_2O_3 Doping on Upper Critical Field B_{c2} and Irreversibility Field B_k

The *T* dependencies of the B_{c2}s of all the samples are presented in Figure 75(a). The B_{c2} values at 20 K (in Table 24) and 30 K linearly extrapolated from Figure 75(a) are plotted in Figure 75(b). It is clear that the B_{c2} values were increased by MB_2 doping, but not by Dy_2O_3 doping. For example, the B_{c2}(20 K) of the undoped sample HPT-01 is ~ 5.8 T, while those of HPT-Zr-01, HPT-Ti-01, HPT-Nb-01 and HPT-DY are ~ 10 T, ~ 10 T, ~ 9 T and

~ 5.6 T, respectively. It is important to note, however, that since these MB_2 doped samples were not homogeneous (as evidenced by the microstructure and the T_c distribution), the B_{c2} values represent the properties of only small fractions of the bulk samples. In other words, some "affected zones" inside these doped bulk samples have higher B_{c2} values than those in the unaffected MgB_2. The observed high defect densities in the affected MgB_2 grains, which increase electron scattering and reduce the electron mean free path, likely contributed to regions of higher B_{c2}. In the Dy_2O_3 doped sample, although nano-size inclusions were observed inside the MgB_2 grains, B_{c2} did not change. This observation together with the absence of changes in lattice parameters, T_c, and FWHM supports the conclusion that Dy_2O_3, unlike MB_2, did not affect the chemistry or the lattice of MgB_2.

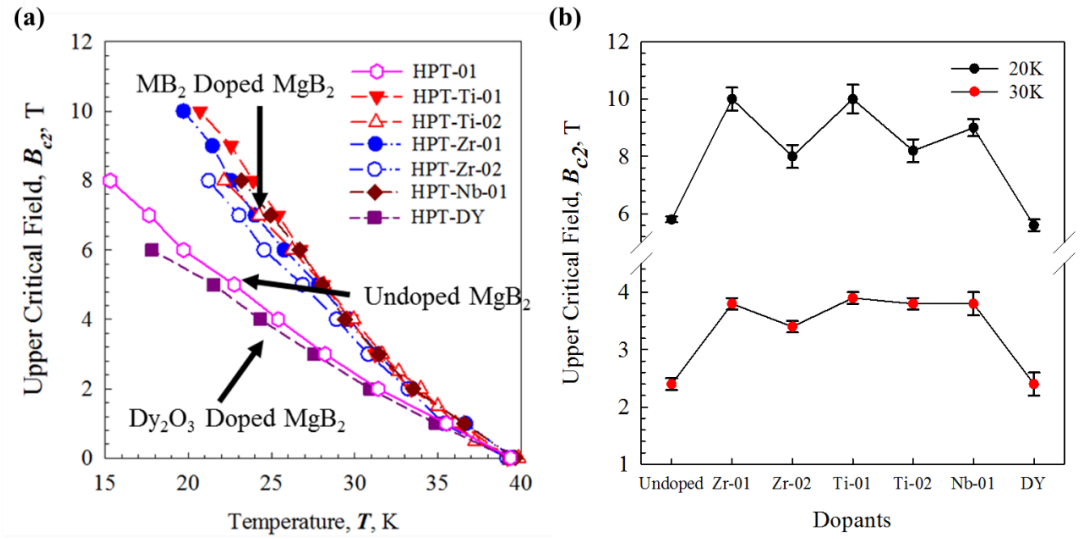

Figure 75 (a) The temperature dependent B_{c2} (T) curves of the all MgB_2 samples. (b) The B_{c2} vs. Dopants at 20 K and 30 K.

5.7 Influence of MB_2 and Dy_2O_3 Doping on Magnetic Critical Current Density J_{cm} and Flux Pinning Behavior

Magnetic critical current density J_{cm}s and flux pinning behaviors of selected samples were calculated based on equation (29) and sample geometries:

$$J_{cm} = \frac{2\Delta M}{b(1-b/3a)} \tag{56}$$

where ΔM is the width of the hysteresis loop at a given field B, a and b are the edge lengths of the sample orthogonal to B ($a > b$). The results at 15 K are shown in Figure 76. The J_{cm} values at low magnetic fields were reduced by MB_2 doping, while the J_{cm} values at higher fields were increased (except in HPT-Nb-01). For HPT-DY, its J_{cm} was slightly increased at all measured fields. A "tail" in $J_{cm}(B)$ can be observed in all doped samples.

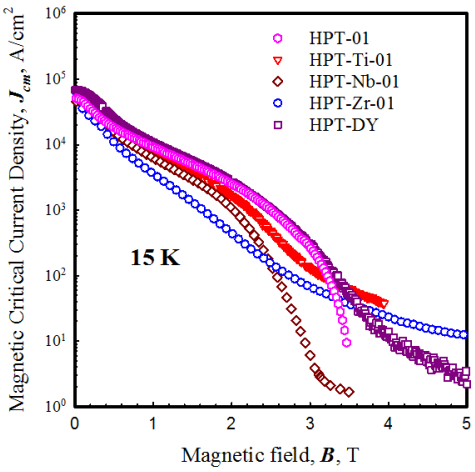

Figure 76 Magnetic critical current density J_{cm} vs. T curves of the undoped sample HPT-01 and the doped samples HPT-Zr-01, HPT-Ti-01, HPT-Nb-01 and HPT-DY at 15 K.

A Kramer Plot, $J_c^{0.5}B^{0.25}$ vs. B, is shown in Figure 77. The irreversibility fields, B_k, taken at the cross-intercepts of linear fittings (black dash lines in Figure 77) are listed in Table 24. Interestingly, B_k was reduced after MB_2 doping, unlike the values of B_{c2} which increased with doping. This effect is due to two factors: (1) the Kramer plots for the doped samples are no longer linear at high fields and the "tail" behaviors observed in both Figure 76and Figure 77indicate that the MB_2 doped samples had higher B_{c2} values; (2) the B_k is also affected by the sample connectivity. As a result of the large phase fraction of impurities in the doped samples that were observed in XRD and SEM, their J_{cm} and B_k were indeed underestimated. Taking these into account, Dy_2O_3 doping though it did not increase B_{c2}, did increased J_{cm}.

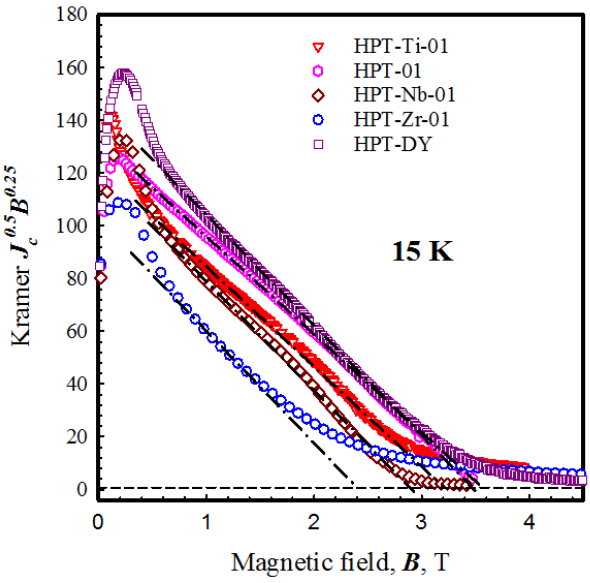

Figure 77 Kramer plot $J_c^{0.5}B^{0.25}$ vs. B curves of the undoped sample HPT-01 and the doped samples HPT-Zr-01, HPT-Ti-01, HPT-Nb-01 and HPT-DY at 15 K.

Figure 78is a plot of bulk pinning force density ($F_p = J_{cm} \times B$) vs. B. The maximum F_p values, F_{pmax}, are listed in Table 24. Compared to the literature values, F_{pmax} of these HPT processed bulk samples are relatively small. The F_{pmax} of the undoped sample HPT-01 is only ~ 0.095 GN/m^3 while according to Susner [9] at 15 K the F_{pmax} of an undoped MgB_2 wire was about 2 GN/m^3. This difference can be attributed to the fact that the MgB_2 grains in these HPT bulk (> 5 μm) are much larger (by a factor of about 20×) than those in the traditionally synthesized samples (typically 30-500 nm).

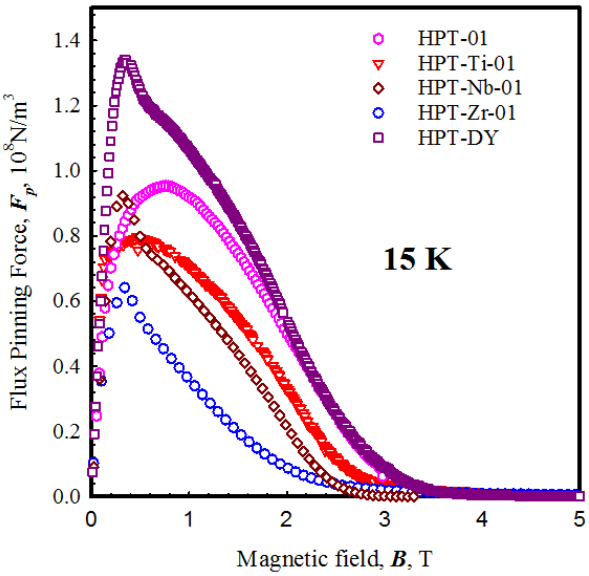

Figure 78 The flux pinning density F_p vs. B curves of the undoped sample HPT-01 and the doped samples HPT-Zr-01, HPT-Ti-01, HPT-Nb-01 and HPT-DY at 15 K.

The normalized bulk pinning force density $f_p = F_p / F_{p,\max}$ is plotted against normalized magnetic field $b = B / B_k$ in Figure 79. The grain boundary (GB) pinning

function from Dew-Hughes [65], $f_p \propto b^{1/2}(1-b)^2$, is also plotted for comparison. Although the undoped sample HPT-01 followed the GB pinning quite well, all doped samples show a deviation from the standard function. The peaks of f_p in the doped samples were shifted from the value of b=0.2 (the peak position of the GB pinning) to lower values. For example, the peaks in HPT-Zr-01, HPT-Ti-01, HPT-Nb-01 and HPT-DY were 0.12, 0.13, 0.11 and 0.10, respectively. This observation which was also reported by Matsushita *et al.* [172] in C doped MgB_2 bulk samples can be explained by two possibilities. The first possibility is that these doped samples might contain a series of local B_k values instead of a single value (just like B_{c2} in the MB_2 doped samples). The variation in B_k of the undoped sample was small and its f_p followed the GB pinning function. The second possibility is that this deviation might be caused by the operation of more than one pinning mechanism (for example normal volume pinning in which f_p maximizes at $b \rightarrow 0.0$ [65]) in association with the GB pinning. The parameter a of the flux line lattice (FLL) is given by $a = 1.07(\Phi_0/B)^{1/2}$, where Φ_0 is the quantum of magnetic flux ($\Phi_0 = 2.07 \times 10^{-15}$ Wb). Based on this expression, the values of a vary from ~ 50 nm at 1 T to ~ 20 nm at 6 T. By definition, the size of the volume pins needs to be larger than a. Considering the fact that these doped samples contained a series of in-grain inclusions (with sizes of 10 - 80 nm) some of which were bigger than the FLL parameter a at every measured field, it is quite possible that the normal volume pinning contributed to these shifts in $F_{p,max}$. All of these possibilities may contribute to the observed peak shifts.

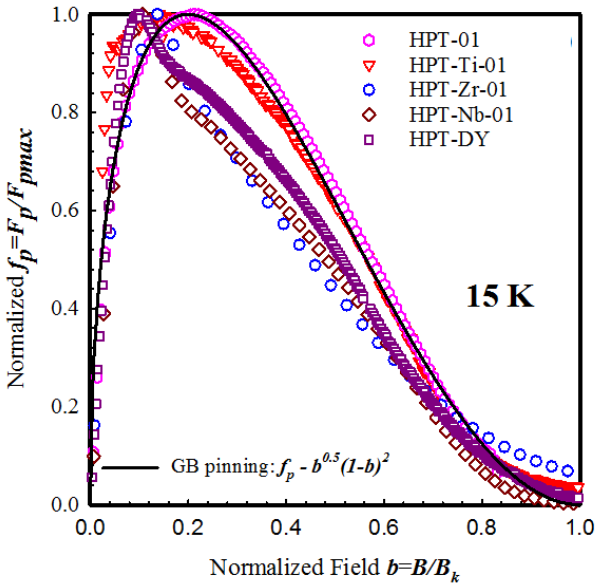

Figure 79 Normalized flux pinning behavior f_p vs. b of the undoped sample HPT-01 and the doped samples HPT-Zr-01, HPT-Ti-01, HPT-Nb-01 and HPT-DY at 15 K.

5.8 Summary of MB_2 Doping in MgB_2

In this chapter we have used HPT method for synthesizing doped MgB_2 bulk at high temperatures (up to 1700 °C) and at pressure (10 MPa) to enhance diffusion and (alternatively) attempt to form dense, nanoscale secondary phases during the sample synthesis. We explored both metal diborides (MB_2, where M = Zr, Ti and Nb) for attempted Mg site substitution and Dy_2O_3 for nanoscale intragrain precipitate formation. Using the HPT process, we conclusively show that the large increases in B_{c2} with metal diboride additions are due to a highly defected band within the grain, rather than substitution or inclusion within the grain, or grain boundary effects. In Figure 80 we provide a hypothesis

to explain the possible mechanism of MB_2 doping. After heat treatment, majority of MB_2 dopant particles stay as second phases, while very small amount of MB_2 precipitate inside MgB_2 grains or on MgB_2 grain boundaries. Since these MB_2 dopants are isomorphic to MgB_2 and their lattice parameters are close to those of MgB_2, lattice strains and defects which are possibly due to coherent lattice mismatching form in MgB_2 around or with these MB_2 inclusions. High defect densities observed in MgB_2 grains around/with these MB_2 inclusions, cause electron scattering and therefore contribute to the B_{c2} enhancement and T_c distribution broadening. On the other hand, these distorted regions are not large enough to significantly influence the high field J_c or B_k. This model explains the frequently observed increases seen for B_{c2} in materials with no accompanying increase in transport current [8, 113-115]. Our results show lack of evidence for the site substitution (confirmed by EDS with nanometer special resolution and 1 at. % accuracy) driven property improvement, which might suggest that the high density of defects (partially observed by TEM) and associated lattice strain could be responsible to the changes in B_{c2} and T_c after MB_2 doping.

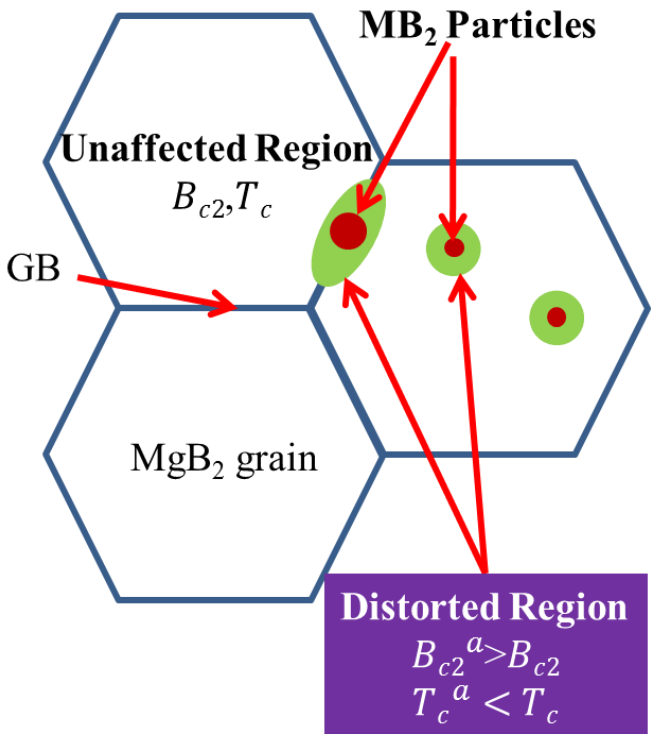

Figure 80 A schematic is used to describe the mechanism of REO doping in MgB_2. MB_2 particles (red) distort MgB_2 grains around/containing them (green). The B_{c2} and T_c of these distorted regions are different from the unaffected MgB_2 regions.

We also confirm the previously observed but sparsely distributed intragrain precipitates formed with Dy_2O_3 additions. Dy_2O_3 additions do not change the lattice parameters, T_c, T_c distribution and B_{c2} of MgB_2, but increased the J_c and flux pinning by forming an array of nano-size precipitates in MgB_2 grains. This observation is consistent with our previous results in Dy_2O_3 doped MgB_2 traditional bulk samples (chapter 4).

Chapter 6: Summary and Conclusions

The aim of this work is to obtain an understanding of the effects of chemical doping on the microstructures and superconducting properties in MgB_2 superconductors.

First, we studied the process using C doping to improve the in-field performance of the state-of-the-art MgB_2 wires. The influence of C doping on transport performance in MgB_2 monofilamentary wires were studied. Significant enhancements in the high field J_c, n-values and B_{c2} were achieved by C doping and the best transport performance was obtained by 3 at. % C doping. Additionally, we found that several parameters, e.g. HT temperature T, HT duration t, C concentration and B types, played important roles in the C doping efficiency. Moreover, the n-values and the pinning potential U in the undoped PIT, C doped PIT and C doped IMD samples have been studied in detail by three different approaches and we showed that C doping was observed to improve both n and U in high fields. The C doping in a set of MgB_2 multifilamentary wires was investigated in terms of transport properties, doping techniques, boron types, wire structure and strain tolerance with the aim of optimizing the performance of the practical MgB_2 multifilamentary wires. However, we found that C doping was less effective at high temperatures (T>20K), which motivated us to study other chemical doping.

We studied the effects of REO doping (Dy_2O_3 and Nd_2O_3) in MgB_2 bulk samples. Their microstructures and superconducting properties were carefully examined to reveal the relationships between them. During the formation of MgB_2, Dy_2O_3 and Nd_2O_3 additives were found to form nano-size DyB_4 and NdB_6 inclusions, respectively. These REB_x inclusions (20 nm – 150 nm) were formed both inside MgB_2 grains and on grain boundaries. The grain refinement caused by the REB_x inclusions on MgB_2 grain boundaries and the formation of new pinning centers by the REB_x inclusions inside MgB_2 grains led to the improvement of F_p and J_c in MgB_2 bulk and wires. Because of these, REO doping is beneficial to MgB_2 bulk and wires, and can be used to further improve the in-field performance of doped MgB_2 superconductors (e.g. C doped MgB_2 wires).

Finally, we studied the mechanism of ZrB_2, TiB_2, and NbB_2 doping in MgB_2 bulk using our HPT method for synthesizing doped MgB_2 bulk samples at high temperatures (up to 1700 °C) and at pressure (10 MPa) to explore solubility limits of dopant species in MgB_2, enhance diffusion, and (alternatively) attempt to form dense, nanoscale secondary phases during the sample synthesis. We explored both metal diborides (MB_2, where M = Zr, Ti and Nb) for attempted Mg site substitution and Dy_2O_3 for nanoscale intragrain precipitate formation. Our results suggested that instead of Mg site substitution reported in the literature [8, 113-115], MB_2 doping mainly caused the high density of defects and associated lattice strain in very small regions which were responsible to the changes in B_{c2} and T_c, but these regions were too small to change J_c. This explained the observation in [8, 113-115] that B_c values increased but J_c did not after MB_2 doping.

Future work:

This work studied the roles of chemical doping (C, REO, MB_2) in MgB_2 and provided useful information in the understanding and development of MgB_2 superconductors. However, it is not the end of the research. In terms of practical applications in the future, greater effort is still needed to further improve the superconducting properties (e.g., J_c, n-value, B_{c2} and B_k) and engineering design (e.g., wire structure, thermal stability and strain tolerance) of MgB_2. In this work doping induced changes in the microstructure and superconducting properties were studied and discussed, but how to incorporate these findings into the large scale fabrication of practical MgB_2 conductors remains a big challenge. Moreover, the improvements of B_{c2} and flux pinning by chemical doping are strongly dependent on the thermal conditions, and some of the positive results in this work were gained at very high temperatures and pressures. These parameters are impractical in terms of large scale manufacturing. Thus further research on the influence of these dopants on the microstructures and properties of MgB_2 practical wires heat treated at conventional temperatures (600°C-800°C) is still important and required.

Appendix A: List of Symbols

Symbols	Description
a, c	Lattice Parameters
A	Cross Section Area
A_{sc}	Cross Section Area of MgB_2 Core
B	Magnetic Field
B_c	Thermodynamic Critical Field
B_{c1}	Lower Critical Field
B_{c2}	Upper Critical Field
B_k	Kramer Irreversibility Field
D	Average Grain Size
D_σ	σ Band Electron Diffusivity
D_π	π Band Electron Diffusivity
E	Electrical Field
E_c	Electrical Field Criterion
f_i	Elemental Pinning Force
f_p	Normalized Pinning Force Density
F_p	Bulk Pinning Force Density
J_c	Critical Current Density
J_{ct}	Transport Critical Current Density
J_{cm}	Magnetic Critical Current Density
J_d	Depairing Current Density
K	Electric Connectivity
l	Electron Mean Free Path
S_v	Projected Volumetric Surface Area of Pins
T	Temperature
T_c	Superconducting Transition Temperature
U	Pinning Potential
V_f	Volume Fraction of Flux Lines within Pins
γ	Anisotropy Factor

(continued on the next page)

Symbols	Description
κ	Ginzburg-Landau Constant
λ	Field Penetration Depth
λ_1, λ_2	Intra-Band Electron-Phonon Coupling Constants
μ_0	Vacuum Permeability
ξ	Superconductor Coherence Length
Φ_o	Magnetic Flux Quantum

References

1. J. Nagamatsu, N. Nakagawa, T. Muranaka, Y. Zenitani, and J. Akimitsu, "Superconductivity at 39 K in magnesium diboride", *Nature*, **410** 63 (2001).
2. F. Jones and R. L. Taylor, "On boron hydride", *J. Chem. Soc., Trans.*, **39** 213–219 (1881).
3. H. K. Onnes, "The resistance of pure mercury at helium temperatures", *Commun. Phys. Lab Univ. Leiden*, **12** 120 (1911).
4. V. Russell, R. Hirst, F. A. Kanda, and A. J. King, "An X-ray study of the magnesium borides", *Acta Crystallographica*, **611** 12 870 (1953).
5. J. Q. Li, L. Li, Y. Q. Li, Z. A. Ren, G. C. Che and Z. X. Zhao, "Structural properties of MgB_2 superconductors with a critical current density greater than 10^5 A/cm^2", *Chin. Phys. Lett.*, **18** 680 (2001).
6. D. C. Larbalestier, A. Gurevich, D. M. Feldmann, and A. A. Polyanskii, "High-T_c superconducting materials for electric power applications", *Nature*, **414** 368 (2001).
7. D. C. Larbalestier, J. Jiang, U. P. Trociewitz, F. Kametani, C. Scheuerlein, M. Dalban-Canassy, M. Matras, P. Chen, N. C. Craig, P. J. Lee and E. E.

Hellstrom, “Isotropic round-wire multifilament cuprate superconductor for generation of magnetic fields above 30 T”, *Nature Mater.*, **13** 375-381 (2014).

8. M. Bhatia, “MgB_2 Superconductors: Processing, Characterization, and Enhancement of Critical Fields”, Ph.D. Thesis, The Ohio State University (2007).
9. M. Susner, “Influences of Crystalline Anisotropy, Porosity, and Connectivity on the Critical Current Densities of Superconducting Magnesium Diboride Bulk samples, Wires, and Thin Films”, Ph.D. thesis, The Ohio State University (2012).
10. G. Z. Li, “Connectivity, Doping, and Anisotropy in Highly Dense Magnesium Diboride (MgB_2)”, Ph.D. thesis, The Ohio State University (2015).
11. E. W. Collings EW, M. D. Sumption, M. Bhatia, M. A. Susner and S. D. Bohnenstiehl, “Prospects for improving the intrinsic and extrinsic properties of magnesiumdiboride superconducting strands”, *Supercond. Sci. Technol.* **21** 103001 (2008).
12. J. Kortus, I. I. Mazin, K. D. Belashchenko, V. P. Antropov, and L. L. Boyer, “Superconductivity of Metallic Boron in MgB_2”, *Phys. Rev. Lett*., **86** 4656–4659 (2001).
13. H. J. Choi, D. Roundy, H. Sun, M. L. Cohen and S. G. Louie, “The origin of the anomalous superconducting properties of MgB_2”, *Nature* **418** 758-760 (2001).
14. K. Chen, W. Q. Dai, C. G. Zhuang, Q. Li, S. Carabello, J. G. Lambert, J. T. Mlack, R. C. Ramos and X. X. Xi, “Momentum-dependent multiple gaps in magnesium diboride probed by electron tunnelling spectroscopy”, *Nature Communications* **3**, 619 (2012).

15. M. H. Jung, M. Jaime, A. H. Lacerda, G. S. Boebinger, W. N. Kang, H. J. Kim, E. M. Choi, and S. I. Lee, "Anisotropic superconductivity in epitaxial MgB_2 films", *Chemical physics letters*, **343** 5 447-451 (2001).
16. A. V. Sologubenko, J. Jun, S. M. Kazakov, J. Karpinski, and H. R. Ott, "Thermal conductivity of single-crystalline MgB_2", *Phys. Rev. B* **66** 014504 (2002).
17. S. Kim, D. S. Stone, J. Cho, C. Jeong, C. Kang and J. Bae, "Phase stability determination of the Mg–B binary system using the CALPHAD method and ab initio calculations," *Journal of Alloys and Compounds*, **470** 1–2 85–89 (2009).
18. M. M. R. Naslain, A. Guette and M. Barret, "Sur le diborure et le tétraborure de magnésium. Considérations cristallochimiques sur les tétraborures", *J. Solid State Chem*. **8** 68-85 (1973).
19. A. Pediaditakis, M. Schroeder, V. Sagawe, T. Ludwig and H. Hillebrecht, "Binary Boron-Rich Borides of Magnesium: Single-Crystal Investigations and Properties of MgB_7 and the New Boride Mg_5B_{44}", *Inorg. Chem.* **49** 10882-10893 (2010).
20. J. D. DeFouw and D. C. Dunand, "Mechanism and kinetics of MgB_2 synthesis from boron fibers", *Acta Mater.* **56** 5751 (2008).
21. J. D. DeFouw, J. P. Quintana and D. C. Dunand, "*In situ* X-ray synchrotron diffraction study of MgB_2 synthesis from elemental powders", *Acta Mater*. **56** 1680 (2008).
22. W. Meissner and R. Ochsenfeld, "Ein neuer Effekt bei Eintritt der Supraleitfähigkeit", *Die Naturwissenschaften* **21** 787 (1933).

23. E. Maxwell, “Isotope effect in the superconductivity of mercury”, *Phys. Rev.*, 78 **477** (1950).
24. A.C. Rose-Innes and E.H. Rhoderick, “Introduction to superconductivity”, Pergamon Press, New York, Second Edition (1987).
25. W. Meissner and R. Ochsenfeld, “Ein neuer Effekt bei Eintritt der Supraleitfähigkeit”, *Die Naturwissenschaften*, **21** 787 (1933).
26. J. Bardeen, L. N. Cooper and J. R. Schrieffer, “Microscopic theory of superconductivity”, *Phys. Rev.*, **106** 162 (1957).
27. J. Bardeen, L. N. Cooper, and J. R. Schrieffer, “Theory of superconductivity”, *Phys. Rev.,* **108** 1175 (1957).
28. M. Tinkham, “Introduction to Superconductivity”, McGraw-Hill, New York, Second Edition (1996).
29. S. L. Bud'ko, G. Lapertot, C. Petrovic, C. E. Cunningham, N. Anderson, and P. C. Canfield, “Boron isotope effect in superconducting MgB_2”, *Phys. Rev. Lett.* **86**, 1877–1880 (2001).
30. D. G. Hinks, H. Claus and J. D. Jorgensen, “The complex nature of superconductivity in MgB_2 as revealed by the reduced total isotope effect”, *Nature* **411** 457-460 (2001)
31. E. Maxwell, “Isotope effect in the superconductivity of mercury", *Phys. Rev.,* **78** 477 (1950).
32. C. A. Reynolds, B. Serin, and L. B. Nesbitt, “The Isotope Effect in Superconductivity. I. Mercury”, *Phys. Rev.* **84**, 691 (1951)

33. V.L. Ginzburg and L.D. Landau, “On the theory of superconductivity”, *Zh. Eksp. Teor. Fiz.* **20**, 1064–1082 (1950).

34. L. P. Gor’kov, “Microscopic Derivation of the Ginzburg-Landau Equations in the Theory of Superconductivity”, *Soviet Physics JETP*, **9**, 6 1364 (1959).

35. A. B. Pippard, “An experimental and theoretical study of the relation between magnetic field and current in a superconductor”, *Proc Roy Soc.* A**216**, 547 (1953).

36. C. G. Zhuang, S. Meng, C. Y. Zhang, Q. R. Feng, Z. Z. Gan, H. Yang, Y. Jia, H. H. Wen and X. X. Xi, “Ultrahigh current-carrying capability in clean MgB_2 films”, *J. Appl. Phys.* **104** 013924 (2008).

37. A. A. Abrikosov, “On the magnetic properties of superconductors of the second group”, *Soviet Physics JETP*, **5** ,6 (1957)

38. A. A. Abrikosov, “Nobel Lecture: Type-II superconductors and the vortex lattice”, *Rev. Mod. Phys.* **76**, 975 (2004).

39. R. Cubitt, M. R. Eskildsen, C. D. Dewhurst, J. Jun, S. M. Kazakov, and J. Karpinski, “Effects of Two-Band Superconductivity on the Flux-Line Lattice in Magnesium Diboride”, *Phys. Rev. Lett.*, **91**, 4 047002/1–047002/4 (2003).

40. J. D. Fletcher, A. Carrington, O. J. Taylor, S. M. Kazakov, and J. Karpinski, “Temperature-Dependent Anisotropy of the Penetration Depth and Coherence Length of MgB_2”, *Phys. Rev. Lett.*, **95**, 9 097005 (2005).

41. V. Moshchalkov, M. Menghini, T. Nishio, Q. H. Chen, A. V. Silhanek, V. H. Dao, L. F. Chibotaru, N. D. Zhigadlo and J. Karpinski, “Type-1.5 Superconductivity”, *Phys. Rev. Lett.* **102**, 117001 (2009).

42. A. Gurevich, “Enhancement of the upper critical field by nonmagnetic impurities in dirty two-gap superconductors”, *Phys. Rev. B* **67**, 184515 (2003).

43. A. Gurevich, S. Patnaik, V. Braccini, K. H. Kim, C. Mielke, X. Song, L. D. Cooley, S. D. Bu, D. M. Kim, J. H. Choi, L. J. Belenky, J. Giencke, M. K. Lee, W. Tian, X. Q. Pan, A. Siri, E. E. Hellstrom, C. B. Eom and D. C. Larbalestier, “Very high upper critical fields in MgB_2 produced by selective tuning of impurity scattering”, *Supercond. Sci. Technol.* **17** 278–286 (2004).

44. A. Gurevich, “Limits of the upper critical field in dirty two-gap superconductors”, *Physica C* **456** 160–169 (2007).

45. V. Ferrando, P. Manfrinetti, D. Marre, M. Putti, I. Sheikin, C. Tarantini, and C. Ferdeghini, "Effect of two bands on critical fields in MgB_2 thin films with various resistivity values", *Phys. Rev. B,* **8** (2003).

46. L. Gozzelino, B. Minetti, G. A. Ummarino, R. Gerbaldo, G. Ghigo, F Laviano, G. Lopardo, G. Giunchi, E. Perini and E. Mezzetti, “Intraband scattering rate and electronic diffusivity study in MgB_2 bulk samples”, *Supercond. Sci. Technol*. **22** 065007 (2009).

47. K. D. Usadel, “Generalized Diffusion Equation for Superconducting Alloys”, *Phys. Rev. Lett.* **25**, 507 (1970).

48. A. K. Pradhan, Z. X. Shi, M. Tokunaga, T. Tamegai, Y. Takano, K. Togano, H. Kito, and H. Ihara, “Electric transport and anisotropic superconducting properties in single crystalline and dense polycrystalline MgB_2”, *Phys. Rev. B.* **64** 212509 (2001).

49. G. K. Perkins, J. Moore, Y. Bugoslavsky, L. F. Cohen, J. Jun, S. M. Kazakov, J. Karpinski and A. D. Caplin, “Superconducting critical fields and anisotropy of a MgB_2 single crystal”, *Supercond. Sci. Technol*. **15** 1156 (2002).

50. C. Buzea and Y. Yamashita, “Review of superconducting properties of MgB_2”, *Supercond. Sci. Technol.* **14** 115–146 (2001)

51. M. Angst, R. Puzniak, A. Wisniewski, J. Jun, S. M. Kazakov, J. Karpinski, J. Roos and H. Keller, “Temperature and Field Dependence of the Anisotropy of MgB_2”, *Phys. Rev. Lett.* **88** 167004 (2002)

52. V. Braccini, “High-field superconductivity in alloyed MgB_2 thin films”, *Phys. Rev. B* **71**, 179902 (2005).

53. D. Wenqing, V. Ferrando, A.V. Pogrebnyakov, R.H.T. Wilke, K. Chen, X. Weng, J.M. Redwing, C.W. Bark, C.B. Eom, Y. Zhu, P.M. Voyles, D. Rickel, J.B. Betts, C. Mielke, A. Gurevich, D.C. Larbalestier, Q. Li and X.X. Xi, "High-field properties of carbon-doped MgB_2 thin films by hybrid physical-chemical vapor deposition using different carbon sources", *Supercond. Sci. Technol.*, **24** 125014 (2011).

54. A. Serquis, G. Serrano, S.M. Moreno, L. Civale, B. Maiorov, F. Balakirev and M. Jaime, "Correlated enhancement of H_{c2} and J_c in carbon nanotube doped MgB_2", *Supercond. Sci. Technol.*, **20** L12 (2007).

55. S. X. Dou, S. Soltanian, J. Horvat, X. L. Wang, S. H. Zhou, M. Ionescu, H. K. Liu, P. Munroe and M. Tomsic, "Enhancement of the critical current density and flux

pinning of MgB_2 superconductor by nanoparticle SiC doping," *Appl. Phys. Lett.*, **81** 3419 (2002).

56. M. Eisterer, M. Zehetmayer and H. W. Weber, "Current percolation and anisotropy in polycrystalline MgB_2", *Phys. Rev. Lett.*, **90** 247002 (2003).
57. M. Suenaga, A. K. Ghosh, Y. Xu and D. O. Welch, "Irreversibility temperatures of Nb_3Sn and Nb-Ti", *Phys. Rev. Lett.* **66** 1777 (1991).
58. G. Blatter, M. V. Feigel'man, V. B. Geshkenbein, A. I. Larkin and V. M. Vinokur, "Vortices in high-temperature superconductors", *Rev. Mod. Phys.* **66**, 1125 (1994).
59. T. Masui, E. Ohmichi, S. Tajima and T. Osada, "Irreversibility field and coherence length of Ca-substituted YBCO single crystals", *Physica C,* **426-434** 1 335-339 (2005).
60. D. C. Larbalestier, L. D. Cooley, M. O. Rikel, A. A. Polyanskii, J. Jiang, S. Patnaik, X. Y. Cai, D. M. Feldmann, A. Gurevich, A. A. Squitieri, M. T. Naus, C. B. Eom, E. E. Hellstrom, R. J. Cava, K. A. Regan, N. Rogado, M. A. Hayward, T. He, J. S. Slusky, P. Khalifah, K. Inumaru and M. Haas, "Strongly linked current flow in polycrystalline forms of the superconductor MgB_2", *Nature* **410**, 186-189 (2001).
61. D. K. Finnemore, J. E. Ostenson, S. L. Bud'ko, G. Lapertot and P. C. Canfield, "Thermodynamic and Transport Properties of Superconducting $Mg^{10}B_2$", *Phys. Rev. Lett.* **86**, 2420 (2001).
62. S. Patnaik, L. D. Cooley, A. Gurevich, A. A. Polyanskii, J. Jiang, X. Y. Cai, A. A. Squitieri, M. T. Naus, M. K. Lee, J. H. Choi, L. Belenky, S. D. Bu, J. Letteri, X. Song, D. G. Schlom, S. E. Babcock, C. B. Eom, E. E. Hellstrom and D. C.

Larbalestier, “Electronic anisotropy, magnetic field-temperature phase diagram and their dependence on resistivity in c-axis oriented MgB_2 thin films”, *Supercond. Sci. Technol*. **14** 315–319 (2001).

63. E. J. Kramera and A. D. Guptab, “A model of surface flux line pinning in type II superconductors”, *Philos. Mag.* **26**, 769 (1972).
64. E. J. Kramer, “Scaling laws for flux pinning in hard superconductors”, *J. Appl. Phys.* **44**, 1360 (1973).
65. D. Dew-Hughes, "Flux pinning mechanisms in type II superconductors", *Philos. Mag.*, **30** 293 (1974).
66. D. Dew-Hughes, "The role of grain boundaries in determining J_c in high-field high-current superconductors", *Philos. Mag.*, **55** 459. (1987).
67. B. J. Shaw, “Grain size and film thickness of Nb_3Sn formed by solid-state diffusion in the range 650–800 °C”, *J. Appl. Phys.* **47**, 2143 (1976).
68. E. Martínez, P. Mikheenko, M. Martínez-López, A. Millán, A. Bevan and J. S. Abell, “Flux pinning force in bulk MgB_2 with variable grain size”, *Phys. Rev. B,* **75,** 134515 (2007).
69. P. Mikheenko, E. Martínez3, A Bevan, J. S. Abell and J. L. MacManus-Driscoll, “Grain boundaries and pinning in bulk MgB_2”, *Supercond. Sci. Technol.* **20** S264-S270 (2007).
70. Z. X. Shi, M. A. Susner, M. D. Sumption, E. W. Collings, X. Peng, M. Rindfleisch and M. J. Tomsic, “Doping effect and flux pinning mechanism of nano-SiC additions in MgB_2 strands”, *Supercond. Sci. Technol.* **24** 065015 (2011).

71. A. Yamamoto, J. Shimoyama, K. Kishio and T. Matsushita, “Limiting factors of normal-state conductivity in superconducting MgB_2: an application of mean-field theory for a site percolation problem”, *Supercond. Sci. Technol.* **20** 658 (2007).

72. M. A. Susner, M. Bhatia, M. D. Sumption and E. W. Collings, “Electric resistivity, Debye temperature, and connectivity in heavily doped bulk MgB_2 superconductors”, *J. Appl. Phys.* **105**, 103916 (2009).

73. A. Yamamoto, H. Tanaka, J. Shimoyama, H. Ogino, K. Kishio and T. Matsushita, “Towards the Realization of Higher Connectivity in MgB_2 Conductors: In-situ or Sintered Ex-situ?”, *Jpn. J. Appl. Phys*. **51** 010105 (2012).

74. S. X. Dou, A. V. Pan, S. Zhou, M. Ionescu, H. K. Liu and P. R. Munroe, “Substitution-induced pinning in MgB_2 superconductor doped with SiC nano-particles”, *Supercond. Sci. Technol.* **15**, 1587 (2002).

75. S. X. Dou, A. V. Pan, S. Zhou, M. Ionescu, X. L. Wang, J. Horvat, H. K. Liu and P. R. Munroe, “Superconductivity, critical current density, and flux pinning in $MgB_{2-x}(SiC)_{x/2}$ superconductor after SiC nanoparticle doping”, *J. Appl. Phys*. **94** 1850 (2003).

76. R. F. Klie, J. C. Idrobo, N. D. Browning, K. A. Regan, N. S. Rogado and R. J. Cava, “Direct observation of nanometer-scale Mg- and B-oxide phases at grain boundaries in MgB_2”, *Appl. Phys. Lett.* **79**, 1837 (2001).

77. Y. Takano, H. Takeya, H. Fujii, H. Kumakura, T. Hatano, K. Togano and H. Kito, H. Ihara, “Superconducting Properties of MgB_2 Bulk Materials Prepared by High Pressure Sintering”, *Appl. Phys. Lett.* **78**, 2914 (2001).

78. A. Tampieria, G. Celottia, S. Sprioa, R. Caciuffob and D. Rinaldib, “Study of the sintering behaviour of MgB_2 superconductor during hot-pressing”, *Physica C* **400** 97–104 (2004).

79. J. M. Rowell, “The widely variable resistivity of MgB_2 samples”, *Supercond. Sci. Technol.* **16** R17–R27 (2003).

80. T. Matsushita, M. Kiuchi, A. Yamamoto, J. Shimoyama and K. Kishio, “Critical current density and flux pinning in superconducting MgB_2”, *Physica C* **468** 1833-1835 (2008).

81. T. Takenobu, T. Ito, Dam Hieu Chi, K. Prassides and Y. Iwasa, “Intralayer carbon substitution in the MgB_2 superconductor”, *Phys. Rev. B* **64**, 134513 (2001).

82. S. Lee, T. Masui, A. Yamamoto, H. Uchiyama and S. Tajima, "Carbon-substituted MgB_2 single crystals", *Physica C* **397** 7 (2003).

83. T. Masui, S. Lee and S. Tajima, "Carbon-substitution effect on the electronic properties of MgB_2 single crystals", *Phys. Rev. B*, **70** 024504 (2004).

84. E. Ohmichi, T. Masui, S. Lee, S. Tajima and T. Osada, "Enhancement of irreversibility field in carbon-substituted MgB_2 single crystals", *J. Phys. Soc. Jpn.*, **73** 2065 (2004).

85. C. Krutzler, M. Zehetmayer, M. Eisterer, H.W. Weber, N.D. Zhigadlo, J. Karpinski, and A. Wisniewski, "Anisotropic reversible mixed-state properties of superconducting carbon-doped $Mg(B_{1-x}C_x)_2$ single crystals", *Phys. Rev. B*, **74** 144511 (2006).

86. S. M. Kazakov, R. Puzniak, K. Rogacki, A. V. Mironov, N. D. Zhigadlo, J. Jun, C. Soltmann, B. Batlogg and J. Karpinski, "Carbon substitution in MgB_2 single crystal: structural and superconducting properties", *Phys. Rev. B*, **71** 024533 (2005).

87. M. Bhatia, M. D. Sumption, E. W. Collings, "Effect of various additions on upper critical field and irreversibility field of in-situ MgB_2 superconducting bulk material", *IEEE Trans. Appl. Supercond.,* **15** 3204-3206 (2005).

88. M. D. Sumption, M. Bhatia, M. Rindfleisch, M. Tomsic, S. Soltanian, S. X. Dou, E. W. Collings, "Large upper critical field and irreversibility field in MgB_2 wires with SiC additions", *Appl. Phys. Lett.*, **86** 092507 (2005).

89. J. H. Kim, S. Zhou, M. S. Hossain, A. V. Pan and S. X. Dou, "Carbohydrate doping to enhance electromagnetic properties of MgB_2 superconductors", *Appl. Phys. Lett.* **89**, 142505 (2006).

90. Z. Gao, Y. Ma, X. Zhang, D. Wang, H. Yang, H. Wen and K. Watanabe, "Influence of oxygen contents of carbohydrate dopants on connectivity and critical current density in MgB_2 tapes", *Appl. Phys. Lett.* **91**, 162504 (2007).

91. S. D. Bohnenstiehl, M. A. Susner, Y. Yang, E. W. Collings, M. D. Sumption, M. A. Rindfleisch and R. Boone, "Carbon doping of MgB_2 by toluene and malic-acid-in-toluene", *Physica C,* **471** 3-4 108-111 (2011).

92. J. V. Marzik, R. J. Suplinskas, R. H. T. Wilke, P. C. Canfield, D. K. Finnemore, M. Rindfleisch, J. Margolies and S. T. Hannahs, "Plasma synthesized doped B powders for MgB_2 superconductors", *Physica C* **423**, 3–4 83–88 (2005).

93. M. A. Susner, Y. Yang, M. D. Sumption, E. W. Collings, M. A. Rindfleisch, M. J. Tomsic and J. V. Marzik, “Enhanced critical fields and superconducting properties of pre-doped B powder-type MgB_2 strands”, *Supercond. Sci. Technol.* **24**, 012001 (2011).

94. J. Kortus, O. V. Dolgov, R. K. Kremer and A. A. Golubov, “Band filling and interband scattering effects in MgB_2: carbon versus aluminum doping”, *Phys. Rev. Lett.* **94**, 027002 (2005).

95. M. Eisterer, “Magnetic properties and critical currents of MgB_2”, *Supercond. Sci. Technol.* **20**, R47–R73 (2007).

96. J.H. Kim, S. Oh, Y.-U. Keo, S. Hata, H. Kumakura, A. Matsumoto, M. Mitsuhara, S. Choi, Y. Shimada, M. Maeda, J.L. MacManus-Driscoll and S.X. Dou, "Microscopic role of carbon on MgB_2 wire for critical current density comparable to NbTi", *NPG Asia Mater.*, **4** 1 (2012).

97. M. A. Susner, S. D. Bohnenstiehl, S. A. Dregia, M. D. Sumption, Y. Yang, J. J. Donovan and E. W. Collings, “Homogeneous carbon doping of magnesium diboride by high-temperature, high-pressure synthesis”, *Appl. Phys. Lett.* **104,** 162603 (2014).

98. S. D. Bohnenstiehl, “Thermal analysis, phase equilibria, and superconducting properties in MgB_2 and carbon doped MgB_2”, Ph.D. thesis, The Ohio State University (2011).

99. M. A. Susner M. D. Sumption, M. A. Rindfleisch and E. W. Collings, “Critical current densities of doped MgB_2 strands in low and high applied field ranges: The $J_c(B)$ crossover effect”, *Physica C*, **490** 20-25 (2014).

100. W. X. Li, R. Zeng, L. Lu, Y. Zhang, S. X. Dou, Y. Li, R. H. Chen and M. Y. Zhu, “Improved superconducting properties of in situ powder-in-tube processed $Mg_{1.15}B_2$/Fe wires with nano-size SiC addition”, *Physica C* **469** 1519–1522 (2009).

101. M. A. A. Mahmud, M. A. Susner, M. D. Sumption, M. A. Rindfleisch, M. J. Tomsic, J. Yue and E. W. Collings, “Comparison of critical current density in MgB_2 with different boron sources and nano-particle dopant additions”, *IEEE Trans. Appl. Supercond.,* **19** 2756-2759 (2009).

102. M. Mudgel, V. P. S. Awana, H. Kishan and G. L. Bhalla, “Significant improvement of flux pinning and irreversibility field in nano-carbon-doped MgB_2 superconductor”, *Solid State Commun.,* **146** 300-334 (2008).

103. J. S. Slusky, N. Rogado, K. A. Regan, M. A. Hayward, P. Khalifah, T. He, K. Inumaru, S. M. Loureiro, M. K Haas, H. W. Zandbergen and R. J. Cava, “Loss of superconductivity with the addition of Al to MgB_2 and a structural transition in $Mg_{1-x}Al_xB_2$”, *Nature* **410,** 343-345 (2001).

104. Y. Zhong, M. Yang and Z. K. Liu, “Contribution of first-principles energetics to Al-Mg thermodynamic modeling”, *Calphad*. **29,** 303-311 (2005).

105. J. Q. Li, L. Li, F. M. Liu, C. Dong, Y. Xiang and Z. X. Zhao, “Superconductivity, superstructure, and structure anomalies in $Mg_{1-x}Al_xB_2$”, *Phys. Rev. B* **65** 132505 (2002).

106. J. Y. Xiang, D. N. Zheng, J. Q. Li, L. Li, P. L. Lang, H. Chen, C. Dong, G. C. Che, Z. A. Ren, H. H Qi, H. Y Tian, Y. M Ni and Z. X Zhao, "Superconducting properties and c-axis superstructure of $Mg_{1-x}Al_xB_2$", *Phys. Rev. B* **65** 214536 (2002).

107. M. Putti, C. Ferdeghini, M. Monni, I. Pallecchi, C. Tarantini, P. Manfrinetti, A. Palenzona, D. Daghero, R. S. Gonnelli and V. A. Stepanov, "Critical field of Al-doped MgB_2 samples: Correlation with the suppression of the σ-band gap", *Phys. Rev. B* **71**, 144505 (2005).

108. J. Karpinski, N. D. Zhigadlo, G. Schuck, S. M. Kazakov, B. Batlogg, K. Rogacki, R. Puzniak, J. Jun, E. Müller, P. Wägli, R. Gonnelli, D. Daghero, G. A. Ummarino and V. A. Stepanov, "Al substitution in MgB_2 crystals: Influence on superconducting and structural properties", *Phys. Rev. B* **71**, 174506 (2005).

109. H. W. Zandbergen, M. Y. Wu, H. Jiang, M. A. Hayward, M. K. Haas and R. J. Cava, "The complex superstructure in $Mg_{1-x}Al_xB_2$ at $x \approx 0.5$", *Physica C* **366** 221–228 (2002).

110. S. Agrestini, D. Di Castro, M. Sansone, N. L. Saini, A. Saccone, S. De Negri, M. Giovannini, M. Colapietro and A. Bianconi, "High T_c superconductivity in a critical range of micro-strain and charge density in diboribes", *J. Phys.: Condens. Matter* **13** 11689–11695 (2001).

111. P. Vajeeston, P. Ravindran, C. Ravi and R. Asokamani, "Electronic structure, bonding, and ground-state properties of AlB_2-type transition-metal diborides", *Phys. Rev. B* **63**, 045115 (2001).

112. R. Arroyave, D. Shin and Z. K. Liu, “Modification of the thermodynamic model for the Mg-Zr system”, *Calphad*, **29**, 230-238 (2005).

113. Y. Feng., Y. Zhao, Y. P. Sun, F. C. Liu, B. Q. Fu, L. Zhou, C. H. Cheng, N. Koshizuka and M. Murakami, “Improvement of critical current density in MgB_2 superconductors by Zr doping at ambient pressure”, *Appl. Phys. Lett.* **79**, 3983 (2001).

114. Y. Feng., Y. Zhao, A. K. Pradhan, C. H. Cheng, J. K. F. Yau, L. Zhou, N. Koshizuka and M. Murakami, “Enhanced flux pinning in Zr-doped MgB_2 bulk superconductors prepared at ambient pressure”, *J. Appl. Phys.* **92**, 2614 (2002).

115. M. Bhatia., M. D. Sumption, E. W. Collings and S. Dregia, “Increases in the irreversibility field and the upper critical field of bulk MgB_2 by ZrB_2 addition”, *Appl. Phys. Lett.* **87**, 042505 (2005).

116. X. P. Zhang, Z. S. Gao, D. L. Wang, Z. G. Yu, Y. W. Ma, S. Awaji and K. Watanabe, “Improved critical current densities in MgB_2 tapes with ZrB_2 doping”, *Appl. Phys. Lett.* **89**, 132510 (2006).

117. M. A. Susner, M. D. Sumption, A. Takase, and E. W. Collings, “Evidence for Zr site-substitution for Mg in PLD-deposited MgB_2 thin films”, *Supercond. Sci. Technol.* **27**, 075009 (2014).

118. J. Wang, Y. Bugoslavsky, A. Berenov, L. Cowey, A. D. Caplin, L. F. Cohen, J. L. MacManus Driscoll, L. D. Cooley, X. Song and D. C. Larbalestier, “High critical current density and improved irreversibility field in bulk MgB_2 made by a scaleable, nanoparticle addition route”, *Appl. Phys. Lett.* **81**, 2026 (2002).

119. S. K. Chen, M. Wei and J. L. MacManus-Driscoll, “Strong pinning enhancement in MgB_2 using very small Dy_2O_3 additions”, *Appl. Phys. Lett.* **88** 192512 (2006).

120. C. Yao, X. Zhang, D. Wang, Z. Gao, L. Wang, Y. Qi, C. Wang, Y. Ma, S. Awaji and K. Watanabe, “Doping effects of Nd_2O_3 on the superconducting properties of powder-in-tube MgB_2 tapes”, *Supercond. Sci. Technol.* **24** 055016 (2011).

121. C. Cheng and Y. Zhao, “Enhancement of critical current density of MgB_2 by doping Ho_2O_3”, *Appl. Phys. Lett.* **89** 252501 (2006).

122. N. Ojha, V. K. Malik, R. Singla, C. Bernhard and G. D. Varma, “The effect of carbon and rare earth oxide co-doping on the structural and superconducting properties of MgB_2”, *Supercond. Sci. Technol.* **23** 045005 (2010).

123. C. E. J. Dancer, P. Mikheenko, A. Bevan, J. S. Abell, R. I. Todd, and C. R. M. Grovenor, “A study of the sintering behaviour of magnesium diboride”, *J. Euro. Ceram. Soc*. **29** 1817 (2009).

124. G. Giunchi, S. Ceresara, G. Ripamonti, S. Chiarelli and M. Spadoni, “MgB2 reactive sintering from the elements”, *IEEE Trans. Appl. Superconduct.,* **13** 3060 (2003).

125. Y. Yang, G. Li, M. A. Susner, M. D. Sumption, M. Rindfleisch, M. Tomsic and E. W. Collings, “The Influence of Densification on the Critical Current Density of MgB_2 Strands”, presented at the Cryogenic Engineering Conference & International Cryogenic Materials Conference (CEC/ICMC) in Spokane, Washington, USA 2011.

126. E. W. Collings, E. Lee, M. D. Sumption and M. Tomsic, “Transport and Magnetic Properties of Continuously Processed MgB_2”, *Rare Metal Mat. Eng.* **31** 406–409 (2002).

127. S. D. Bohnenstiehl, M. A. Susner, S. A. Dregia, M. D. Sumption, J. Donovan and E. W. Collings, “Experimental determination of the peritectic transition temperature of MgB_2 in the Mg–B phase diagram”, *Thermochim. Acta* **576,** 27–35 (2014).

128. G. Grasso, A. Malagoli, M. Modica, A. Tumino, C. Ferdeghini, A. S. Siri, C. Vignola, L Martini, V. Previtali and G. Volpini, “Fabrication and Properties of Monofilamentary MgB_2 Superconducting Tapes”, *Supercond. Sci. Technol*. **16** 271–275 (2003).

129. G. Giunchi, G. Ripamonti, E. Perini, T. Cavallin and E. Bassani, “Advancements in the Reactive Liquid Mg Infiltration Technique to Produce Long Superconducting MgB_2 Tubular Wires”, *IEEE Trans. Appl. Supercond.* **17** 2761-2765 (2007).

130. J. M. Hur, K. Togano, A. Matsumoto, H. Kumakura, H. Wada and K. Kimura, “Fabrication of High-performance MgB_2 Wires by an Internal Mg Diffusion Process”, *Supercond. Sci. Technol*. **21** 032001 (2008).

131. M. D. Sumption, X. Peng, E. Lee, M. Tomsic and E. W. Collings, “Transport Current in MgB_2 based Superconducting Strand at 4.2 K and Self-Field”, cond-mat/0102441 (2001).

132. E. W. Collings, E. Lee, M. D. Sumption, M. Tomsic, X. L. Wang, S. Soltanian and S. X. Dou, “Continuous-and Batch-Processed MgB2/Fe Strands - Transport and Magnetic Properties”, *Physica C* **386** 555–559 (2003).

133. H. Kumakura, A. Matsumoto, H. Fujii, H. Kitaguchi, S. Ooi, K. Togano and H. Hatakeyama, “Fabrication and Properties of Powder-in-Tube Processed MgB_2 Tapes and Wires”, *Journal of Low Temperature Physics* **131** 1085-1093 (2003).

134. W. Goldacke, S. I. Schlachter, B. Obst, M. Eisterer, “*In-situ* MgB_2 Round Wires with Improved Properties”, *Supercond. Sci. Technol.* **17** S490-S495 (2004).

135. R. Flukiger, H. L. Suo, N. Musolino, C. Beneduce, P. Toulemonde and P. Lezza, “Superconducting Properties of MgB_2 Tapes and Wires”, *Physica C*, **385** 286-305 (2003).

136. B. A. Glowacki, M. Majoros, M. Vickers, J. E. Evetts, Y. Shi, I. McDougall, “Superconductivity of Powder-in-Tube MgB_2 Wires”, *Supercond. Sci. Technol*. **14** 193-199 (2001).

137. S. Soltanian, X. L. Wang, I. Kusevic, E. Babic, A. H. Li, M. J. Qin, J. Horvat, H. K. Liu, E. W. Colling, E. Lee, M. D. Sumption and S. X. Dou, “High-Transport Critical Current Density above 30 K in Pure Fe-clad MgB_2 Tape”, *Physica C* **361** 84-90 (2001).

138. M. A. Susner, M. D. Sumption, M. Bhatia, X. Peng, M. J. Tomsic, M. A. Rindfleisch and E. W. Collings, “Influence of Mg/B Ratio and SiC Doping on Microstructure and High Field Transport J_c in MgB_2 Strands”, *Physica C* **456** 180–187 (2007).

139. M. D. Sumption, M. Bhatia, X. Wu, M. Rindfleisch, M. Tomsic and E. W. Collings, Multifilamentary, *in situ* route, Cu-stabilized MgB_2 Strands", *Supercond. Sci. Technol.* **18** 730–734 (2005).

140. M. D. Sumption, M. Bhatia, M. Rindfleisch, M. Tomsic and E. W. Collings, "Transport Properties of Multifilamentary, *in-situ* Route, Cu-Stabilized MgB_2 Strands: One Metre Segments and the $J_c(B, T)$ Dependence of Short Samples", *Supercond. Sci. Technol*. **19** 155–160 (2006).

141. S. K. Chen, K. A. Yates, M. G. Blamire and J. L. MacManus-Driscoll, "Strong Influence of Boron Precursor Powder on the Critical Current Density of MgB_2" *Supercond. Sci. and Tech.* **18** 1473–1477 (2005).

142. X. Xu, M. J. Qin, K. Konstantinov, D. I. dos Santos, W. K. Yeoh, J. H. Kim and S. X. Dou, "Effect of Boron Powder Purity on Superconducting Properties of MgB_2", *Supercond. Sci. and Technol.* **19** 466–469 (2006).

143. J. H. Kim, W. K. Yeoh, M. J. Qin, X. Xu and S. X. Dou, "The Doping Effect of Multiwall Carbon Nanotube on MgB_2/Fe Superconductor Wire", *J. Appl. Phys.* **100,** 013908 (2006).

144. H. Yamada, M. Hirakawa, H. Kumakura, H. Kitaguchi, "Effect of Aromatic Hydrocarbon Addition on in-situ Powder-in-Tube Processed MgB_2 Tapes", *Supercond. Sci. Technol.* **19** 175-177 (2006).

145. J. H. Kim, X. Xu, M. S. Hossain, D. Q. Shi, Y. Zhao, X. L. Wang, S. X. Dou and S. Choi, "Influence of Disorder on the in-field J_c of MgB_2 Wires using Highly Active Pyrene", *Appl. Phys. Lett.* **92** 042506-042506-3 (2008).

146. R. Flükiger, M. D. Shahriar, A. Hossain, C. Senatore, F. Buta and M. Rindfleisch, "A New Generation of In-Situ MgB_2 Wires with Improved J_c and B_{irr} Values Obtained by Cold Densification (CHPD)", *IEEE Trans Supercond.* **21** 2649 – 2654 (2011).

147. W. Goldacker, S. I. Schlachter, B. Liu, B. Obst, E. Klimenko, "Considerations on Critical Currents and Stability of MgB_2 Wires Made by Different Preparation Routes", *Physica C* **401** 80–86 (2004).

148. H. Kitaguchi, A. Matsumoto, H. Hatakeyama and H. Kumakura, "*V–I* Characteristics of MgB_2 PIT Composite tapes: *n*-values under strain, in High Fields, or at High Temperatures", *Physica C* **401** 246–250 (2004).

149. H. L. Suo, P. Lezza, D. Uglietti, C. Beneduce, V. Abächerli and Flükiger R, "Transport Critical Current Densities and *n* Factors in Mono- and Multifilamentary MgB_2/Fe Tapes and Wires Using Fine Powders", *IEEE Trans. Appl. Supercond*. **13** 3265-3268 (2003).

150. E. Martínez, M. Martínez-López, A. Millán, P. Mikheenko, A. Bevan andJ. S. Abel, "Temperature and Magnetic Field Dependence of the *n*-Values of MgB_2 Superconductors", *IEEE Trans. Appl. Supercond*. **17** 2738-2741 (2007).

151. J. H. Kim, S. X. Dou, A. Matsumoto, S. Choi, T. Kiyoshi and H. Kumakura, "Correlation between Critical Current Density and *n*-Value in MgB_2/Nb/Monel Superconductor Wires", *Physica C* **470** 1207–1210 (2010).

152. M. Nilsson-MeUbin, A. Parikh and S. Salama, "*I-V* Characteristics of Melt-Textured $YBa_2Cu_30_{7-x}$ Superconductors Containing Grain Boundaries", *Physica C* **223** 19-29 (1994).

153. E. Zeldov, N. M. Amer, G. Koren, A. Gupta, M. W. McElfresh and R. J. Gambino, "Flux Creep Characteristics in High-Temperature Superconductors", *Appl. Phys Let* **56** 680-682 (1990).

154. K. Berger, J. Lévêque, D. Netter, B. Douine and A. Rezzoug, "Influence of Temperature and/or Field Dependences of the *E–J* Power Law on Trapped Magnetic Field in Bulk YBaCuO", *IEEE Trans. Appl. Supercond*. **17** 3028-3031 (2007).

155. P. Kováč, I. Hušek, T. Melišek, E. Martinez and M. Dhalle, "Properties of doped ex and in situ MgB_2 multi-filament superconductors", *Supercond. Sci. Technol*. **19** 1076–1082 (2006).

156. A. Malagoli, C. Bernini, V. Braccini, C. Fanciulli, G. Romano and M. Vignolo, "Fabrication and superconducting properties of multifilamentary MgB_2 conductors for AC purposes: twisted tapes and strands with very thin filaments", *Supercond. Sci. Technol.* **22** 105017 (2009).

157. P. Kováč, I. Hušek, T. Melišek, L. Kopera and M. Reissner, "Stainless steel reinforced multi-core MgB_2 wire subjected to variable deformations, heat treatments and mechanical stressing", *Supercond. Sci. Technol.* **23** 065010 (2010).

158. P. Kováč, I. Hušek, T. Melišek and L. Kopera, "Filamentary MgB_2 wires twisted before and after heat treatment", *Supercond. Sci. Technol.* **24** 115006 (2011).

159. P. Kováč, L. Kopera, T. Melišek, M. Rindfleisch, W. Haessler and I. Hušek, "Behaviour of filamentary MgB_2 strands subjected to tensile stress at 4.2 K", *Supercond. Sci. Technol.* **26** 105028 (2013).

160. H. Kitaguchi, H. Kumakura and K. Togano, "Strain effect in MgB_2/stainless steel superconducting tape", *Physica C* **363** 198-201 (2001).

161. H. Kitaguchi and H. Kumakura, "Superconducting and mechanical performance and the strain effects of a multifilamentary MgB_2/Ni tape", *Supercond. Sci. Technol*. **18** S284 (2005).

162. G. Nishijima, S. J. Ye, A. Matsumoto, K. Togano, H. Kumakura, H. Kitaguchi and H. Oguro, "Mechanical properties of MgB_2 superconducting wires fabricated by internal Mg diffusion process", *Supercond. Sci. Technol*. **25** 054012 (2012)

163. P. Kováč, I. Hušek, T. Melišek, L. Kopera and J. Kováč, "Critical currents I_c-anisotropy and stress tolerance of MgB_2 wires made by internal magnesium diffusion", *Supcond. Sci. Technol.* **27** 065003 (2014)

164. K. Katagiri, R. Takaya, K. Kasaba, K. Tachikawa, Y. Yamada, S. Shimura, N. Koshizuka and K. Watanabe, "Stress–strain effects on powder-in-tube MgB_2 tapes and wires", *Supercond. Sci. Technol.***18** 351–355 (2005)

165. G. Z. Li, M. D. Sumption, M. A. Susner, Y. Yang, K. M. Reddy, M. A. Rindfleisch, M. J. Tomsic, C. J. Thong and E. W. Collings, "The critical current density of Advanced Internal-Mg-Diffusion-processed MgB_2 wires", *Supercond. Sci. Technol.* **25** 115023 (2012)

166. P. Lezza, V. Abächerli, N. Clayton, C. Senatore, D. Uglietti, H. L. Suo and R. Flükiger, "Transport properties and exponential *n*-values of Fe/MgB_2 tapes with various MgB_2 particle sizes", *Physica C* **401** 305 (2003).

167. E. Martínez, A. Angural, S. Schlachter and P. Kováč, "Transport and magnetic critical currents of Cu-stabilized monofilamentary MgB_2 conductors", *Supercond. Sci. Technol.* **22** 015014 (2009)

168. A. E. Curzon and H. G. Chlebek, "The observation of face centred cubic Gd, Tb, Dy, Ho, Er and Tm in the form of thin films and their oxidation", *J. Phys. F* **3**, 1-5 (1973).

169. Z. P. Yin and W. E. Pickett, "Rare-earth–boron bonding and 4f state trends in RB_4 tetraborides", *Phys. Rev. B* **77**, 035135 (2008).

170. L. D. Cooley, A. J. Zambano, A. R. Moodenbaugh, R. F. Klie, J. X. Zheng and Y. Zhu, "Inversion of two-band superconductivity at the critical electron doping of $(Mg,Al)B_2$", *Phys. Rev. Lett.* **95,** 267002 (2005).

171. A. J. Zambano, A. R. Moodenbaugh and L. D. Cooley, "Effects of different reactions on composition homogeneity and superconducting properties of Al-doped MgB_2", *Supercond. Sci. Technol.* **18,** 1411–1420 (2005).

172. T. Matsushita, "Flux pinning in superconductors", *2nd edn*, Springer, Ch. 9.2, 384-386 (2014).

173. M. Mudgel, L. S. Sharath Chandra, V. Ganesan, G. L. Bhalla, H. Kishan and V. P. S. Awana, "Enhanced critical parameters of nanocarbon doped MgB_2 superconductor", *J. Appl. Phys.* **106** 033904 (2009).

174. A. Yamamoto, J. Shimoyama, I. Iwayama, Y. Katsura, S. Horii and K. Kishio, "Influence of dopant particle size on the critical current properties and microstructures of MgB_2 bulk samples doped with TiC and SiC", *Physica C* **463–465** 807–11 (2007).

175. P. Lezza, C. Senatore and R. Flukiger, "Improved critical current densities in B_4C doped MgB_2 based wires", *Supercond. Sci. Technol*. **19** 1030–3 (2006).

176. N. Hörhager, M. Eisterer, H. W. Weber, T. Prikhna, T. Tajima and V. F. Nesterenko, "Ti and Zr doped MgB_2 bulk superconductors", *J. Phys.: Conf. Ser*. **43** 500–4 (2006).

177. P. N. Togouleva, N. M. Suleimanova and K. Conderb, "Pinning enhancement in MgB_2-magnetic particles composites", *Physica C* **450** 45–7 (2006).

178. M. Mudgel, V. P. S. Awana, H. Kishan, R. Rawat, A. V. Narlokar, S. Balamurugan and G. L. Bhalla, "Impact of nano-Mo addition/substitution on the phase formation and superconductivity of $Mg_{1-x}Mo_xB_2$ (x=0.0 to 0.50)", *Mod. Phys. Lett. B* **21**, 875 (2007).

179. S. X. Dou, S. Soltanian, Y. Zhao, E. Getin, Z. Chen, O. Shcherbakova and J. Horvat, "The effect of nanoscale Fe doping on the superconducting properties of MgB_2", *Supercond. Sci. Technol*. **18** 710–5 (2005).

180. A. Tampieria, G. Celottia, S. Sprioa, D. Rinaldib, G. Baruccab and R. Caciuffo, "Effects of copper doping in MgB_2 superconductor", *Solid State Commun.* **121** 497–500 (2002).

181. C. Shekhar, R. Giri, R. S. Tiwari, O. N. Srivastava and S. K. Malik, “High critical current density and improved flux pinning in bulk MgB_2 synthesized by Ag addition”, *J. Appl. Phys.* **101** 043906 (2007).

182. L. Shi, S. Zhang and H. Zhang, “Effects of Co and Mn doping on the structure and superconductivity of MgB_2”, *Solid State Commun,* **147** 27 (2008).

183. Q. Zhao, Y. C. Liu, S. Penner, L. M. Yu, Z. Dong and Z. M. Gao, “Characterization and the mechanism of formation of the ternary compound $MgNi_{2.5}B_2$ in Ni-doped MgB_2 bulk”, *Supercond. Sci. Technol.,* **22** 075024 (2009).

184. J. Huo, Y. C. Liu, Z. Dong and H. Jiang, “Effect of Sn-doping on the sintering process of MgB_2 and its superconductive properties”, *J Mater Sci: Mater Electron,* **22** 233 (2011).

185. C. Shekhar, R. Giri, R. S. Tiwari, D. S. Rana, S. K. Malik and O. N. Srivastava, “Effect of La doping on microstructure and critical current density of MgB_2”, *Supercond. Sci. Technol.* **18** 1210–4 (2005).

186. Y. Takikawa, M. Takeda, M. Migita, M. Uehara, T. Kuramoto and Y. Kimishima, “Effect of W-addition on pinning property of MgB_2”, *Physica C,* **471** 905 (2011).

187. J. C. Grivel, N. Anderson, P. G. A. P. Pallewatta, Y. Zhao, and M. V. Zimmermann, “Influence of Bi, Se and Te additions on the formation temperature of MgB_2”, *Supercond. Sci. Technol.,* **25** 015010 (2012).

188. L. B. S. DaSliva, D. Rodrigues, G. Serrano, V. C. V. Metzner, M. T. Malachevsky and A. Serquis, “MgB_2 superconductors with addition of other diboride and SiC”, *IEEE Trans. Appl. Superconduct.,* 21 2639 (2011).

189. M. Gharaibeh, B. A. Albiss, I. Jumah, and I. M. Obaidat, “Effective incorporation of nanoceria into polycrystalline MgB_2”, *J. Appl. Phys.,* **107** 063908 (2010).

190. M. Burdusel, G. Aldica, S. Popa, M. Enculescu and P. Badica, “MgB_2 with addition of Sb_2O_3 obtained by spark plasma sintering technique”, *J. Mater. Res.,* **47** 3828 (2012).

191. D. Rodrigues, J. Jiang, Y. Zhu, P. M. Voyles, D. C. Larbalestier and E. E. Hellstrom, “Flux pinning optimization of MgB_2 bulk samples prepared using high energy ball milling and addition of TaB_2”, *IEEE Trans. Appl. Superconduct.,* **19** 2797 (2009).

192. Y. Yang, M. A. Susner, M. D. Sumption, M. A. Rindfleisch, M. J. Tomsic and E. W. Collings “Influence of Strand Design, Boron Type, and Carbon Doping Method on the Transport Properties of Powder-in-Tube $MgB_{2-x}C_x$ Strands”, *IEEE Trans. Appl. Supercond.* **22** 6200110 (2012).

193. Y. Yang, “C doping Report”, *Internal Report,* 2010.

194. Y. Yang, “Variable Temperature Measurements Report”, *Internal Report,* 2010.

195. Y. Yang, “Heat Treatment Optimization Report”, *Internal Report,* 2010.

196. Y. Yang, G. Li, M. Susner, M. D. Sumption, M. Rindfleisch, M. Tomsic and E. W. Collings, “Influence of twisting and bending on the J_c and *n*-value of multifilamentary MgB_2 strands”, *Physica C,* **519** 188-123 (2015).

197. M. Nilsson-Mellbin, A. Parikh and K. Salama, “*I-V* characteristics of melt-textured $YBa_2Cu_3O_{7-x}$ superconductors containing grain boundaries”, *Physica C,* **223** 19-29 (1994).

198. N. Schönborg and S. Hörnfeldt, “Model of the temperature dependence of the hysteresis losses in a high-temperature superconductor”, *Physica C,* **372-376** 1734-1738 (2004).

199. Y. Yang, M. A. Susner and M. D. Sumption, “Critical Current and *n*-values of MgB_2 strands in a range of B-T”, presented in the Cryogenic Engineering Conference & International Cryogenic Materials Conference (CEC/ICMC) in Spokane, Washington, USA 2011.

200. Z. X. Shi, M. A. Susner, M. Majoros, M. D. Sumption, X. Peng, M. Rindfleisch, M. J. Tomsic and E. W. Collings, “Anisotropic connectivity and its influence on critical current densities, irreversibility fields, and flux creep in in situ processed MgB_2 strands”, *Supercond. Sci. Technol.,* **23** 045018 (2010).

201. P. Fabbricatore, M. Greco, R. Musenich, P. Kovac, I. Husek and F. Gomory, "Influence of the sintering process on critical currents, irreversibility lines and pinning energies in multifilamentary MgB_2 wires", *Supercond. Sci. Technol.* **16** 364–370 (2003).

202. M. Pissas, E. Moraitakis, D. Stamopoulos, G. Papavassiliou, V. Psycharis and S. Koutandos, "Surface Barrier and Bulk Pinning in MgB_2 Superconductor", *Journal of Superconductivity: Incorporating Novel Magnetism* **14** 5 (2001).

203. T. T. M. Palstra, B. Batlogg, L. F. Schneemeyer and J. V. Waszczak, “Thermally Activated Dissipation in $Bi_{2.2}Sr_2Ca_{0.8}Cu_2O_{8+\delta}$”, *Phys. Rev. Lett.* **61**, 1662 (1988).

204. S. X. Dou, O. Shcherbakova, W. K. Yeoh, J. H. Kim, S. Soltanian, X. L. Wang, C. Senatore, R. Flukiger, M. Dhalle, O. Husnjak and E. Babic, “Mechanism of

enhancement in electromagnetic properties of MgB_2 by Nano SiC Doping", *Phys. Rev. Lett.* **98,** 097002 (2007).

205. P. Kovac, I. Husek, T. Melisek, J. C. Grivel, W. Pachla, V. Strbık, R. Diduszko, J. Homeyer and N. H. Andersen, "The role of MgO content in ex situ MgB_2 wires", Rapid Communication, *Supercond. Sci. Technol.* **17** L41–L46 (2004).
206. L. P. Aldridge, "Accuracy and precision of an X-ray diffraction method for analysing portland cements", *Cement and Concrete Research* **12** 4 437-446 (1982).
207. J. I. Goldstein *et al*., "Scanning Electron Microscopy and X-ray Micronalysis", 3rd ed, Plenum Press, New York (2003).